Università degli Studi di Padova
Dipartimento di Scienze Chimiche

Scuola di Dottorato di Ricerca in Scienza e Ingegneria dei Materiali
XXIV ciclo

Microfluidic Devices:
Compact Laboratories from Design to Application

Direttore della Scuola: Ch.mo Prof. Gaetano Granozzi
Supervisore: Ch.mo Prof. Michele Maggini

Dottorando: Simone Silvestrini

Università degli Studi di Padova
Dipartimento di Scienze Chimiche

Scuola di Dottorato di Ricerca in Scienza e Ingegneria dei Materiali
XXIV ciclo

Microfluidic Devices: Compact Laboratories from Design to Application

Direttore della Scuola: Ch.mo Prof. Gaetano Granozzi
Supervisore: Ch.mo Prof. Michele Maggini

Dottorando: Simone Silvestrini

Dicembre 2011

To my father.

Summary

Riassunto

Questa tesi è un riassunto delle più rappresentative attività sperimentali svolte dall'autore nel triennio 2009-2011 presso i laboratori del dipartimento di scienze chimiche dell'università di Padova, sotto la supervisione del prof. M. Maggini. Il filo conduttore che lega le tematiche toccate dal presente lavoro è la tecnologia microfluidica, intesa come insieme di tecniche per la manipolazione dei fluidi su scala micrometrica. Tale manipolazione avviene all'interno di microcanali, ambienti confinati nello spazio la cui geometria può essere sfruttata per ottimizzare operazioni unitarie – quali il mescolamento e il trasferimento di calore – di profondo interesse dal punto di vista chimico.

Una porzione importante di questo elaborato è dedicata alle tecniche di microfabbricazione per la prototipizzazione rapida di chips microfluidici, un tema sviluppato costantemente durante tutto l'internato di tesi. I protocolli sviluppati per la fabbricazione di interfacce con l'ambiente esterno, di microcanali e di elettrodi, sono riportati punto per punto e commentati in modo da permetterne una fedele riproduzione. Due tecniche largamente sfruttate sono la fotolitografia "soft" e l'embossing. La prima si basa sulla fotopolimerizzazione di resine commerciali (in particolare di tipo tiolenico), utilizzando una maschera disegnata al computer e stampata su acetato per imprimere un disegno sul materiale polimerico e ricavarne quindi dei canali. La seconda prevede l'uso di un plotter da taglio per lavorare materiali quali nastri biadesivi o film di cera dai quali ricavare direttamente le microstrutture desiderate.

La resina tiolenica commerciale NOA è anche al centro di due lavori sperimentali riguardanti gli aspetti più chimici della prototipizzazione: la resistenza ai solventi e la bagnabilità. Fra i requisiti principali di un materiale per la fabbricazione di reattori chimici, c'è senz'altro la resistenza ai solventi utilizzati nelle sintesi per cui il reattore stesso deve essere utilizzato. Nonostante la resina in oggetto presenti caratteristiche di compatibilità interessanti, soprattutto se confrontata con altri materiali tipicamente usati in microfluidica, quali il poli(dimetilsilossano), la sua resistenza verso i solventi alogenati non ne consente un ampio uso in ambito sintetico. La deposizione di uno strato di silice, ad ogni modo, ha permesso di aumentare la sua resistenza, pur non rendendola completamente resistente. Altra caratteristica importante, in quanto controlla l'interazione fra solvente e superficie interna del reattore è la bagnabilità. Nel caso del NOA, si dimostra come essa possa essere controllata derivatizzando la resina grazie alla condensazione dei gruppi idrossili superficiali con derivati triclorosilani.

La possibilità di produrre rapidamente dispositivi microfluidici ha portato allo sviluppo di varie applicazioni, le più interessanti delle quali sono descritte nella terza parte della tesi.

Innanzitutto viene dimostrato come un elegante dispositivo fabbricato con un materiale ceroso molto comune come il Parafilm, possa essere utilizzato per la sintesi parallela di diversi coloranti diazoici attraverso una sintesi multistep che prevede la produzione in ambiente confinato di un intermedio potenzialmente esplosivo come un sale di diazonio.

In seguito viene descritta l'applicazione di una cella a flusso interfacciata a uno spettrofotometro, con cui si possono ricavare interessanti informazioni sulle cinetiche di adsorbimento di sensibilizzatori sulla superficie dell'ossido di titanio. Tale processo è di interesse generale, essendo alla base della produzione delle celle fotovoltaiche a colorante organico.

La trasparenza ottica della resina tiolenica NOA viene poi sfruttata per condurre reazioni fotochimica all'interno di canali microfluidici fabbricati in questo materiale. Luci monocromatiche "fredde" LED vengono qui usate per direzionare il fenomeno di crescita di nanostrutture metalliche, producendo nanoparticelle di forma e dimensioni controllate.

La possibilità di fabbricare elettrodi direttamente all'interno di canali ha avuto come sbocco naturale la costruzione di dispositivi per elettrochimica. Quello presentato in questa tesi è stato progettato per compiere misure di spettroscopia elettrochimica di impedenza e ne viene presentata la fabbricazione e la caratterizzazione elettronica di base.

L'ultima parte della tesi riporta gli studi cinetici relativi a due importanti reazioni nell'ambito della chimica dei fullereni: la cicloaddizione di speci 1,3-dipolari alla gabbia fullerenica (reazione di Prato-Maggini) e la reazione di ciclopropanazione con derivati bromomalonati (reazione di Bingel-Hirsch). L'interesse dietro a questi studi è duplice: da un lato studiare queste reazioni fornisce dati interessanti per un confronto critico fra la chimica condotta in flusso e quella condotta con tecniche tradizionali, d'altra parte studi di tipo cinetico su queste due reazioni non sono presenti in letteratura nonostante l'indiscussa utilità delle reazioni suddette.

Abstract

This doctoral thesis resumes the most interesting experimental results achieved between 2009 and 2011 by the author, during his stay in the laboratories of the department of chemical sciences of the university of Padova, under the supervision of prof. M. Maggini. The main theme behind this work is microfluidics, an ensemble of techniques for the manipulation of fluids on the micrometer scale. Such manipulation is carried out inside microchannels, confined environments whose geometries can be exploited to optimize unit operations – such as mixing and heat transfer – of profound interest for chemists.

Microfabrication is the first theme treated, and one that has been constantly developed during this internship. The fast prototyping of microfluidic chips is described thoroughly, from the fabrication of chip-external world interfaces, to that of microchannels and electrodes, in order to allow for their easy reproduction. Two techniques widely employed were soft photolithography and embossing. The former makes use of photocurable resins, in particular thiol-ene ones, employing masks to copy a design to the resin bulk in order to make the channels. The latter is based on the use of a cutting plotter to work directly on the materials the microchannels are made of, such as biadhesive tapes and Parafilm M laboratory film.

A commercial thiol-ene resin, NOA, was the object of two experimental works: one aimed at increasing its solvent resistance and the other at achieving wettability control for its surfaces. Solvent resistance is possibly the foremost requirement for a chemical reactor; while NOA displays better chemical compatibility towards organic solvents than other materials commonly used for microfluidic applications, such as poly(dimethylsiloxane), its scarce resistance towards halogenated solvents is a drawback for its employment. The deposition of a silica layer proved to ease this problem, even though it did not solve it, by extending the working life of microchannels made in polymeric material when aggressive solvents were used.

Another interesting characteristic is wettability, which controls the interaction between solvent and the reactor's inner surfaces, playing an important role in the flow characteristics of the device. To control this feature, NOA was functionalized by silanizing the hydroxide groups on its surface by condensation with trichlorosilane derivatives. A demonstrator device consisting in a passive valve that can discriminate between aqueous and organic liquids was fabricated in a few hours thanks to this method.

Being able to quickly produce microfluidic devices led to the development of various applications, the most interesting of which are reported in the third part of the thesis. As a first

example, a very common laboratory material such as Parafilm M was used to fabricate an elegant microreactor capable of producing two diazo dyes in parallel, in a multistep synthesis whose first step relies on the production in confined environment of an intermediate (diazonium salt) which is potentially explosive.

Next, a flow cell interfaced with a spectrophotometer is described, which was used for the study of adsorption kinetics of organic dyes (photosensitizers) on porous titanium dioxide. Such process is of general interest, being a fundamental step in the fabrication of dye sensitized solar cells.

The optical transparency of NOA resins is exploited in the third application presented: a microreactor that was used to carry out photochemical reactions. Light emitting diodes were used as cold, highly efficient light sources to direct the growth phenomena of metal nanostructures, to produce silver nanoparticles with controlled sizes and shapes.

The same masking technology developed for photocurable materials was also exploited to produce gold electrodes. A microfluidic device for electrochemical impedance spectroscopy was then developed and a description of its design, production and electronic characterization is reported at the end of the third section.

Finally, the last part of the thesis report two kinetic studies carried out on important processes for fullerene chemistry: a 1,3-dipolar cycloaddition of azomethyne ylides (the Prato-Maggini reaction) and a cyclopropanation reaction to the fullerene cage with bromomalonate derivatives (the Bingel-Hirsch reaction). The interest behind these studies is two-fold: i) they allow a critical comparison between batch and flow chemistry and ii) notwithstanding the widespread employment of these two reactions in chemical laboratories, few kinetic studies are available on the subject.

Abbreviations

ATR	Attenuated Total Reflectance
CAD	Computer-Assisted Design
CFD	Computational Fluid Dynamics
DBU	1,8-diazabicyclo[5.4.0]undec-7-ene
DCM	Dichloromethane
DMF	Dimethylformamide
DSSC	Dye-Sensitized Solar Cell
FT-IR	Fourier Transform Infrared
FTO	Fluorine-doped Tin Oxide
HPLC	High Pressure Liquid Chromatography
ITO	Indium Tin Oxide
LED	Light Emitting Diode
LOAC	Lab On A Chip
MEMS	Micro Electro-Mechanical Systems
MR	Micro Reactor
MFD	Microfluidic Device
(Ag, Au, Cu)NP	(Silver, Gold, Copper) Nanoparticle
µTAS	Micro Total Analysis System
NOA	Norland Optical Adhesive
ODCB	1,2-dichlorobenzene
OTS	Octadecyl Trichlorosilane
PCE	Photo Conversion Efficiency
PDMS	Poly(dimtheylsiloxane)
PTFE	Poly(tetrafluoroethylene)
PTS	2-[methoxy(polyethylenoxy)propyl]trichlorosilane

PVD	Physical Vapor Deposition
SAD	Selected Area Diffraction
STY	Space Time Yield
TEM	Transmission Electron Microscope
TEOS	Tetraethyl Orthosilane
UV	Ultraviolet
WCA	Water Contact Angle

0. Foreword

“How much can the vessel in which a chemical reaction is run affect the reaction itself?”. This is one question I asked myself when I undertook my PhD project. After taking up many laboratory courses, I was to start back from the very basics of lab activities, which are overlooked most of the time: labware. Most of the reactions routinely carried out in research laboratories make use of glass round bottom flasks, with volumes ranging from 5 mL to 5 L. Glass is usually considered to be inert during the reaction, or is rendered so (through the chemistry chlorosilanes, for example), mixing is provided by Teflon-coated magnetic bars and oil/ice baths allow for heating/cooling when necessary. The processing of starting materials into products is carried out *batch*-wise, in a discontinuous way, since only relatively small amounts of product are usually needed and the reaction setup can be easily modified. Continuous flow setups are rarely employed in academic laboratories.

The demands of industry are quite different from those of the research laboratory. The need for performance drives the industrial practice towards the use of larger, continuous reactors and to consider heat and mass transfer more closely in order to optimize every step of a reaction. The *scaling up* of processes is an expensive and time consuming task. As such, months can be necessary to successfully bring a reaction from the lab to the industry. Several steps are usually required, starting from the design of a continuous process based on the discontinuous lab example and moving to sheer size increase.

A completely different solution for the translation of laboratory reactions to full-fledged production techniques has been probed in the last two decades: the microfluidic approach. Here, chemistry is carried out in microstructured reaction vessels in a continuous way, which means ease of adaptability to large scale production, via *numbering-up* of production modules, while bringing about a number of advantages on both industrial and lab scale, like a great ease of control over reaction parameters such as temperature, mixing and residence times. It is indeed surprising that microfluidic techniques have begun receiving intense worldwide attention from the chemical scientific community in the last fifteen years only. At the present time, flow techniques are mostly appreciated by the pharmaceutical industry, which is, typically, the most active in research and development.

This doctoral thesis is a collection of microfluidic methods for synthesis and characterization purposes. I have been fortunate enough to follow the entire process of problem solving, starting from the setting up of a cleanroom facility for the production of microstructured surfaces, to device design, prototyping, testing and use to generate useful scientific data.

Furthermore, the problems I faced during my 3-years stay at the Chemical Sciences Department of the University of Padova were very diverse, ranging from the surface chemistry of polymeric materials, to organic chemistry kinetic studies, production of carbon and metal nanostructures, electrosynthesis and electroanalytical chemistry.

Structure of the thesis

Chapter one begins by outlining the state of the art of microfluidic technology with particular emphasis on applications in the field of chemical synthesis. It also provides an introduction to the physics describing the properties of microfluidic devices and makes critical comparisons with traditional "bulk" systems.

Chapter two deals with the fast prototyping techniques that were developed during the course of this doctoral thesis. It reports a step by step description of the procedures that were employed to fabricate the devices used for the production of scientific data in later chapters.

Chapter three presents a number of applications of prototype devices for scientific purposes, ranging from electro-analytical chemistry to chemical synthesis and spectroscopy.

Chapter four compares the kinetics of reactions carried out in batch and flow conditions, a convenient way to rationalize the differences between "flask" and "flow" chemistry.

On pictures and images

Every microfluidic device pictured in this thesis has been fabricated by the author, except where otherwise indicated.

1. Introduction

The advent of miniaturized electronics in the second half of the twentieth century quickly changed our lifestyles. Small, portable devices such as music players, remote controllers and mobile phones have had a strong impact on the way we live and communicate, but also sport a lower energy consumption and better performances than their larger (and older) counterparts. Much in the same fashion, the scientific community is seeing the emergence of micro electro-mechanical systems (MEMS), electricity-driven mechanical devices whose size is of the order of 1 – 100 µm. Microfluidic technology is often regarded as a subcategory of MEMS, dealing the handling of fluids in small volumes. Many classical chemical techniques, like high pressure liquid chromatography (HPLC) or even filtrations, could in principle be considered microfluidic, in that they assume a fluid passing through a packed medium which results in channels with a width of the order 10^{-6} m. However, the typical microfluidic device (MFD) consists in an ordered pattern of channels with micrometric size, such as those pictured in figure 1.1 and an interface with the external environment in order to be connected to a fluid management apparatus (i.e. pump). Other elements, such as functional surfaces and electrodes can also be part of the device and may serve to carry out specific tasks, resulting in what is termed a *lab-on-a-chip* (LOAC).

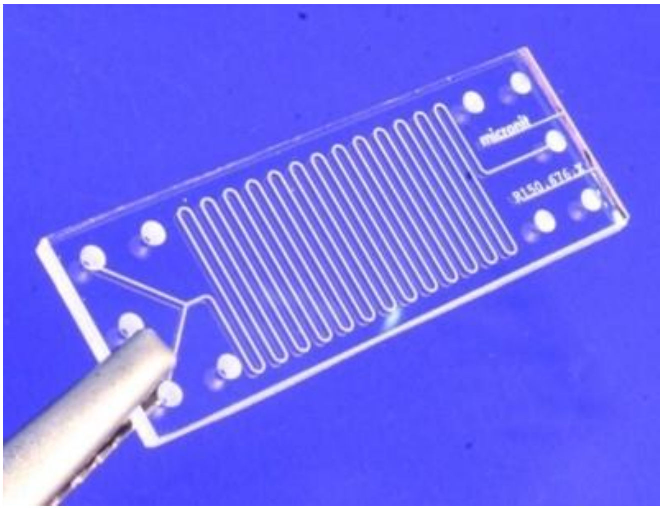

Figure 1.1 Commercial glass microfluidic chip by Micronit Microfluidics BV. The microfluidic channels have a square section with a side of 150 µm and the total internal volume is 6 µl.

1.1 State of the art – an overview

The first LOAC analysis system was a gas chromatograph, developed in 1979 by S.C. Terry at Stanford University[1] but the field was further developed only from the nineties, when the term micro total analysis system (µTAS) was forged.[2] The first examples of LOACs were reported in literature for sensing purposes, and soon became important interdisciplinary tools. In his 2009 article on Nature Chemistry, deMello notes how microfluidics is yet another trend in the "general drive in chemistry and biology to harness the effects of small scales on the way matter behaves".[3] Biological applications were indeed the first to benefit from LOAC technology, as exemplified by the scientific production of G. Whitesides, who envisioned a range of paper-based, low-cost medical analysis applications for use in developing countries.[4] The main advantages claimed by µTAS are quick and reliable analyses, carried out in short times over a small volume of sample by field-deployable, low cost devices. Another classical example of the potentiality of MFDs was reported by Whitesides' alumnus, R. Ismagilov, who showed how proteins could be conveniently crystalized for X-ray crystallographic analysis in a MFD, employing a so-called segmented flow to produce a series of isolated droplets of very small volume, each acting as a separate chemical reactor for crystallization.[5] Chemical synthesis can also benefit from the use of microreactors, as widely reported by the group led by professor S. Ley, where continuous flow syntheses are critically employed to carry out selected synthetic steps in the synthesis of complex organic structures.[6]

The availability of commercial microfluidic platforms and the rapid development of accessible prototyping techniques to fabricate custom microfluidic devices, has led to an increased interest towards every aspect of this new approach to chemical problem solving, from the description and modeling of flows in the micro-scale, to applications in the field of chemistry and biology. Literature reflects the interest in this field, with a whole issue of Chemical Society Reviews being devoted to microfludics[7] in 2010 and an impact factor of 6.26 for the journal "Lab on a chip", possibly the foremost publication dealing with microfluidics applications. The flow chemistry society was also founded in 2010 and started publishing the Journal of Flow Chemistry soon after.[8]

Notwithstanding the quick inflation of the related literature, microfluidics cannot offer solutions to all chemical problems and some authors go as far as to highlight the need for a more critical approach to this technology, as suggested by the title of the 2010 article on Angewandte Chemie Int. Ed. authored – among the others – by D. G. Blackmond and J. Cabral: "The flow's the thing… Or is it? Assessing the Merits of Homogeneous Reactions in Flask and

Flow".[9] The most correct description for microfluidics is perhaps that of a collection of enabling technologies, that allow for a precise control of the experimental environment up to the point making it possible to carry out processes in condition not before possible.

1.2 Microfluidic setups

Microfluidic setups can be categorized according to a number of criteria. A first distinction can be made regarding the scale of the system being considered: while the general description of MFDs given earlier in this chapter states that the channels have sub-millimeter lateral dimensions, many advantages for synthetic chemistry typical of the microfluidic conditions can still be observed for larger scales, up to a few millimeters. A definition of *meso*-fluidic systems would be more appropriate for commercial systems such as Vapourtec's R series flow reactor[10], or the Corning's Low Flow system[11] (both can be seen in figure 1.2). In this regard, in most cases that category is considered to be comprised in that of microfluidics. Working with larger channels result in larger reactor volume, so that more starting materials can be processed. Unsurprisingly, this "*meso*" approach is more often found in the field of chemical synthesis, particularly for industrial applications. Indeed, many published studies demonstrate how only minimal adaptations are required in order for microfluidic syntheses to be run on such relatively larger scales.[12]

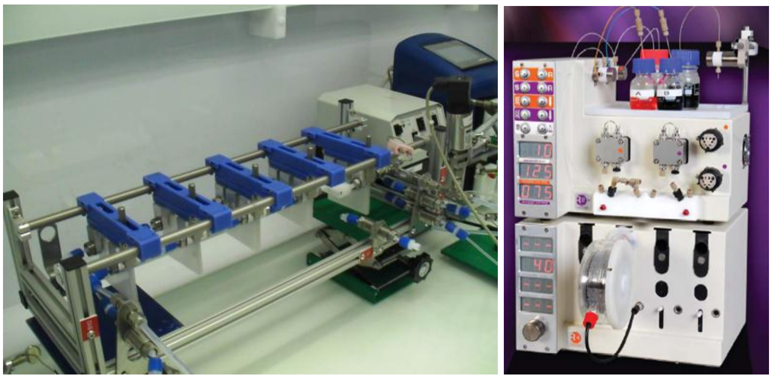

Figure 1.2. Two examples of commercial flow reactors: Corning's Low Flow (left) and Vapourtec R series reactor (right)

Another distinction could in principle be made between MF systems being operated on a chip and those consisting only in tubes and fittings. The simplest setups for chemical synthesis consist in just a "mix & heat" system. Batch reactions on the laboratory-scale can be run in a beaker (just like in figure 1.3a), or in a round bottom flask (vessel) with a stirring bar (mixer) and a heating plate (temperature control). The corresponding flow setup consists in pumps, connected via a "T" or "Y" junction (mixing) to a channel of a given length (vessel) passing in a hot bath (temperature control). The junction can be either in a microfluidic chip (figure 1.3b), or consist just of an HPLC-type standard junction (figure 1.3c).

A chip usually encompasses both the mixing element and the vessel, so its internal volume is set upon fabrication. On the contrary, working with HPLC junctions followed by tubing allows to change the vessel, resulting in a more flexible approach. In particular, the volume of the vessel defines the residence time when working at constant flow rate, which is one of the most important parameter in a chemical reaction.

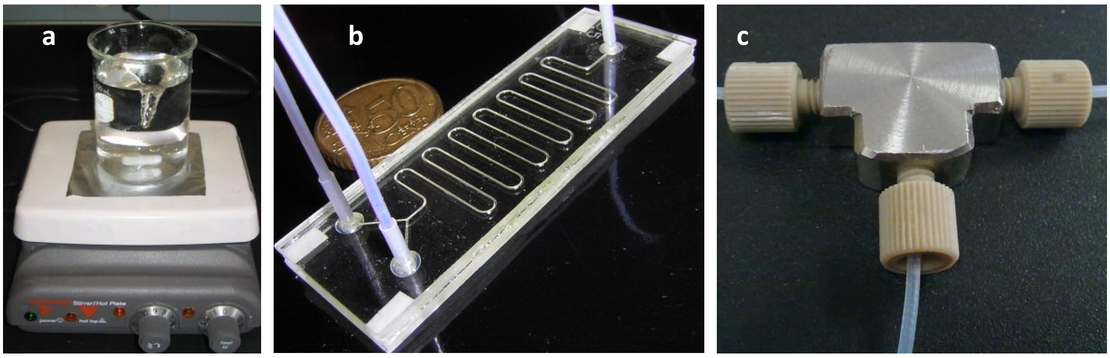

Figure 1.3. “mix & heat” experimental setups: a) beaker, stirring bar and heating plate; b) Y-junction microfluidic chip; c) T-junction made in stainless steel with PEEK fittings (commercialized by Upchurch Scientific).

For “mix & heat” applications, a Y-junction setup is quicker to assemble and its parts can be replaced and cleaned more easily than those of a MF chip. Some advantages of the chip are its elegance, which may play a role as an educational tool, its transparency, allowing to see through the reactor in order to spot the buildup of solids or perform spectrophotometric monitoring of the process. Another possibility given by the chip setup is the implementation of elements inside the microchannels in order to broaden the device’s fields of application, for example optical fibers and electrodes.

Moreover, a microfluidic setup can be a proper LOAC, with all its working parts on a single device, or built as a modular system, with different, interfaced microfluidic devices each carrying out a specific task or unit operation. Both the LOAC and the modular approaches have their up and downsides. A true LOAC is in principle a black box device that can be employed by just about any operator regardless of his or her knowledge of chemistry. The device will, however, only carry out the very specific task it has been designed for, with very limited flexibility. On the other hand, the modular microfluidics approach closely resembles the compartimentalization of industrial plants, offering a series of tools that must be understood, connected and operated properly by educated personnel.

Lastly, there are two main methods in which the liquid flows can be managed in the microchannels: continuous and segmented flows. In continuous flow devices, exemplified in figure 1.4a, a single liquid phase homogeneously fills the device from inlet to outlet. On the contrary, in a segmented flow, droplets of one phase – generally the one flowing at lower flow rate – are carried along the channels by the other phase. The relative flow rate and the geometry of both the channel and the droplet generator (the area of the MFD where the droplets form) control the characteristics of the train, such as droplets volume and size distribution. Droplets can be engineered in order to be permeable or impermeable to their surrounding medium, which is a very important feature for their use as synthetic tools, and their *cross-talking* (diffusion of species between droplets) can be controlled as well.[13]

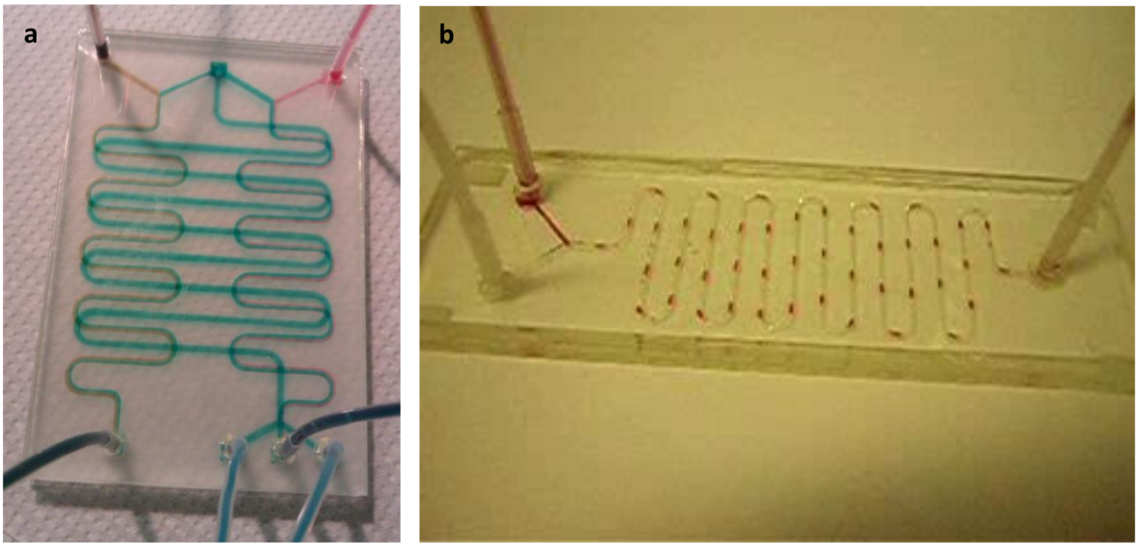

Figure 1.4. Types of flows. a) Continuous flow of different colored inks; b) Segmented flows of two immiscible phases: sodium dodecylbenzosulfate in water (clear) and tetraphenylporphyrin in dichloromethane (red).

Simple designs allow to produce droplets at rates up to a few kHz (thousands of droplets per second), so analytical methods based on this technology can benefit from extremely large number of samples that allow for interesting statistical data treatment. The precision associated with a measurement, for example, increases with the square root of the number of repeated tests, meaning that a segmented flow device operating at 2kHz has a 100-fold precision increase over a single-measurement test after a 5 seconds run.

As chemical reactors, MFDs operating with a continuous phase can be described as plug flow reactors (PFR), while each droplet in a segmented flow behaves like a separate batch reactor (BR) with the increased benefit of being generated continuously. The employment of segmented flow techniques for chemical synthesis on large scales, however, can be hindered by the presence of two phases, which implies the need for an extra separation step at reaction workup, possibly followed by purification of the solvents before recycling.

1.3 Physical description of microfluidic devices

The behavior of fluids in a MFD is dictated by the high surface-to-volume ratio highlights surface properties of the materials, such as wetting and electrostatics, overshadowing volume-related properties, like inertia. In the following paragraphs I will recollect the fundamental physical laws that come in handy to describe and understand the properties of MFDs.

Hypotheses

All through this thesis I will deal with uncompressible liquids, so that the divergence of the field of velocity $\vec{u}$ is null:

$$\vec{\nabla} \cdot \vec{u} = 0 \tag{1.1}$$

Also, the Knudsen number, the ratio between the molecular mean diffusion path length λ and a characteristic linear dimension of the system *L* will always be lower than 1,

$$Kn = \frac{\lambda}{L} < 1 \tag{1.2}$$

so that the hypotheses of continuum apply and there is no need for statistical mechanics to describe the behavior of the system.

Navier-Stokes equations

To describe the flow of a fluid means to compute its field of velocities $\vec{u}(x, y, z, t)$, in respect to position (*x, y, z*) and time (*t*). The most general equation set that link this field to the macroscopic properties of the fluid are the Navier-Stokes equations, and they are derived from the continuity equation, the conservation of momentum and the mass balance. They can be written as a single equation, as

$$\rho \frac{d\vec{u}}{dt} = \rho\vec{g} - \vec{\nabla}p + \mu\nabla^2\vec{u} + \frac{2}{3}\mu\vec{\nabla}(\vec{\nabla} \cdot \vec{u}) \tag{1.3}$$

where ρ is the density of the fluid, μ its viscosity, $\vec{g}$ is the acceleration of gravity and p the pressure. In the case of an incompressible fluid, the last term is null, thus equation (1.3) becomes

$$\rho \frac{d\vec{u}}{dt} = \rho\vec{g} - \vec{\nabla}p + \mu\nabla^2\vec{u} \tag{1.4}$$

Mathematicians have not yet proved that smooth solutions to this set of differential equations always exist, or that, if they do, they have physical meaning. This is called the Navier–Stokes existence and smoothness problem and is numbered, by the Clay mathematics institute, in the list of the greatest mathematical problems still unsolved.[14] Even in their differential form, the Navier-Stokes equations are useful for the solution of hydrodynamic problems.

Computational fluid dynamics (CFD) techniques rely heavily on the numerical solution of these equations to precisely simulate the behavior of fluid masses and thus constitute a powerful tool for physicists, chemists and engineers alike.

Fluid motion in microfluidic conditions

Some considerations can be made on the flow inside channels with linear dimension of the order of tens to hundreds of micrometers. The Reynolds number, Re, is an adimensional quantity that gives a measure of the ratio of inertial forces to viscous forces:

$$Re = \frac{\rho|\vec{u}|l}{\mu} \tag{1.5}$$

Its value is used to discriminate between laminar ($Re < 2.3 \times 10^3$) and turbulent ($Re > 4 \times 10^3$) flow regimes (for $2.3 \times 10^3 < Re < 4 \times 10^3$, a "transitional" flow is considered and both regimes are actually possible) to assay one of the most interesting properties of a flowing system. Figure 1.5 reports a Re *versus* flow rate diagram for a channel of infinite length, with round section and a diameter of 250 µm (typical size for GC fused silica capillaries), assuming the steady state flow of a liquid similar to water and most of the common solvents used for organic synthesis, which densities lie in the 0.8 – 1.4 g/ml range, and dynamic viscosities in the 0.5 – 1.5 cP range.

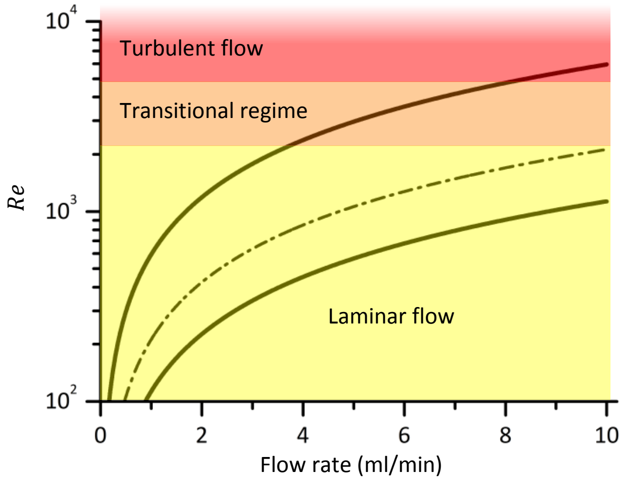

Figure 1.5. Typical Reynold's numbers, Re, as a function of the flow rate in a round channel of infinite length and a diameter of 250 µm. The dash-dot curve represents values for water at 25 °C.

The value of Re for microfluidic systems is typically very low, ensuring a completely laminar flow inside the channel. In such simple cases, the field of velocities can be derived from the general equation of transport. The field is cylindrically symmetric around the axis of the channel and the velocity profile is parabolic, as shown in figure 1.6. The field $\vec{u}(x, y, z, t)$

actually becomes $\vec{u}(r)$, *r* being the distance from the axis, and can be expressed by Poiseuille's law:

$$|\vec{u}| = -\frac{\rho}{4\mu}\frac{\Delta p}{\Delta x}(R^2 - r^2) \tag{1.6}$$

where R is the channel radius and $\frac{\Delta p}{\Delta x}$ is the pressure gradient along the conduit. The fluid motion can be described as an infinite number of concentric, cylindrical lamellae slipping relative to one another. At the wall of the channel *R* equals *r*, thus the velocity is null. This is called *no-slip condition* and is a boundary condition commonly considered when integrating the equations that lead to equation 1.6. The slipping conditions at the channel walls have been and are still matter of debate for physicists [15-17] but, for the sake of this thesis, I will stick to the classical approach to transport phenomena and assume the no-slip boundary condition.

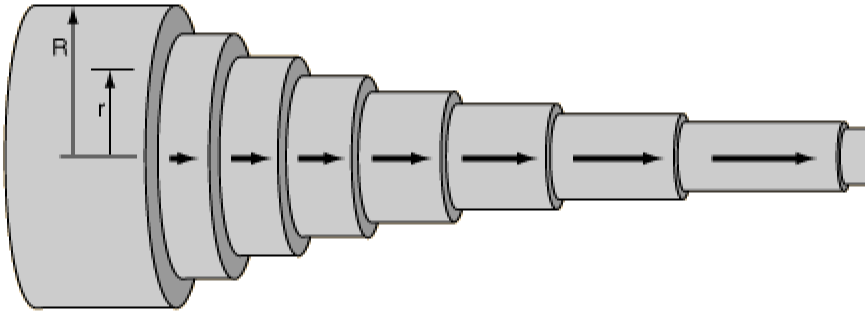

Figure 1.6. Parabolic velocity profile in a cylindrical conduit, as described by Poiseuille's law (equation 1.6)

The value of Re is not only important in defining the type of flow inside a conduit, but it also appears in the empirical equations that model the flow of extensive physical properties in a body of fluid, such as mass (describing mixing) and energy (describing heat exchange). The description given so far is not exhaustive, in that the microchannels section is only rarely round and never infinite in length. Moreover, various degrees of turbulence are induced by bends in the channel path, external interfacing (inlets and outlets) and other structures.

A low Reynolds number is often desirable because the lack of turbulence minimizes pressure drops and backmixing phenomena, but it also severely hinders mixing, as exemplified in figure 1.7, and heat exchange performances, that can only take place by diffusion as opposed to convection. a typical experiment What is probably most important, though, is that the laminar flow allow for a steady state description of the system (the time variable does not appear in the velocity field expression) thus greatly simplifying the understanding and the design of microfluidic experiments. Even when turbulent flows are desired, they can be generated in selected section of the conduit by different means – for example by bending the channel – and modeled precisely thanks to the physical simplicity of the surroundings.

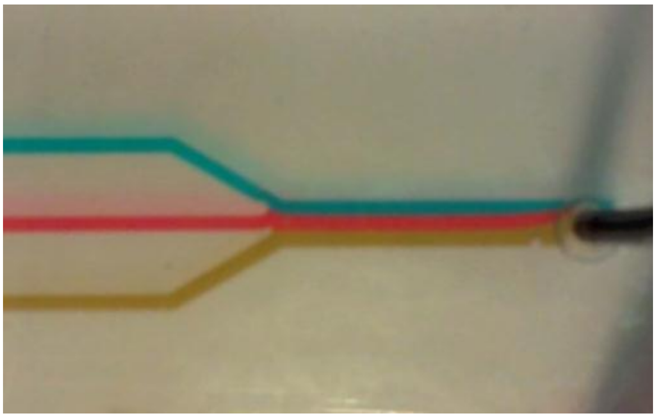

Figure 1.7. Mixing (or lack thereof) in laminar flow regime. The three flows were colored with India ink and keep flowing parallel to each other even when in contact.

Residence time

As a first approximation, the residence time rt of an element of fluid moving inside a channel, from an inlet to an outlet, can be calculated as the ratio between the volume of the channel itself, V, and the flow rate Q (expressed as volume over time):

$$rt = \frac{V}{Q} \tag{1.7}$$

This definition would be realistic if all the fluid elements in the channel moved at the same linear velocity. As shown in the previous paragraph, however, in a round channel the velocity varies with the distance from the axis. Thus, it is common practice to term the ratio between channel volume and flow rate the *mean* residence time, or τ, and to consider a residence time distribution (RTD) for fluid elements, $E(t)$, which is a probability distribution function that describes the amount of time a fluid element could spend inside the reactor. In particular, the integral $\int_{t_1}^{t_2} E(t)dt$ represents the fraction of fluid whose residence time is between t_1 and t_2. Günter et al. reported a convenient system for the experimental determination of $E(t)$ and found that the RTD of a 50 mm long Teflon tube with a diameter of 500 µm and a flow rate of 100 µl/min closely resembles that of an ideal laminar flow reactor with axial dispersion.[18] The RTD in this ideal case is described by the following:

$$E(t) = \frac{1}{2}\left(\frac{Bo}{\pi\left(\frac{t}{\tau}\right)}\right)^{1/2} e^{\left(\frac{Bo\left(1-(t/\tau)\right)^2}{4(t/\tau)}\right)} \tag{1.8}$$

where Bo is the Bodenstein number, inverse of the Peclet number Pe, which describes the magnitude of convection with respect to diffusion:

$$Pe = \frac{|\vec{u}|l}{D} \tag{1.9}$$

$|\vec{u}|$ being the velocity of the liquid, l a characteristic length and D the diffusion coefficient. The diffusivity of water in water is assumed to be 10^{-9} m^2/s and, for a 1 m long round conduit with l=250 µm and a flow rate of 100 µl/min, $|\vec{u}|$ = 0.849 m/s, so that Pe = 2.122 × 10^3.

For a given species being injected in the tube, the concentration at the outlet, $c_{out}(t)$ can be written as the convolution of its concentration at the inlet, $c_{in}(t)$ and the residence time function $E(t)$,

$$c_{out}(t) = \int_0^t x(t-t')E(t')dt' = \int_0^t x(t')E(t-t')dt' \qquad (1.10)$$

The comparison between the plots of $c_{in}(t)$ and $c_{out}(t)$, presented in figure 1.8, gives a good idea of the behavior of a microchannel, in particular regarding the error that is made by employing equation 1.7. In the example reported, $c_{in}(t)$ is a step function, equal to the molarity of water (55.5 mol/l) for 1 second starting at t = 0. τ = 117.8 s.

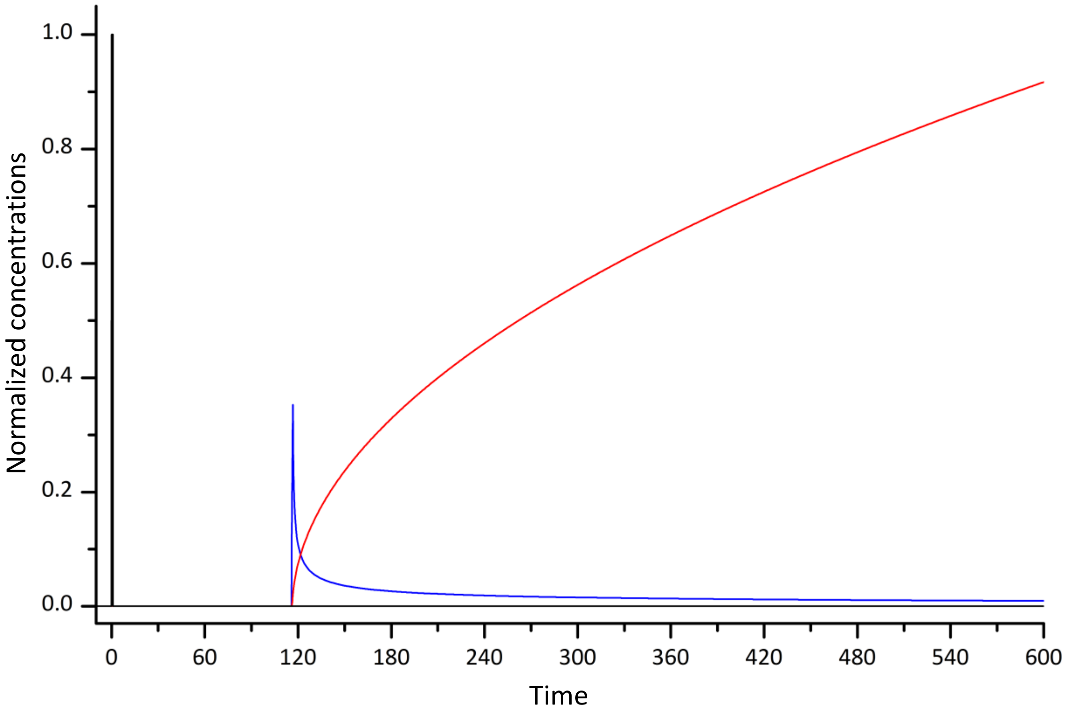

Figure 1.8. RTD for a water flow in a 1 m long, round channel with a diameter of 250 µm at 100 µl/min flow rate. In black, the normalized concentration at the inlet, in blue is the normalized concentratrion at the outlet, in red is the fraction of the injected material that has exited the tube at a given time.

In equation 1.7, it is possible to substitute the volume of the channel with the product of its cross section Σ and its length l, getting

$$\mathrm{rt} = \frac{\Sigma \mathrm{l}}{Q} \qquad (1.11)$$

While this relationship may appear trivial, it outlines one of the most interesting properties of MFDs: the *time-length equivalence*. It is indeed possible to substitute the mean residence time of the fluid at a certain position along the channel, with the position itself multiplied by a scale factor which depends on the geometry of the system only. For most chemical applications, this also means that, during operation, each position along the channel is at steady state and its properties do not change over time.

Mass and heat transfer

Mass and energy are extensive properties and their transport is described by the general equation

$$\vec{\Gamma} = -\delta\vec{\nabla}\psi \tag{1.12}$$

where $\vec{\Gamma}$ is the flow of the extensive property, $\vec{\nabla}\psi$ is the gradient of the relative intensive property and δ is a proportionality factor, called the resistance. Applying this equation to the fields of concentration C and temperature T, yield the following equations:

$$Q = k\frac{dT}{dx} \tag{1.13}$$

$$J = D\frac{dC}{dx} \tag{1.14}$$

where the flows are expressed along a single direction, x. Equation 1.13 is the Fourier law for heat conduction, where Q is the heat flow per unit area and k is the thermal conductivity; equation 1.14 is the Fick law of diffusion at stationary state (usually called Fick's *first* law of diffusion), where J is the molar flow and D the diffusivity of the species in the medium. The similarity between these two differential equations ensures that the solutions to mass and thermal flow problems are very similar. Equation 1.13 can be used to calculate the amount of heat passing through a surface (most notably, the interface between two bodies held at constant temperatures), to yield

$$\frac{dq}{dt} = h_q a\Delta T \tag{1.15}$$

where a is the specific area over which the flow takes place, ΔT is the temperature difference between the two bodies and h_q is the thermal conductance coefficient. h_q represents the inverse of the ratio between the temperature drop and the average heat flow across the interface and can be estimated with empirical equations.

For diffusive mass transfer, equation 1.14 yields

$$\frac{dC}{dt} = h_c a\Delta C \tag{1.16}$$

here, h_c represents the mass transfer coefficient, with similar meaning as h_q in the case of heat flow.

Mixing

Mixing is a critical parameter for chemical applications, since the models describing chemical reactivity hypothesize perfectly mixed systems. In MFDs working in laminar flow conditions, diffusion is the only phenomenon contributing to the mixing of the species in the conduits and the magnitude of its effects can be evaluated by equation 1.16. In a MFD, the elements providing mixing that are only based on diffusion are called *passive* mixers and their performance is optimized by improving the specific area of contact (a, in equation 1.16) between different streams. The basic mixing design is the so-called T-junction, shown in figure 1.9. The time necessary for one molecule to diffuse over the width w of the channel has direct proportionality to the square of the width itself:

$$\tau_D \propto \frac{w^2}{D} \tag{1.17}$$

where D is the coefficient of diffusion of the molecule. Let $|\vec{u}|$ be the velocity of the stream carrying the molecule, the path L travelled along the axis of the channel over the time τ_D is proportional to the Peclet's number, as defined in equation 1.9.

$$L \propto \frac{|\vec{u}|\, w^2}{D} \equiv Pe \tag{1.18}$$

T-junctions are but the simplest (and least performing) mixer, whereas a plethora of designs are commercially available for passive mixing.[19] Besides the increase in the specific area of contact between the streams, these designs work by generating turbulent flows by means of obstacles and special geometries of the channel network. An analytical description of these mixers is often very complex and engineering methods are usually employed in their study, such as computations flow dynamics simulations.

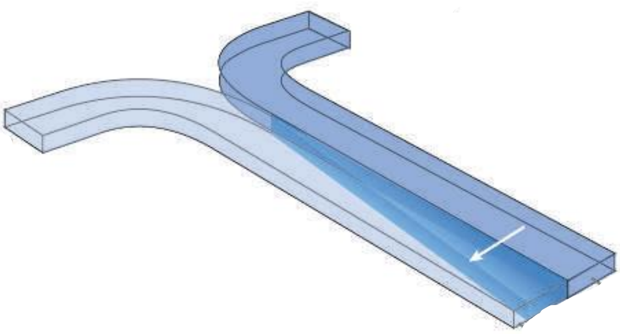

Figure 1.9. T-junction mixer and diffusive mixing.[20]

For tank reactors, the mixing time τ is the time needed to achieve a uniform concentration $\bar{C}$ of a given species over the volume of the container, V_c. At the instant $t < \tau$ a degree of mixing

$\varphi(t)$ can be defined as the complement to the normalized mean squared error of the concentration over the whole reactor volume

$$\varphi_{tank}(t) = 1 - \frac{\int_V [C(x,y,z,t)-\bar{C}]^2 dV}{\int_V [C_0(x,y,z)-\bar{C}]^2 dV} \quad (1.19)$$

where the integral at the numerator runs over the whole container volume and C_0 is the concentration at a given position if no mixing was to occur. In this case, C is a function of both position and time. This concept can be translated to MFD designs, by calculating the mean difference over the section of the channel Σ_c at a given position along the channel axis, z. In this case,

$$\varphi_{MFD}(z \equiv t) = 1 - \frac{1}{\bar{C}} \frac{\int_\Sigma [C(x,y,z\equiv t)-\bar{C}]^2 d\Sigma}{\int_\Sigma [C_0(x,y)-\bar{C}]^2 d\Sigma} \quad (1.20)$$

and the two variables, z and t are freely interchangeable thanks to the time-length equivalence outlined in equation 1.11. Experimentally, φ can be determined by observing the distribution of a fluorescent dye over the section of a channel by means of fluorescence confocal spectroscopy. Channels often have a plane of symmetry perpendicular to the direction of observation, so the dependence of C from the position is further reduced by one degree of freedom. In this case, C is direct proportional to the light intensity measured, as shown in figure 1.10, where a stream of rhodamine dye is mixed with a carbonate buffer solution at a T-junction.

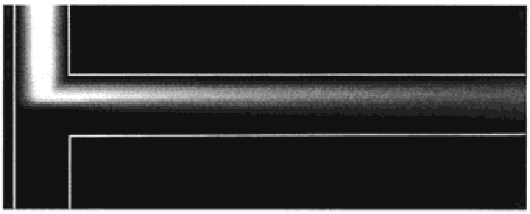

Figure 1.10. Diffusive mixing of rhodamine dye in aqueous carbonate buffer solution. The intensity of each pixel was used to determinate the concentration of the dye.[21]

1.4 Flask *versus* Flow: advantages of MFDs

When microfluidic methods for syntheses and analyses are developed, they are inevitably pitched against traditional techniques. Accuracy, precision, sensitivity and detection limits are key parameters for the validation of analytical techniques that are quite straightforward to assess. Productivity, safety and economy, on the other hand, have to be considered for synthetic applications. This kind of batch *versus* flow comparisons are seldom a trivial task and have led to many misconceptions, as reported by Cabral and coworkers in the review "*The flow's the thing... Or is it? Assessing the merits of homogeneous reactions in flask and flow*"[9].

Comparing “flask” to “flow” is not just about comparing a reaction’s conversion, yield, selectivity and reaction time, even though those are key parameters to describe its outcome. Differences in the aforementioned parameters should always be rationalized and related to the different characteristics of the setups used, in order to produce new knowledge. The general physical description of MFDs given thus far, allow to make some observations about the differences between bulk- and micro- systems. In particular, a number of peculiarities arise from the high specific surfaces of micro-phases, which bring about interesting advantages.

Greater control over reaction parameters

In equations 1.15 and 1.16, the term a indicates the specific surface over which the intensive property (heat, concentration) is transported. The surface area of a cylindrical conduit of length l and radius r is

$$A = 2\pi r \cdot l \qquad (1.21)$$

and the specific area varies as a function of the radius as

$$a = \frac{A}{V} = \frac{2\pi r \cdot l}{\pi r^2 \cdot l} = \frac{2}{r} \qquad (1.22)$$

Larger values of a indicates, for example, that the fluid in the conduit will exchange heat with the external environment more quickly, according to eq. 1.15. Therefore, if heat was generated inside the conduit (i. e. due to an exothermic chemical reaction), raising the temperature of the fluid, the heat exchange with the external environment would be faster for a small channel than for a large one. Likewise, the distribution of temperatures in the channel will be narrower, allowing for a better control of that which is probably the most important thermodynamic variable for a chemical reaction.

A clear description of the effect of a narrow temperature distribution on the outcome of a reaction is given by T. Schwalbe et al. and is reported in figure 1.11. In this example, a reaction is considered where a species A can react to give either B or C, passing through a transition state, either B’ or C’. In the case considered, the energy associated with C’ is larger than that associated with B’. The temperature distributions are considered and plot for a batch reactor (blue), a microreactor (MR, red) and for the ideal case (black) of a very narrow distribution. All distributions are Gaussian curves with the same average value but different widths, so that for the batch reactor the variance is higher.

The temperature of a system and the fraction of molecules whose potential energy is higher than the activation energy of a reaction are closely related by the Boltzmann factor. In particular, the average temperature, in all cases, corresponds to the optimal temperature for the generation of the intermediate B’, eventually leading to the formation of B. Anyway, the wider temperature distribution in the batch reactor, allow an increased fraction of A molecules to cross the potential energy barrier needed for the generation of C’, leading to an increased production of C with a loss of selectivity and performance, when compared to the ideal system. The MR system, on the other hand, performs in quasi-ideal conditions.

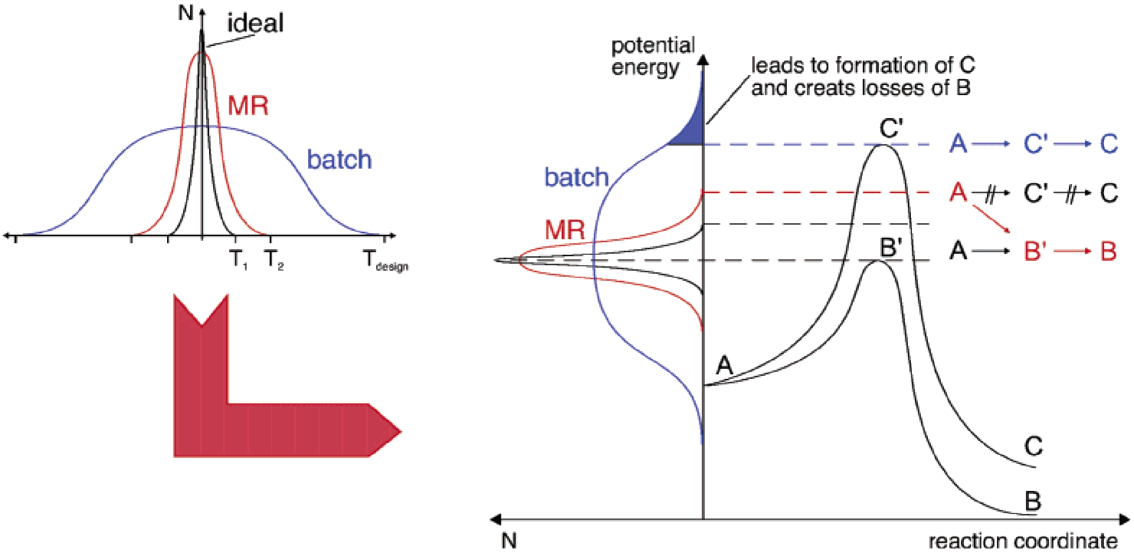

Figure 1.11. Temperature distribution and activation energy. [22]

In an analogous example, reported in figure 1.12, a model multistep reaction,

A → B’ → B → C’ → C

is considered, with the same relative potential energy values of the transition states. In this case, B is the target product and is formed first in both the batch and microfluidic reactors, but then is consumed quickly in the batch reactor where the temperature distribution allows for an easier formation of C.

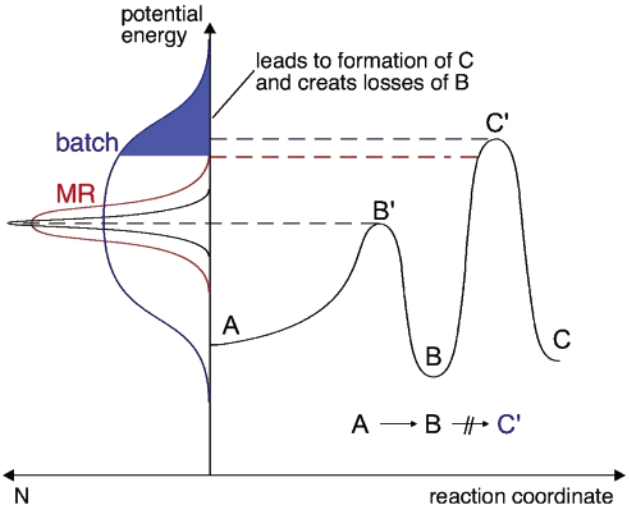

Figure 1.12. Suppression of follow-up reactions by exact adjustment of the inner temperature in a two-stage process. [22]

While equation 1.16 closely resembles equation 1.15, the comparison of mixing capabilities of MFDs and traditional batch reactors must take into account that in the latter, mixing is governed by convection thanks to the use of a stirrer, like a magnetic bar, while the former only depends on diffusive mixing as described in the previous paragraph. It is a common misconception that the use of a MFD implies better mixing performances in an experiment. This is not always the case, since diffusive mixing is always slower than its turbulent counterpart. The real advantage of MFDs is the degree of control that can be accessed and the ease of modeling of the mixing phenomena, which makes optimization easier. A bulk, continuous stirred tank reactor (CSTR) is considered in an ideal mixing regime when the characteristic mixing is at most one fifth of the mean residence time and the typical mixing time for a round bottom flask with magnetic stirring is in the order of a few seconds. Indeed, a typical indication for undergraduate students who are trying out acid-base titrations for the first time, is to add the titrating agent slowly once close to the end point, allowing a few seconds to pass between each added drop in order for the pH to stabilize all over the mixture.

The simplest passive mixer, a T-junction, provides a mixing time of the same magnitude as a stirred round bottom flask but, as mentioned, many mixers are available whose mixing times are orders of magnitude smaller. One such example is the device reported in figure 1.13, where the two streams are divided in 16 equal parts which are then brought into contact as thin lamellae, increasing the specific area and the rate of mixing. This specific device claims a mixing time in the order of a few tens of milliseconds, which can be considered ideal for most application.

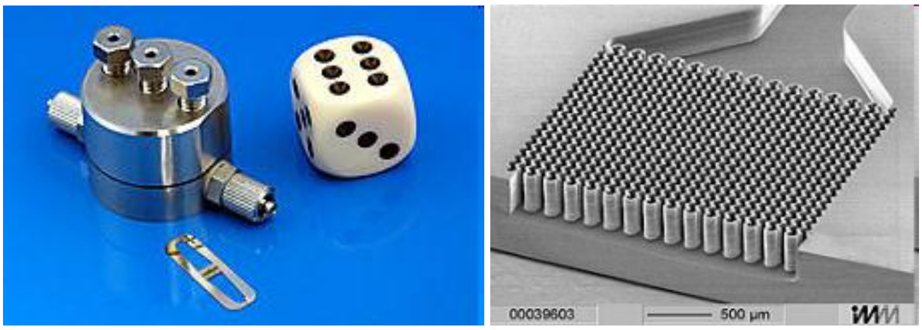

Figure 1.13. Slit interdigited commercial micromixer by IMM, Institut für Mikrotechnik Mainz GmbH. On the left is the assembled device, on the right is a closeup of the mixing element, where the two streams are laminated and brought into contact with an increased area of contact.

Increased Safety

Heat exchange capabilities are intimately linked to the safety of chemical reactors. Reaction with a strong exothermal character have a long history for being the cause of explosions when temperature controls fail. In such processes, temperature needs to be monitored closely, for its increase also causes an increase in the reaction rate, according to Arrhenius' law, and an even stronger increase in heat production possibly resulting in a thermal runaway. The improved heat exchange potential of MFDs helps in reducing the risk (the probability) of such an event. Moreover, the dangers (the magnitude) of explosions are reduced as well, since the amount of material being processed in a microreactor is constant over time and very small compared to that of a traditional reactor (either batch or working in continuous flow, like a PFR or CSTR).

Nitrations are possibly the archetypical example of a reaction with strong thermal runaway risk, even on the laboratory scale, and the work by Ducry and Roberge on the autocatalytic nitration of phenol published in 2005 strongly highlights the issues of safety, besides the chemical performance of their experimental apparatus.[23] A more general paper on the scale-up of nitration processes using nitric acid has been published recently by a team of scientists from Novartis, giving further evidence of the industrial interest backing microfluidic technology.[24]

Even the fluorination of toluene with elemental fluorine could be carried out safely in microfluidic conditions thanks to the optimal heat exchange. This reaction is traditionally carried out at -70 °C on the lab scale. In this case, a new mechanism of the reaction was made accessible, going from a radical chain type (which is unselective and difficult to control) to an electrophilic substitution (safer and selective), even working at 10 °C.[25, 26]

Diazomethane offers yet another example towards different aspects of safety issues that can be tackled by employing microfluidic reactors. The molecule itself is very toxic and reactive, it may release nitrogen gas if heated and should not be stored in large amounts. Moreover, all of its precursors are toxic and/or explosive. Rossi et al. recently developed a convenient flow synthesis that uses N-methyl-N-nitrosourea as a starting material instead of N-methyl-N-nitroso-p-toluenesulfonamide which is also explosive. While slightly more expensive than the latter, the former reagent can be handled and stored more safely, than used to produce even large amounts of diazomethane *in situ*, so that it is consumed by the following reaction step and its space time concentration is kept constant and low in the system.[12]

Lastly, since microreactors only have a very small holdup of hazardous substance , the need for high levels of isolation of the operator from the reactor itself is greatly reduced, together with the costs for the plant management.

Ease of scale up

The scale up of chemical processes is traditionally an expensive effort in terms of both time and money. Operative parameters needs to be optimized every time the output volume is increased, and new problems may arise at every scale increase, requiring new technical solutions. Moreover, many intermediate steps are usually needed, to go from the lab- to the plant- scale, passing through different pilot plants capable of limited production runs.

There are two different approaches to the scaling up of chemical syntheses developed in microfluidic conditions: i) a proper scale up, to a *meso*-fluidic scale, which usually only requires minor tweaking or ii) numbering up of production units, basically running many syntheses in parallel. Both approaches are usually employed at the same time, going up in scale as long as the process is easy to optimize (also taking advantage from the reduced safety issues described earlier), then numbering up the production units. It is worth mentioning that having many identical reactors simultaneously at work helps reducing maintenance costs, since spare parts are common to all units, and stop times, since single units can be stopped for maintenance while the others keep going.

Comparing productivities

Comparing the productivities of different synthetic methods is often tricky to evaluate, so that even data reported in literature are sometimes misleading. Let’s consider a batch reactor processing a given amount of starting materials in a given amount of time. If the volume of the reactor was doubled, the amount of starting materials converted would double as well, with no increase in the reaction time. The same goes for a chemical flow reactor consisting in a tube of a given cross section. Doubling both the length of the reactor and the flow rate for the starting materials, would ensure the same reaction time and double the amount of starting materials processed in a given amount of time.

In order to compare continuous and discontinuous systems which may, in principle, sport different volumes, it is better to look at the *intensity* of the process, measured by the *space time yield* (STY), defined as

$$STY = \frac{n}{t \cdot V} \tag{1.23}$$

where n is the number of moles produced, t is the time needed to produce them and V is the volume of the reactor. STY has the dimensions of a quantity of matter over time over volume, in this thesis that is typically mol s^{-1} ml^{-1}.

Disadvantages and issues of MFDs

The foremost problem encountered when using MFD setups for chemical synthesis is probably that of the management of solids. The solubility of the reagents must be thoroughly checked and, in general, reactions must be designed so that little or no solid is produced. As a rule of thumb, no solid should be used whose size is more than one tenth that of the channel, in order not to risk the clogging of the reactor. Another issue derives from the high surface-to-volume area typical of MFD. As previously described, this is a very welcome characteristic for exchange phenomena, but it also means that there is an higher specific surface exposed to the chemical environment. In general a completely inert surface is desired to avoid any interferences with the processes taking place inside the microchannels.

From an industrial point of view, a continuous process does not only require a reactor, but also separation and purification techniques to work in continuous mode. Chromatography offers an example of a discontinuous separation method that cannot be run in a continuous fashion. Any fluidic synthesis that relies on a chromatographic step will probably find its bottleneck there. In this perspective, the criterion for the choice of a reaction pathway towards the desired product should favor – for example – distillations over chromatographic steps.

2. Fast prototyping techniques & protocols

The market of microfluidic devices is growing together with the scientific and industrial interest in this field. Many companies, including Corning Inc. (US), Vapourtec (UK) and Micronit Microfluidics (Holland), just to name a few, offer standalone microfluidic solutions for chemical synthesis and other applications. These may include reactors (either chips or tubings), pumping systems (HPLC- or syringe- pumps), heat exchangers and various sensors (temperature and pressure being the most common). Notwithstanding the availability of commercial MRs, examples of custom-made devices abound in the literature. Prototypes can be interesting from a chemical point of view in that they allow extreme flexibility in the design and enable the testing of the proof of principle of an application before moving on to more expensive setups.

This chapter reports original protocols that have been developed throughout this thesis for the fabrication of microfluidic chips. It illustrates different types of chips and discusses the choice of materials, the fabrication of the interfaces with the external world and that of the microfluidic channels. The implementation of electrodes in MFD is discussed as well. The last two paragraphs illustrate experimental works on the surface treatments of polymer microchannels in order to control their properties and develop new applications.

2.1 General MFD structure

The MF chip prototypes that will be presented throughout this thesis share a same fundamental structure, depicted in figure 2.1, with two main elements, called the "head" and the "body". The former provides a convenient interface with the external environment by means of flanged PTFE tubings while the latter bears the channel network and any other functional element. The top cover, channel ceiling and floors are usually glass, and the whole structure resembles a multilayered sandwich.

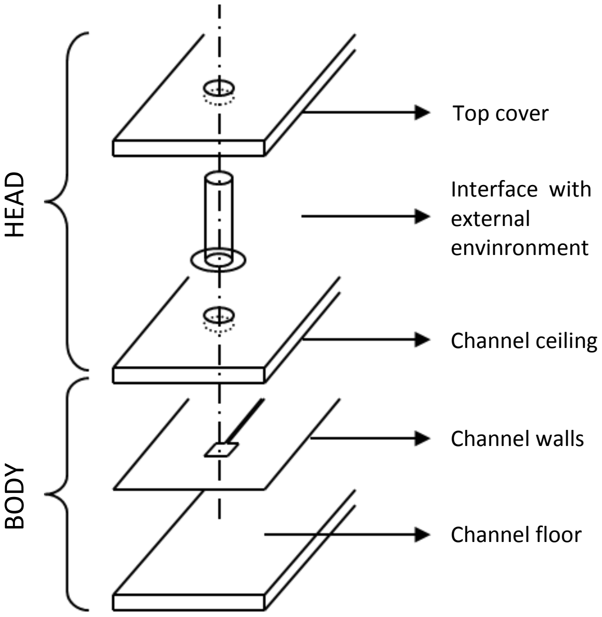

Figure 2.1. General structure of the MFD prototypes presented in this thesis

Different materials/techniques can in principle be used for the fabrication of the two main elements, as will be reported in the following sections. Depending on the employed method, it may be possible to fabricate a multilayered body, with fluids moving on all three directions, although they can only take “discrete” steps up and down.

2.2 Soft photolithography microfabrication

Microfabrication broadly refers to a collection of processes for the fabrication of physical objects with dimensions in the micrometer-to-millimiter scale. Many such processes are borrowed from well-established protocols, originally developed for semiconductor industries and used to make integrated circuits. A structure can be either fabricated on the surface of a substrate, hence being termed “additive”, or out of its bulk material, being called “subtractive”.

Soft photolithography[27] is an additive microfabrication technique, and its concept is borrowed directly from the printed circuit industry. The technique involves the patterning of a photoresist, a material whose chemical structure is changed upon exposition to some kind of radiation, i.e. by crosslinking and hardening. This change in chemical structure must be reflected by a change in the material’s properties, so that the areas exposed may either be removed (negative photoresist) or resist removal (positive photoresist) during the development step, usually carried by exposing the sample to a proper solvent. In general, the four steps reported in figure 2.2 can be recognized as common to all photolithographic techniques:

1. Photoresist deposition. The sensitive layer is deposited on the substrate. Photoresists are usually employed as liquids, so a solvent removal step may be necessary here. Different deposition methods are available, such as dip-coating, spin-coating and phase-vapour depositions, just to name a few.
2. Masking: the mask bearing the pattern to be copied is placed over the photoresist layer. Its position may be controlled by a mask aligner and it may or may not be placed in direct contact with the photoresist layer (this is evidently not possible in case of a liquid photoresist).
3. Exposition: the masked photoresist is irradiated with a preset amount of radiation. Exposure time and the intensity of the source play important roles in the correct transposition of the features of the mask on the photoresist.
4. Development: a suitable chemical agent, is used to remove either the irradiated or the un-irradiated portions of the photoresist layer.

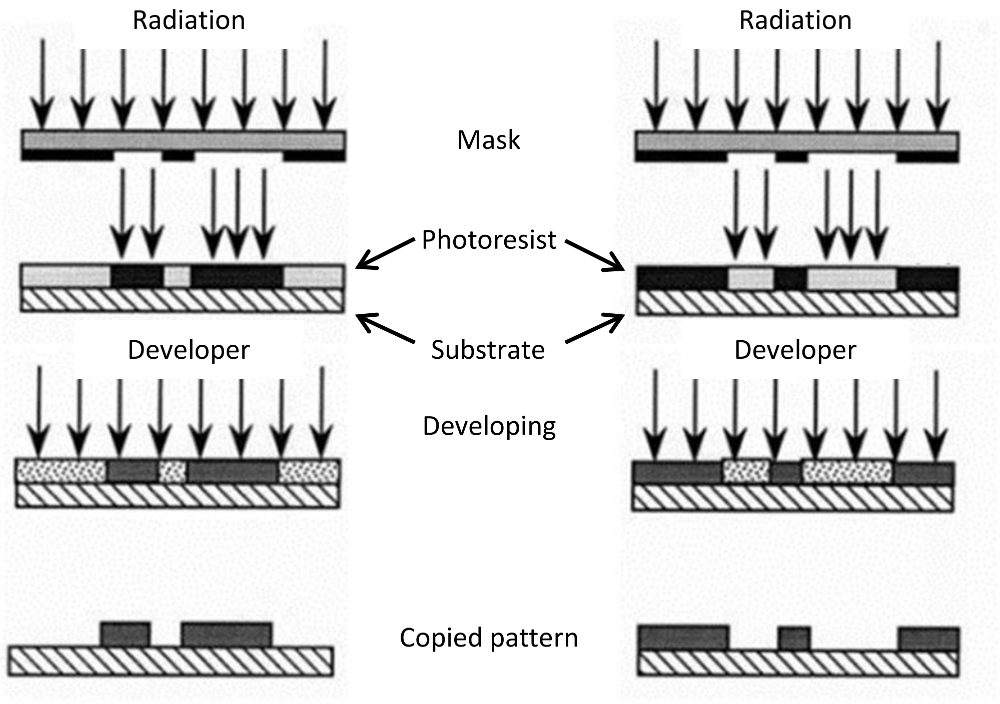

Figure 2.2. General process for soft photolithography. In the left example a negative photoresist is used, whereas a positive one is used on the right.

The resolution that can be achieved with this technique depends on the photoresist that is being used, on the illumination systems (wavelength used, geometry) and on the overall quality of the mask used. In the course of this thesis, two illumination systems were used:

1. A 350 W handheld Spectroline SB-100P lamp with an emission centered at λ = 365 nm and a low pass filter to remove visible components of the emission, mounted face down in a custom-made black box. The box (pictured in figure 2.3) provides cooling by two 12 V cooling fans of the type used for motherboard cooling on standard home computers, a manually operated shutter and a working plane that can be set at different heights.
2. A 350 W Reinraumtechnik Lanz collimated UV source (UV400), also with an emission centered at λ = 365 nm, located in a ISO 7 cleanroom environment. On this apparatus, the quartz optics ensure that light rays flow parallel, thus ensuring vertical shadows and minimal distortion of the mask's features upon their transfer to the photoresist. The working plane on this setup is fixed with a constant energy flow of 60 W/cm^2 and equipped with an automatic shutter for precise control of exposure times. This setup is displayed in picture 2.3.

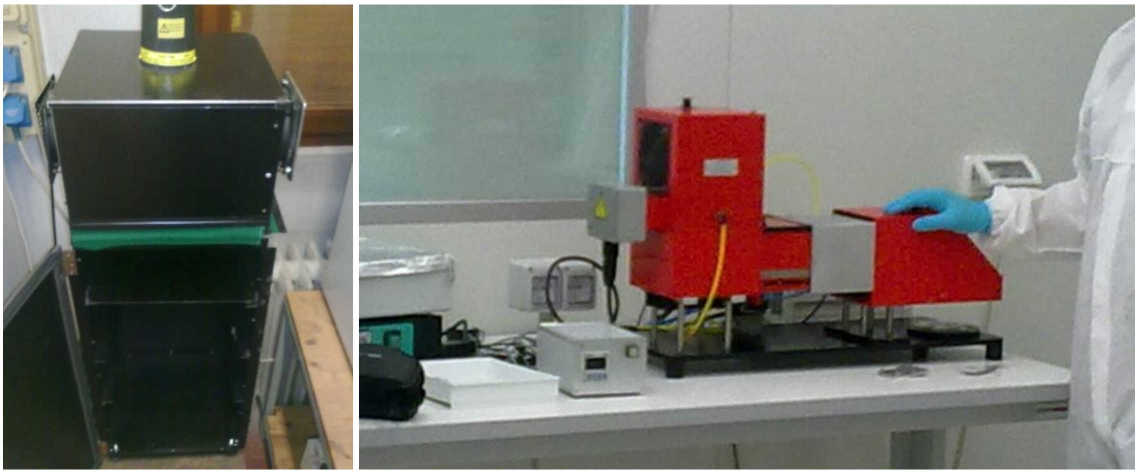

Figure 2.3. UV sources used for the soft photolithography fabrication of MFDs. On the left is the Spectroline lamp on its custom made housing; on the right is the Reinraumtechnik Lanz setup with collimator optics.

2.3 Materials

Silicon, glass, polymers, waxes and adhesives are all materials that can be used in the fabrication of MFDs. Choosing the right one is a key step in the prototyping process, since different materials can be worked with different techniques and each one has its peculiar properties that range from mechanical and heat resistances to the chemical compatibility with the surrounding environment. In their 2010 paper, Wootton and deMello went as far as to term this material issue an “elephant in the room” for MFDs: something that inevitably has to be dealt with (and possibly exploited) but is often overlooked.[28]

Poly(dimethylsiloxane) (PDMS), $[SiO(CH_3)_2]_n$ is possibly the most widely employed elastomer in the fast prototyping of MF chips. Dow Corning sells the popular two components kit, Sylgard 184.[29] The first component, or base, contains dimethylvinyl-terminated polydimethylsiloxane oligomers and a platinum complex; the second component, or curing agent, contains primarily methylhydrosiloxane-dimethylsiloxane copolymers, together with a small amount of an inhibitor ensuring a finite working time on the order of two hours from the mixing of the components. Sylgard 184 also contains large fractions of tetramethylated or dimethylvinylated silica filler, that modulate its mechanical properties.

PDMS is usually employed for replica molding techniques.[30] The lateral resolution that can be reached upon patterning depends mainly on the quality of the master being replicated, and features with sub-micron dimensions can be routinely reproduced. Cured PDMS samples have hydrophobic surfaces and are inert, unless oxidized by means of oxygen plasma. One of the drawbacks of PDMS is its incompatibility with many organic solvents such as toluene, that inevitably swell the polymer causing the failure of the device. For this reason, PDMS chips are employed with aqueous media, typically used for biochemical applications. Moreover, care must be taken to flush the devices with excess cleaning solution before use, to remove platinum traces that may be left behind by the catalyser and which may contaminate the experimental environment.

SU-8 is an epoxy-based negative photoresist, whose monomer is displayed in figure 2.4. This resin was originally formulated by IBM in 1982[31] and the first application for thick film lithography was reported in 1995.[32] It is provided as a mixture of the multifunctional bisphenol monomer and a triarylium-sulfonium salt-based photoinitiator in γ-butyrolactone.[33] Each monomer unit has eight crosslinking epoxy group, so that a very dense three-dimensional network is formed upon curing.

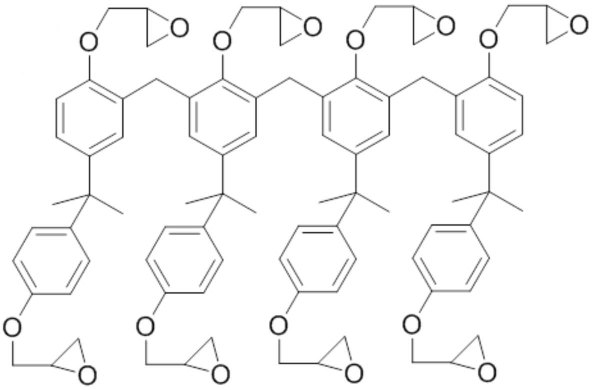

Figure 2.4. SU-8 monomer.

SU-8 is usually spin-coated on a suitable surface, where it undergoes baking to remove the solvent and then a photolithographic process with 365 nm wavelength UV radiation, to copy the desired pattern from a mask. Once developed, the resulting structures are extremely resistant to chemicals, so that the removal of crosslinked SU-8 is problematic even with hot piraña solutions and aqua regia.

Thanks to its chemical stability and mechanical properties, that make it possible to fabricate structures with very high aspect ratios, SU-8 is an ideal material for the fabrication of masters for replica molding and microcontact printing. Notwithstanding the interesting properties of this material, however, its use for the fabrication of closed microchannels is problematic, because the lithographic process can only produce open structures (see figure 2.2). A bonding process to another surface would therefore be needed in order to provide sealing for the device, but such process is quite difficult to carry out. In principle, SU-8 should be spin coated on a substrate, put in contact with the device to be sealed and then baked to evaporate the solvent. This, in turn create solvent bubbles between the structures and the sealing substrate that would damage the MFD.

Glasses are – or would be – the ideal choice for the fabrication of MFDs for chemical purposes. The most common glass, soda lime, is an amorphous solid comprising various amounts of silica (generally around 75% in weight) and other metal oxides, most notably sodium, calcium, aluminium and potassium. Most chemistry on the lab scale is carried out in glass vessels, so there is no worry about its chemical inertia in most situations. Furthermore, many types of glasses with a wide range of different properties exist on the market and surface modification techniques are available for their functionalization/compatibilization.

Glasses are usually worked by etching (or otherwise eroding) their surface. This is typically done by hydrofluoric acid or its derivates, either in solution or in the gas phase. Patterning a glass substrate with micron-sized structures is not considered a difficult task, but the sealing of the device requires extremely flat surfaces, with a rugosity lower than 5Å, in order for the silhanol groups of different glass slides to come in contact and condense. This, in turn, requires very expensive glass substrates and a low class cleanrooms to work in, making all-glass chips designs unsuitable for fast prototyping applications.

Thiol–ene photopolymers have been extensively used to fabricate microfluidic devices and to contribute to the performance, alter the surface chemistry, or control the material properties of various microdevices.[34] Thiol–ene materials are characterized by their exceptional solvent resistance, rapid curing and strong adhesion to metal and glass substrates. Thiol-ene based liquid monomers solutions are available from Norland Products Inc., who commercializes them as optical adhesives under the acronym NOA. There exist various formulations that differ in their mechanical properties, curing time, viscosity and refractive index. NOA 81, whose main components are reported in figure 2.5, is the formulation that has been used throughout this thesis because of its short curing time. This single component liquid photopolymerizes upon exposure to UV light without inhibition from oxygen and for large thicknesses (>1mm).[35] As compared to PDMS, NOA adhesives have a i) greater solvent resistance to swelling, ii) much higher elastic modulus (typically, 3 orders of magnitude), iii) smaller autofluoresence background and iv) are impermeable to air and water vapor.[36] The fully cured material is optically transparent in the visible range of the electromagnetic spectrum and adheres to glass and metals alike. It resists temperatures up to 130 °C. Table 2.1 shows the effects of some chemicals and mixtures of chemicals on cured samples of NOA 81.[35]

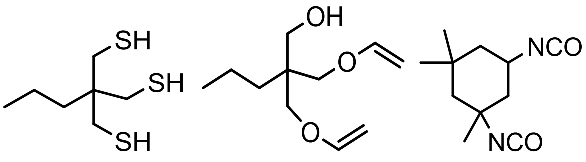

Figure 2.5. Components of NOA 81 resin.

The polymerization is almost exclusively vertical, so this is an ideal substrate for photolithographic techniques. The use of NOA 81 for prototyping purposes was first reported by Cygan et al. in 2005[37] in order to overcome the compatibility issues of PDMS with many organic solvents. The only drawback of NOA 81 is the delamination it undergoes when exposed to halogenated solvents and strong bases. While not as resistant as SU-8, NOA 81 strikes a good balance between ease of fabrication and chemical resistance, making an excellent choice for the fabrication of MFDs for chemical synthesis.

Substance	Direct exposition for 1 h	Indirect exposition for 24 h
Water	-	-
Sulfuric acid 10%	-	-
Acetic acid 5%	-	-
Phosphoric acid 5%	-	-
Sodium hydroxide 1%	Softening	-
Sodium phosphate 5%	Softening	-
Sodium carbonate 5%	Softening	-
Sodium borate 5%	Softening	-
Sodium hydroxide 10%	Dissolution	Dissolution
Hexane	-	-
Methanol	-	-
Toluene	-	-
Trichloroethylene	-	-
Dimethylformamide	Softening	-
Acetone	Softening	-
Dichloroethane	Softening	-
Dichloromethane	Dissolution	Dissolution

Table 2.1 Resistance of NOA 81 to various chemicals. Direct exposition refers to a film of resin in contact with the solvent; indirect exposition refers to the solvent flowing inside the polymeric MFD.

Adhesive tapes are generally cheap, commercially available materials that can be used for the fabrication of microfluidic channels by blade cutting. Interestingly enough, it was only in the last few years that reports on the use of adhesive tapes began to be published, such as the one from Yuen and Vasily[38]. While most of these tapes are incompatible with solvents other than water and alcohols, prototypes can be fabricated in matters of minutes and may prove very useful for biological applications.

Parafilm M is one of the most useful and common consumables found in chemical laboratories. Typically used for sealing applications, it consists mainly of polyolefins, long chain hydrocarbons lacking functional groups. Materials of this kind are commonly referred as waxes, malleable near ambient temperature and with a melting point near room temperature.

Like adhesives, Parafilm can be blade cut to obtain a pattern of channels, then soften by heating just below the melting point and sandwiched between two hard slides. Organic solvents in general dissolve this material, which on the other hand displays surprisingly good resistance to aqueous acids and bases, as reported in table 2.2, making it useful for water-based applications.

Effects of exposition for 48 hours at room temperature		
	Agent	**Effect**
Acids	Hydrochloric acid 36%	-
	Sulfuric acid 98%	-
	Nitric acid 95%	Browning (film resists)
Alcali	Sodium hydroxide 22%	-
	Ammonium hydroxide 28%	-
Salts	Sodium chloride 20%	-
	Potassium permanganate 5%	Browning (film resists)
	Iodine 0.1 mol/l	Browning (film resists)
Organic solvents	Methanol	-
	Ethanol	-
	Isopropanol	-
	Diethyl ether	Dissolution
	Chloroform	Dissolution
	Carbon tetrachloride	Dissolution
	Benzene	Dissolution
	Toluene	Dissolution

Table 2.2 Resistance of Parafilm M to various chemicals, as reported by a reseller.

Polytetrafluoroethylene (PTFE) is a synthetic fluorocarbon polymer that finds numerous applications thanks to its extremely low coefficients of friction against solids, its hydrophobicity and low chemical reactivity. It is typically commercialized as Teflon, by DuPont Co. PTFE can be machined to good tolerances in order to fabricate both interface systems (heads) and channel networks for devices. However, a workshop is required and its use in this thesis was limited to “advanced” prototypes.

2.4 Protocols for fast prototyping of MFDs

Fast prototyping represents an important alternative to commercially available devices, in that it provides a mean to test an application’s proof of principle, in a short time and with little cost. Moreover, while most manufacturers will produce microfluidic chips based on customers’ designs, chemists appreciate the complete control over the properties of the reactors that can be achieved when fabricating their own microfluidic solutions. Hereafter, a number of protocols are reported for the fabrication of microfluidic devices that were developed in the group of prof. Maggini, which started to explore flow chemistry on the micro scale in 2007.[39, 40]

Glass cleaning

Most of the devices that will be presented in this thesis have been fabricated on glass plates. Glass surfaces are bound to collect dust and organic materials during storage and handling, that can significantly modify their properties. In particular, the good adhesion of different materials on the glass may suffer from the presence of other substances. The surface chemistry may be altered, too, effectively impairing the effects of surface modification reactions that may be required for a specific application. It is therefore imperative that all glass substrates be thoroughly cleaned in order for an ideal behavior of this material to be preserved. Glass plates undergoing machining, such as drilling or sanding, should be cleaned after they have been worked on, paying special attention to the area where the machining took place (i.e. the walls of the hole, in case of drilling, where a lot of silica dusts are bound to collect). Plates undergoing chemical etching, by hydrofluoric acid or batch oxide etch solutions should be cleaned both before and after the treatment.

The following protocol consists of three steps: standard cleaning; piraña or ozone cleaning; final rinse and drying. Experience shows that step 2 may not always be necessary, if pre-cleaned glass is used. Corning microscope slides, plain (not frosted) have been successfully used throughout this thesis and performed well for most fast prototyping purposes without resorting to the cleaning procedures illustrated in step 2. However, in those cases where the size of the MFD being fabricated exceeded that of the microscope slides (either 3’’x1’’ or 3’’x2’’), glass plates from other sources were employed and skipping the second step often led to fails later in the process.

Glass slides should always be handled with gloves, using tweezers whenever possible to avoid contaminations. In between the steps, the slides should be kept in a closed container, wrapped in cleanroom paper, which is specifically designed to minimize particulate generation.

1. **Standard cleaning**
   a. Wash the glass slide with standard laboratory glassware detergent, by using a clean sponge. Thin substrates (i.e. 100 µm-thick glass slides) should be immersed in the detergent solution and sonicated for 15 minutes, in order not to damage them.
   b. Rinse with water to remove foam.
   c. Rinse with abundant DI water.

   Repeat step 1 at least twice, or more should buildups of dirt still appear on the substrate upon naked-eye inspection.

2. **Hot piraña cleaning**

   WARNING: Piraña solutions must be prepared and handled with great care, under a fume hood and possibly kept behind a screen. They are highly corrosive and oxidating. Piraña solutions clean by dissolving organic buildups, and a large amount of contaminants is bound to cause violent bubbling and a release of gas that can cause an explosion. For this reason, make sure surfaces are free of organic solvents from previous wash steps.
   a. In a beaker with a magnetic stirrer, prepare a 4:1 mixture of concentrated sulfuric acid (oleum) and 30% hydrogen peroxide solution *by slowly adding the hydrogen peroxide to the acid under stirring*.
   b. Heat the mixture to 70 °C.
   c. Immerse the glass substrate in the solution using Teflon tweezers and leave it there for 30 minutes.
   d. Remove the sample from the cleaning solution using Teflon tweezers, moving it to a beaked filled with DI water.
   e. Thoroughly rinse with DI water.

   Ozone cleaning

   WARNING: ozone is a toxic gas with a clearly distinguishable, sharp odor somewhat resembling chlorine bleach. Most people can detect about 0.01 ppm of ozone in air. Exposure of 0.1 to 1 ppm produces headaches, burning eyes, and irritation of the airways. For this reason, this step should always be carried out under a fume hood.

   a. Turn on the ozone cleaner (pictured in figure 2.6) and allow 20 minutes for the UV lamp to heat up and ozone to build up in the chamber.
   b. Put the glass plate in the chamber for 15 minutes, then turn it face down and let it sit for another 15 minutes.
   c. After turning off the lamp and removing the sample, allow the ozone to flow out of the chamber, then inspect it and clean any residue that may have collected there.

Figure 2.6. Ozone cleaner.

3. **Final drying**
   a. Rinse with isopropanol.
   b. Dry under nitrogen flow.

   Note 1: Compressed air may be used only if it does not carry oil microparticles, which is often the case when a compressor is used for the compressed air line.

   Note 2: Use of technical acetone instead of isopropanol for this task often results in lime stains on the glass due to the water contained in that solvent. Isopropanol also has a degreasing effect to remove traces of organics, so it's preferable over acetone.

Head fabrication with NOA 81 resin

As outlined in paragraph 2.1, the term "head" indicates the first part of the MFD encountered by the fluid, that is, the one providing the interface with the external world. The ideal technical solution for interfacing chemical fluidic devices with each other is perhaps the use of HPLC fittings made in polyether ether ketone (PEEK, an organic polymer thermoplastic) or stainless steel, which are designed to withstand high pressures and are compatible with a wide range of chemicals. Such fittings comprise a nut and a ferrule and have standardized dimensions and threads (as per ISO 262 standard) so a device fabricated with them can be easily setup with standard pumping systems. In order to use HPLC fittings, such as the one pictured in figure 2.7, a female threaded receiver is necessary but it is not possible to machine glass blocks in this way.

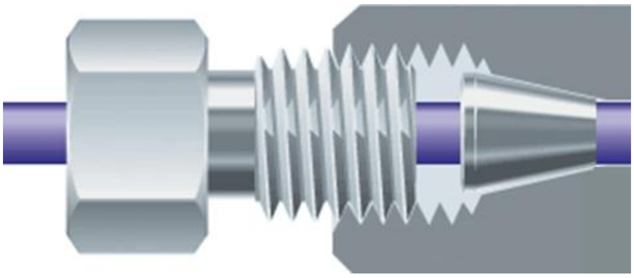

Figure 2.7. generic HPLC-type fitting for the interconnection of fluidic apparatuses. The blue tube passes through the bolt and tightly through the ferrule. Once screwed in, the bolt presses the ferrule in its seating so that the system is sealed and the fluid cannot exit backwards from the thread.

For this reason a new kind of interface had to be developed, that made use of the same tubing commonly used for HPLC connections, without threads. The heads presented in this paragraph is composed of two glass slides, drilled to provide inlets and outlets. Those two slides are glued together with NOA 81 resin, with flanged PTFE tubes in between, as schematically pictured in figure 2.8. The tubes have outer/inner diameters of 2.1 / 1.5 mm. Smaller tubes, (1.6 / 0.5 mm) can be quickly fitted thanks to PTFE being soft enough to slightly expand, providing an excellent sealing for the device. All PTFE tubes were acquired from Deutsch & Neumann GmbH Berlin. This head design is very different from the traditional one, where needles were pushed directly into the device causing considerable mechanical stress to the device and acting as wedges between the glass plates. A comparison is made in figure 2.9

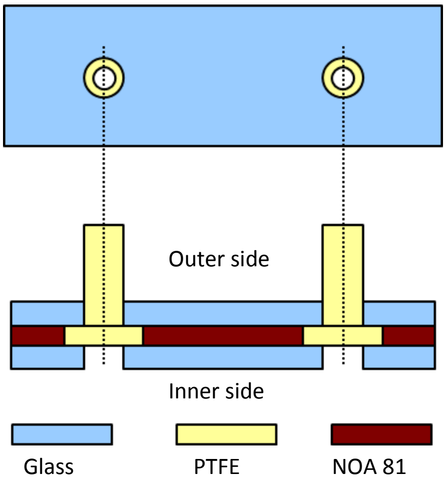

Figure 2.8. Schematic structure of the MFD head.

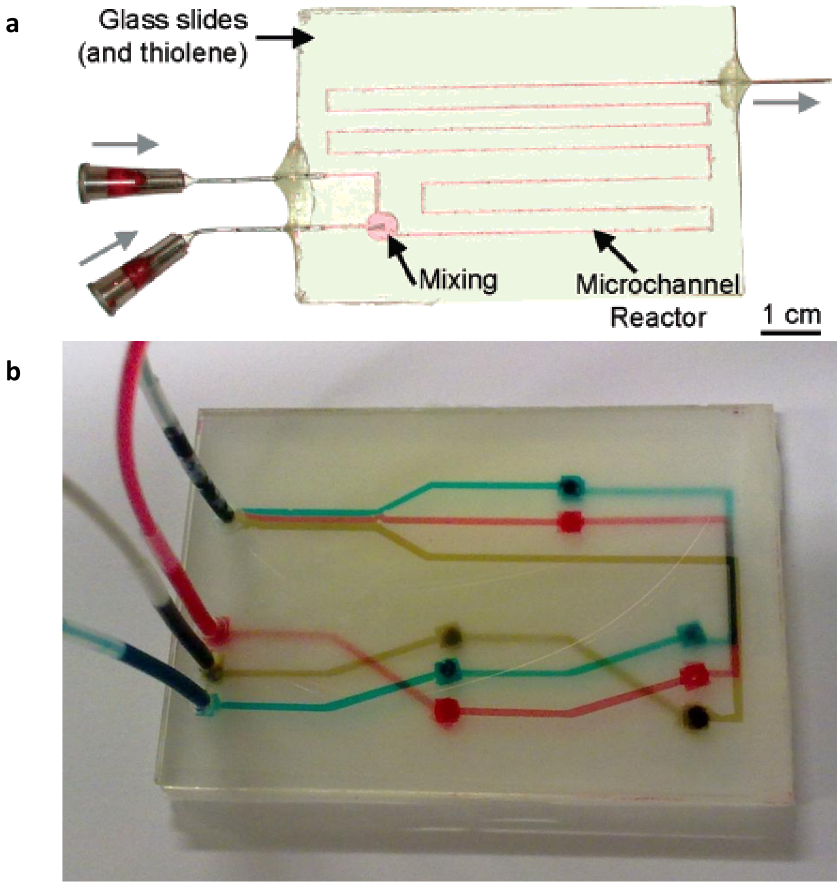

Figure 2.9. Comparison between a) traditional, needles-based interfacings of thiol-ene MFDs (developed by Wu et al.[41]) and b) our new MFD head.

1. **Glass drilling**
    a. Mark the desired positions of inlets on the glass slide with a felt-tip pen.
    b. Working at the lowest speed, scratch the surface of the glass on the mark, then flush with water and start tapping gently on the same spot, digging down to about half of the slide's thickness.
    c. Turn the slide around and complete the hole by scratching the surface and then digging slowly, as before.
    d. Repeat points b-c for all inlets.

Figure 2.10. Column-mounted dremel rotary tool. A hard rubber block (red) is used to hold the glass slide during drilling.

The drilling of glass slides is not an easy task and extensive trial and error is required in order to carry this task out with ease. Drilling is been carried out on a column-mounted Dremel rotary tool (figure 2.10) with a 11/64'' Dremel diamond wheel point (Dremel catalogue code 7105), pictured in figure 2.11. This point is designed for carving-engraving and final touching of hard materials, not for drilling; it can be successfully used to this end by tapping on the surface of the slide without applying too much pressure and cooling extensively with water. The tip of the diamond point should be checked regularly (every 20 drilled holes, or when glass slides show a tendency to break easily) to make sure the diamond powder has not been consumed.


Figure 2.11. Diamond wheel point used for drilling glass plates

Glass slides can be drilled straight through without turning them around as recommended in c). However, doing so inevitably results in holes with damaged rims on the exit side of the diamond point. In this case it is advisable to set the damaged rims towards the inside of the head, so that the damaged area is filled with NOA resin to avoid leaks.

An alternative to drilling that has been tested with good results is sanding with pressurized silica powder, which can be carried out with specialized equipment, where available. In order to dig through the glass, a brass plate was drilled with the aforementioned Dremel tool mounting a point suitable to drill soft metals. The plate was then put in front of the glass plate and used as a mask, aiming the powder flux into the hole for a few seconds. Sanding is definitely easier than drilling and gives excellent results, but requires more expensive equipment. Moreover, with a sufficient amount of practice, Dremel-drilling can become as quick and performing.

2. **Glass cleaning**
   See the glass cleaning protocol.
   This is also a good time to turn on the UV lamp so that it warms up to be used later for the curing of the thiolene resin.
3. **PTFE tube flanging**
   a. Using the tube cutter, cut 25-30 mm sections of PTFE tube. Cut two for each inlet, one with 2.1 and one with 1.6 mm external diameter.
   b. Set the larger tube in the flanger, as shown in figure 2.12a. It should stick out from the edge for about 2 mm (figure 2.12b).
   c. Fit the point of the flanging tool in the tube (see figure 2.12c) and move it around applying pressure.

d. Remove the flanged tube from the flanger (figure 2.12d).
e. Repeat points b-d for all the tubes.

The flange should be as round as possible, and large enough to allow a good seal. It's dimensions depend on the length of the tube sticking out from the flanger edge, but very long flanges risk to be damaged by the flanging process.

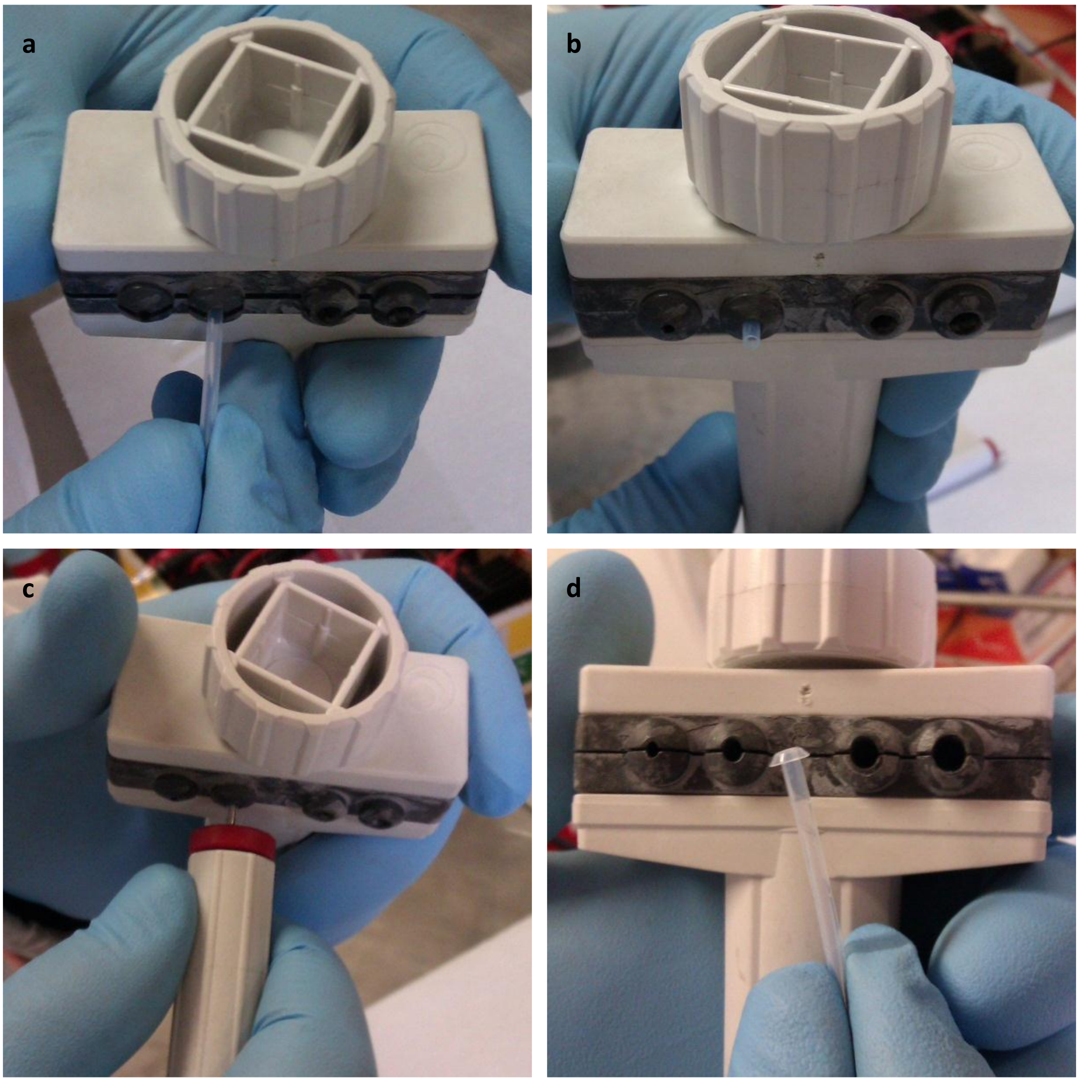

Figure 2.12. Procedure for the flanging of PTFE tubes. Special attention should be put to the amount of tube sticking out of the flanger in b).

4. **Tube fitting** (the various steps are picture in figure 2.13)
    a. Push a flanged tube through a glass plate hole by the end facing away from the flange, for about 5 mm (first tube in the figure).
    b. Pull the non-flanged end of the tube slowly and by turning it around, till the flange comes in contact with the glass plate (second tube) and opens up (third tube in the figure).
    c. Repeat a-b for each tube.

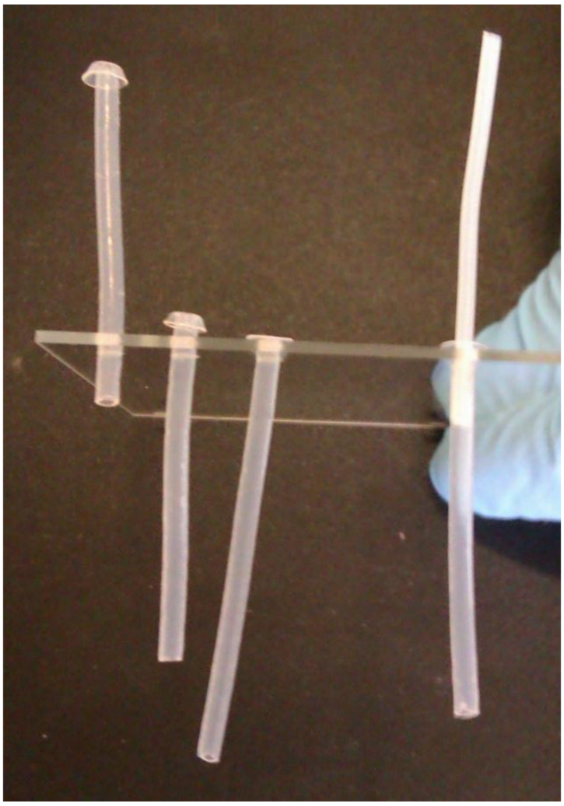

Figure 2.13. Stages of the fitting of flanged PTFE tubes on the drilled glass plate.

5. **Head sealing**
    a. Cut four small square slips of filter paper, about 3 mm in side. Soak one by one in a drop of NOA resin and then set them on the corners of the glass slide. No liquid resin layer should remain on top of the slips.
    b. Expose for 60 seconds to the UV lamp.
    c. Set the glass slide used in step 4 on a beaker with the flanges on top. The slide should be as well balanced as possible.
    d. Fit the smaller tubes cut in step 3 (1.6 mm external diameter) in the flanges, as pictured in figure 2.13 (last tube on the right). They will be used as guides for aligning the second glass slide.

e. Pour a layer of NOA resin on the slide, avoiding making bubbles. To this end, start pouring outside of the slide, into the beaker, then move on the slide and, again, finish outside. Make sure to pour the resin all around the flanges. (Figure 2.14a)

f. Set the second drilled glass slide over the first, using the small tubes as guides. Make one side touch the slide first, then slowly drop the other in order to avoid the formation of bubbles on the resin. (Figure 2.14b-c)

g. Allow to sit for one minute, letting the liquid pour from the sides. Help resin drops fall from the bottom by guiding them with a spatula.

h. Expose for 120 seconds on the top shelf of the UV lamp. (Figure 2.14d)

i. Remove the smaller PTFE tubes from the head.

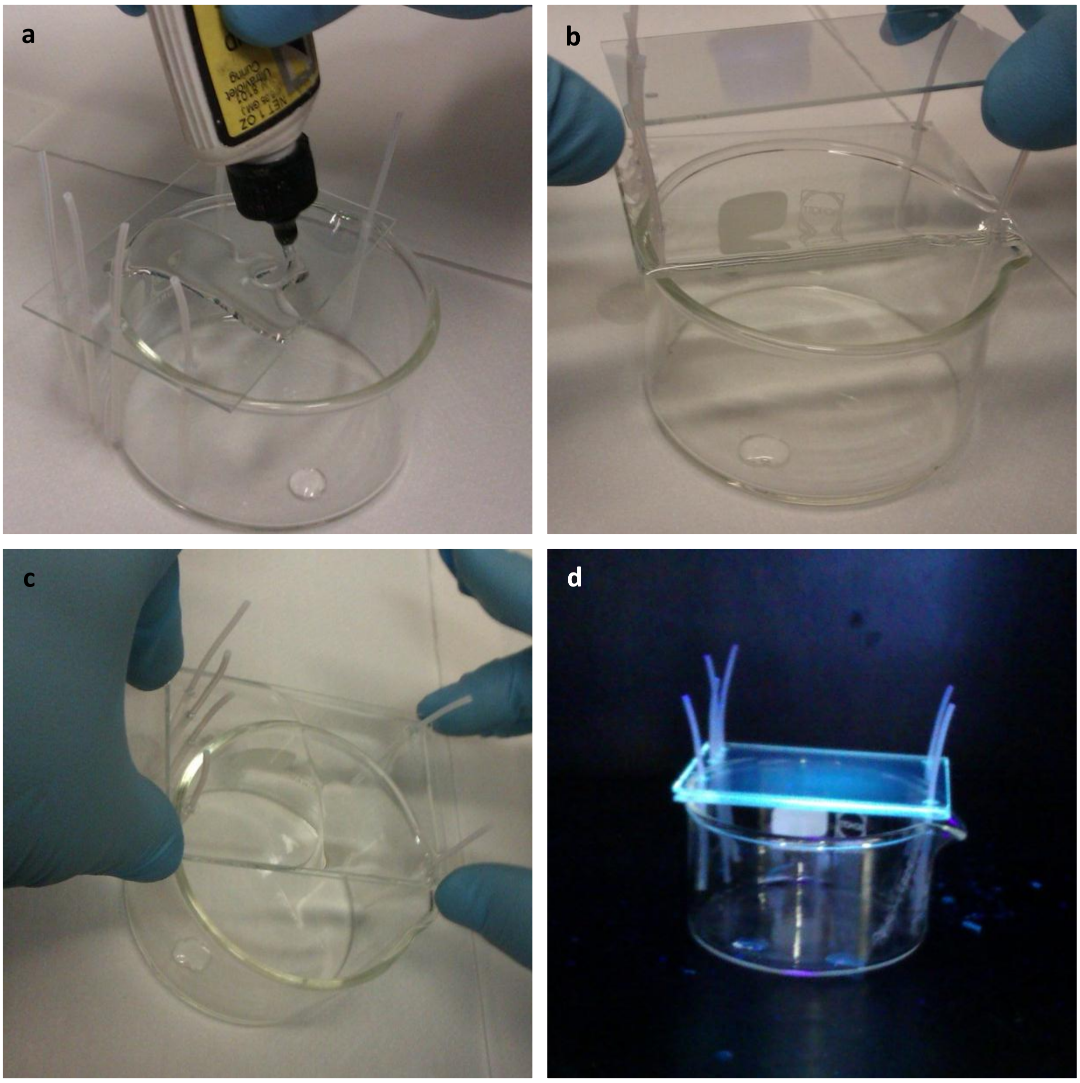

Figure 2.14. Sealing of NOA head. a) Liquid resin is poured over the outer glass plate and can't drip through the flanged tubes, since they were sealed. In b) the inner glass plate is aligned to the first thanks to the slim tubes and in c) it is brought into contact with the liquid resin starting from one side. Lastly, the head is irradiated with UV light.

6. **Cleaning & Postcuring**
   - a. Remove excess resin from the head with a blade. Put special care in removing any buildup on the inner side (see scheme in figure 2.8 for reference) because that is the side where the channels will be fabricated / will adhere.
   - b. Clean the inner surface by standard cleaning (cleaning paragraph, step 1) and dry it (step 3). It is especially important not to use acetone at this stage, since it may quickly damage the partially-cured resin.
   - c. Irradiate the clean head under the UV lamp for 30 minutes.
   - d. Put the head on a heating plate at 50 °C overnight, with the inner side facing down.

After point c, the head should display a yellowish color, typical for the NOA resin when it has just been cured. This hue will fade in a week time, or after 12 hours at 50 °C, hence step d, which is not required right now if the head is to be used for further fabrications step with NOA resin.

Soft lithography on thiol-ene resin (channels patterning)

This photolithographic process, displayed schematically in figure 2.15, exploits the properties of NOA 81 resin, which polymerizes vertically upon irradiation in the UV spectrum, at 365 nm. When a mask is used to partially cover a layer of liquid resin during the exposure process, the shadowed portion of the sample does not polymerize and can be washed away, effectively copying the pattern of the mask. As reported earlier on, the maximum horizontal resolution achievable with this technique depends on two major factors: the quality of the mask and the optical characteristics of the exposition system (in particular the collimation degree of the UV light). Thanks to its quartz optics, Reinraumtechnik Lanz collimated source performed better than the handheld Spectraline lamp in terms of light collimation and energy flow homogeneity. With some technical solutions, however, the Spectraline lamp’s collimation could be improved, in particular by working at an increased distance from the source as reported in figure 2.16.

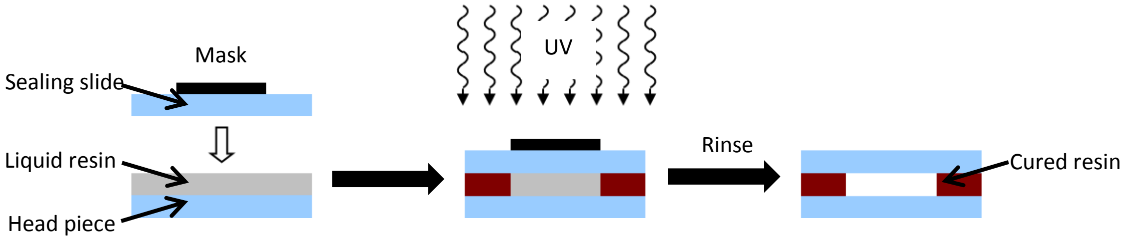

Figure 2.15. Schematic representation of the soft photolithographic process on NOA resin.

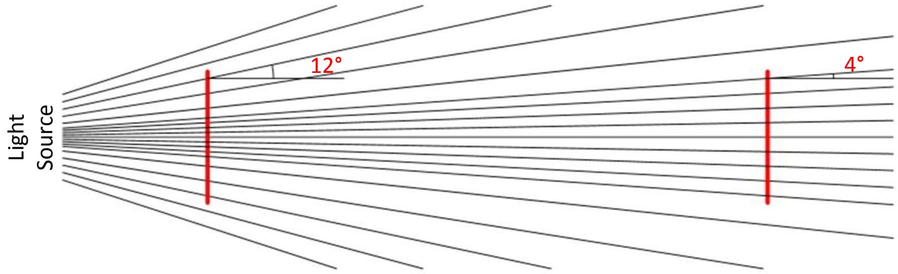

Figure 2.16. Effect of distance on the collimation of light rays. The divergence of the light rays insisting on a certain surface is lower, the further the surface is from the light source.

In the end, both light sources were used with this protocol, yielding excellent results. In particular, the exposure times indicated in the present protocols are intended for the Spectraline lamp, and may vary according to the age of the lamp itself and that of the resin.

The photolithographic masks that have been used were printed on transparencies with a common office laser printer working at 600 dpi resolution. By observing a printed image on the microscope (figure 2.17), it can be seen that it is made of small dots, so that even filled areas cannot stop light rays completely and the edges of the shapes are irregular and littered with dots. For this reason, a good reproducibility can be attained only for features whose size do not exceed five times the printer's resolution. This rule of thumb sets the lateral resolution of this method at circa 200 µm, which can be halved by employing a 1200 dpi printer.

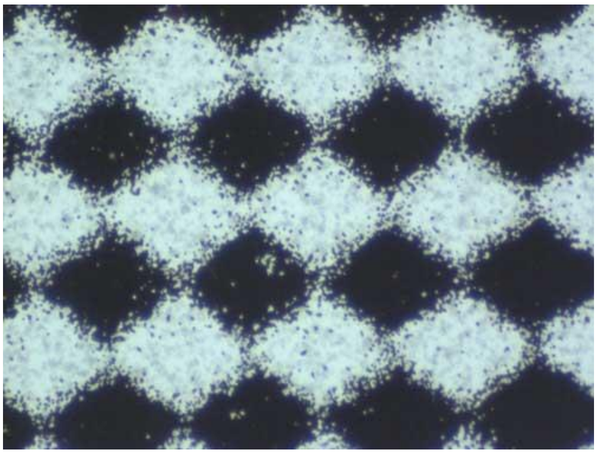

Figure 2.17. Closeup of an image printed on a laser printer.

The height of the channel is set by the thickness of the liquid resin layer that is irradiated through the mask. This, in turn, is controlled by using spacers (filter paper slids soaked in NOA resin, as per the fabrication of the head) to keep the head and the sealing slide separated. The thickness of one each such spacer is approximately 150 µm.

1. **Preparation of negative mask**
   1. Draw the channel pattern by using a computer software. The area of the channel should be filled. An example is reported in figure 2.18.
   2. Print two or three copies of the same design on transparency with a laser printer.
   3. Cut out and superimpose at least two masks, holding them together with tape. Pay special attention to the exact alignment of the masks.

   It is advisable to use circles with a diameter of 3 mm in correspondence to inlets, since the extra area helps an easy alignment with the drilled glass head. Besides that, keeping at least 3 mm away from the sides of the device when designing the mask helps in avoiding leaks.

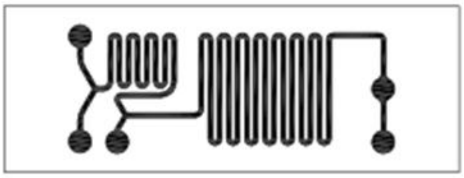

Figure 2.18. Sample photolithographic mask. Circles are used in correspondence to the inlets; channels are 600 µm wide.

2. **Photolithography**

   Note: the UV source should be warmed up for 15 minutes and the NOA resin should be taken out from the fridge and allowed to warm to room temperature, before this process.
   1. Fit a PTFE tube ($\varnothing_{ext}$ = 1.6 mm) in each inlet on the device head, so that it fills it completely without coming out on the inner side (see figure 2.19).
   2. Set the head of the device on a beaker or another suitable container, with the inner side faced up.
   3. Cut four small square slips of filter paper, about 3 mm in side. Soak one by one in a drop of NOA resin and then set them on the corners of the glass slide. No liquid resin layer should remain on top of the slips.
   4. Expose for 60 seconds on the top shelf.
   5. Repeat steps c) and d) if a thicker channel is required, superimposing the paper slips. Each set of spacers will provide a thickness of 150 µm on the average.

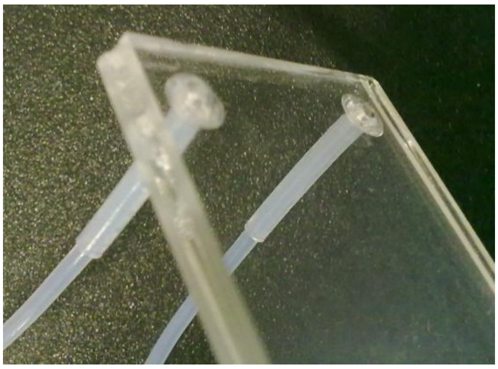

Figure 2.19. Head with stopped inlet tubes

  f. Pour a layer of NOA resin on the head, avoiding making bubbles. To this end, start pouring outside of the slide, into the beaker, then move on the slide and, again, finish outside.
  g. Set a glass slide over the head. Make one side touch the side of the head first, then slowly drop the other in order to avoid the formation of bubbles on the resin.
  h. Allow to sit for one minute, letting the liquid pour from the sides. Help resin drops fall from the bottom by guiding them with a spatula.
  i. Set the mask on the glass plate, so that the inlets from the head and the mask correspond. Another glass plate can be put on top of the mask to hold it in place while the uncured device is carried to the UV lamp.
  j. Expose for 60 seconds on the bottom shelf.
     If more than one set of spacers was used (see step c-d-e), increase the exposure time by 30 seconds per extra spacer.
  k. Remove the mask. It can be reused, unless it shows resin buildup.

3. **Channel emptying and flushing**
   a. Connect a water pump to a trap and a tube (figure 2.20a). Set the tip of a micropipette at the end of the tube, as shown in figure 2.20b.
   b. Remove the PTFE tubes blocking the inlets and use some paper to remove any uncured resin from the bottom of the device.
   c. Turn on the water pump. Fit the tip in one of the inlets, sucking uncured resin out slowly. It is preferable to apply vacuum on a single inlet throughout the process, if the channel design allows it, and block the other inlets one at a time in order to empty all possible courses.
   d. Once the channels are empty, apply the vacuum for at least 10 more minutes, to allow for the residues to be aspirated.
   e. Connect each outlet, other than the one where the vacuum is being applied, to a beaker filled with a solvent by means of a PTFE tube as in figure 2.20c. Flush extensively, alternating between neat ethanol and a 1 : 3 acetone : ethanol mixture. Small aliquots of the latter mixture should be flushed in between longer flushes of the former.

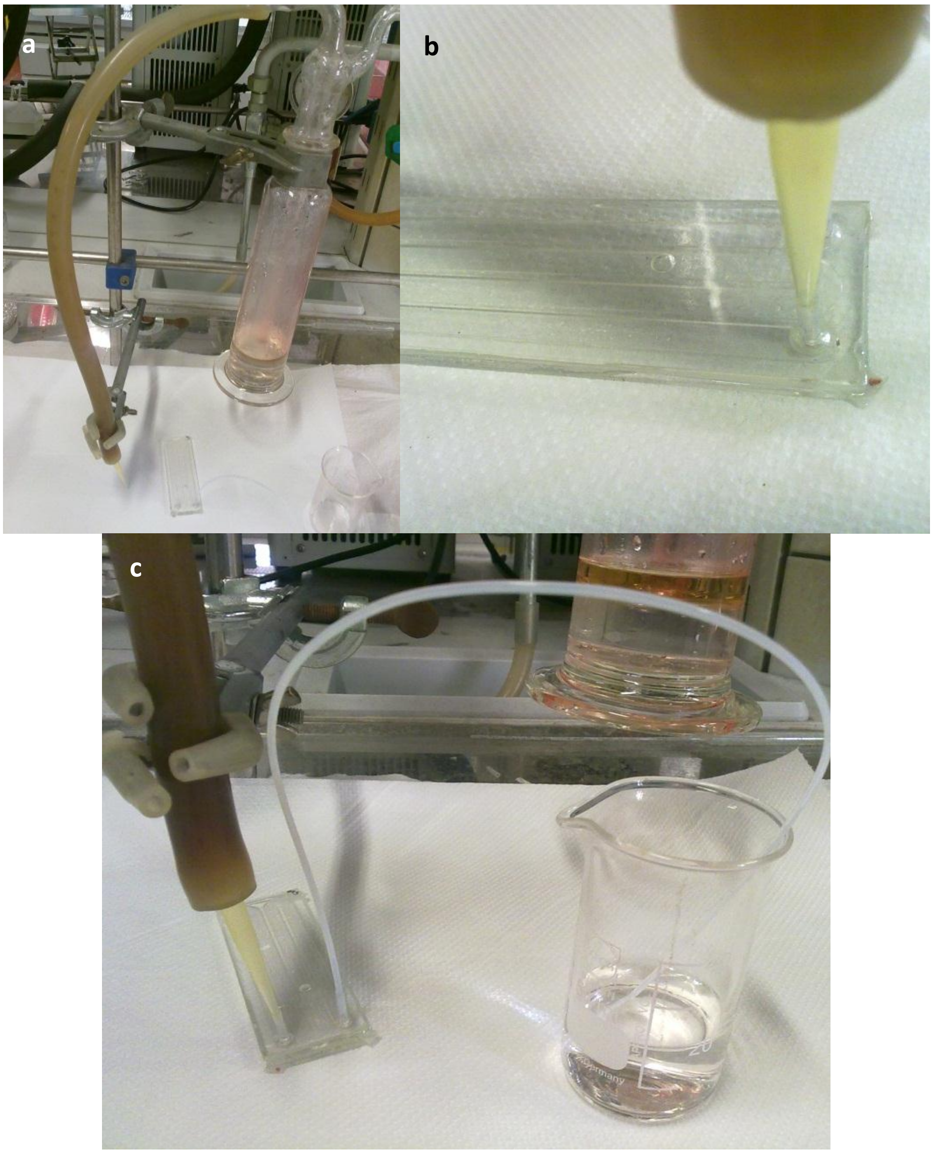

Figure 2.20. a), b) Setup used for removal of uncured resin from the patterned channels and c) washing of the device with ethanol

This procedure should be carried out with care, since it is where all mistakes made in the previous processes may manifest themselves as device failures. While it is not necessary to work in a dark environment, the uncured resin in the channels can still crosslink, so direct sunlight exposure should be avoided, along with exposition to any UV source.

Vacuum from the water pump should not be too strong, especially if small features were printed on the masks. Small structures, like pillars, or thin walls between channels may be damaged, resulting in shortcuts in the channel network. In case of device failure at this stage, it is usually possible to “open up” the device by means of a blade without damaging the head, which can be reused after being thoroughly cleaned.

While it has never been necessary during this thesis, warming up the device filled with uncured resin would lower the viscosity of the liquid filling the channels, thus making it possible to empty them more easily. This trick may come in handy for smaller channels, with high pressure drops. In this case, it is advisable to work at 40 °C maximum, not to promote extensive thermal crosslinking in the resin.

4. **Postcuring and priming**

   Note: before taking this step, ensure that the channels are clean (see step 3) and free from uncured resin leftovers. As with the procedure for the fabrication of the head, the device at this stage should appear yellow due to the incomplete crosslinking of the resin.

   a. Expose the device for 30 minutes on the top shelf.
   b. Put the device on a heating plate at about 50 °C overnight. Alternatively, let the device sit for a week time.
   c. Flush the device with toluene, then with water (2 hours for each solvent).

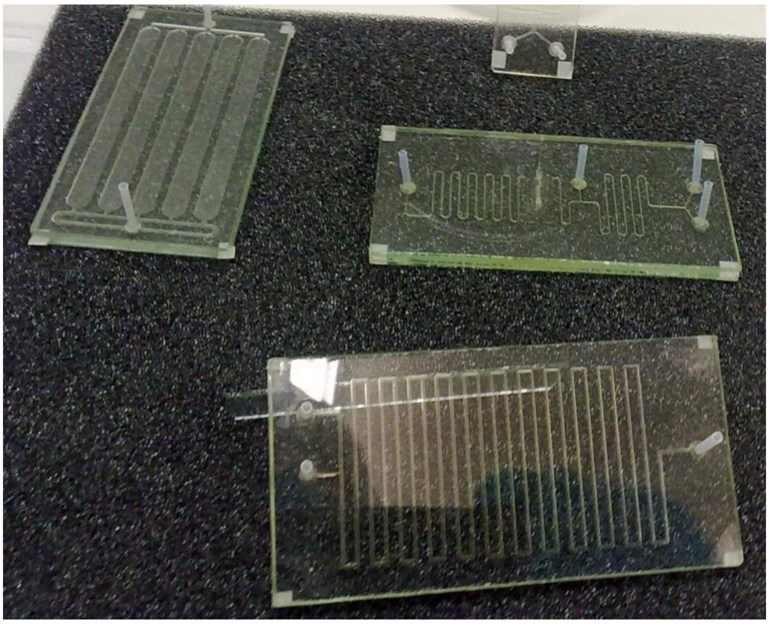

Figure 2.21. Finished, ready for use devices.

Embossing of biadhesive and Parafilm M films (channels patterning)

This technique represents an alternative to the photolithographic process for the fabrication of the channels that make up the body of MFDs. It is based on the use of a cutting plotter (a Graphtec Craft Robo 200-20, by Graphtec America Inc., was used throughout this thesis) on a sheet of the material the channels themselves are made from. In particular, biadhesive tape (PLP 250, from Syrom 90 SpA) and Parafilm M laboratory film have been used here with good results. The adhesion to the head of the MFD is assured by the glue on the biadhesive tape, while Parafilm can be either clamped between the head and a hard material, or warmed up and pressed to stick to them once softened. The method outlined here is indeed compatible with the head described earlier, made with NOA 81 resin, but also with different heads that may be machined from PTFE, poly(methylmethacrylate) or other materials.

The maximum lateral resolution in the production of the channels mostly depends on the capabilities of the plotter. Channels with a width of 300 µm have been fabricated with good reproducibility for straight paths, while round curves sometimes show a slight deformation, so that if such features are present the maximum resolution should be considered lower, at about 600 µm.

1. **Preparation of the channels**
    a. Draw the channel pattern by using a computer software. The area of the channel should not be filled. An example is reported in figure 2.22.
    b. Import the drawing in the proprietary software of the cutting plotter, which is compatible with the drawing exchange format (.dxf) standard.
    c. Fasten the desired film on the carrier sheet of the plotter. The film must not move during the cutting operation. Parafilm M can be fastened on the sheet directly, by using scotch tape. Biadhesive tape must be placed over an oily, non-stick surface that still provides some adhesion, in order for it not to slip away. That surface will therefore be attached to the carrier sheet.

    When using the cutting plotter, it is better to use squares (3 mm in side) instead of circles as in the case of optical lithography masks. It’s still better to keep at least 3 mm of material between the side of the device and the channel network to ensure proper sealing.

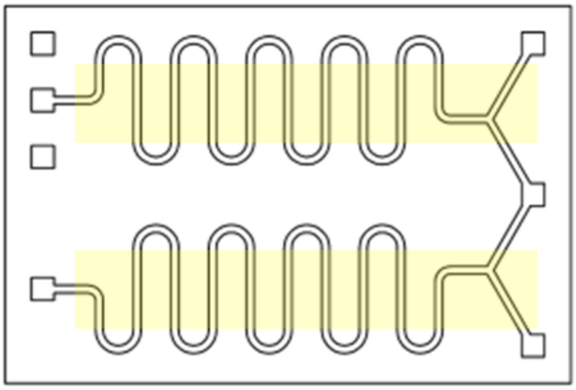

Figure 2.22. MFD design for embossing with cutting plotter. Notice the squares in correspondence of the inlets. A weak adhesive (yellow bands) can be used to keep the fringes from freely moving around while transferring the film.

2. **Sealing the chip (biadhesive)**
    a. Remove the tape from the oily slip, then place it on a surface with the sticky surface on top. Stick the head on the tape, aligning the holes to the squares in the channel design.
    b. Remove the back of the biadhesive, exposing the second sticky surface.
    c. Stick the last glass slide on this surface.

    Press on the whole surface with fingers, in order for the tape to stick on the glass slides and make seal. Areas with poor sealing can be easily detected by closely observing the device with backlight.

    Sealing the chip (Parafilm M)

    d. Remove the channel network from the carrier sheet and place it on the bottom glass plate. Once the network is in place, remove the adhesive keeping fringes in place, if any is present.
    If the design presents many fringes, such as in the case presented in figure 2.22, such fringes must not be allowed to move relative to one another. To this end, they can be held in place by a weak adhesive (the sticky band of post-it notes has proved to work very well) indicated in the above figure by a yellow band.
    e. Set the head on top of the channel network, aligning the inlets to the squares.
    f. Put the device on a hot plate between 45 and 50 °C. When the parafilm wax starts turning transparent, apply gentle pressure on the device, especially around the edges. Two minutes are enough for a good sealing.
    g. Alternatively, use paper clips to hold the chip together instead of sealing it, to provide a quick way for its disassembly. The clips should run all around the chip to assure proper sealing.

This approach to microfabrication can be easily adapted to produce multilayered devices, as shown in figure 2.23. To this end, the glass slide sealing each layer must bring the connection holes to the lower layer to allow the passage of the fluid. When working with Parafilm M, the addition of layers should always start from the head and proceed downwards so that successive thermal treatments do not alter the geometry of the upper structures by softening them over and over too many times.

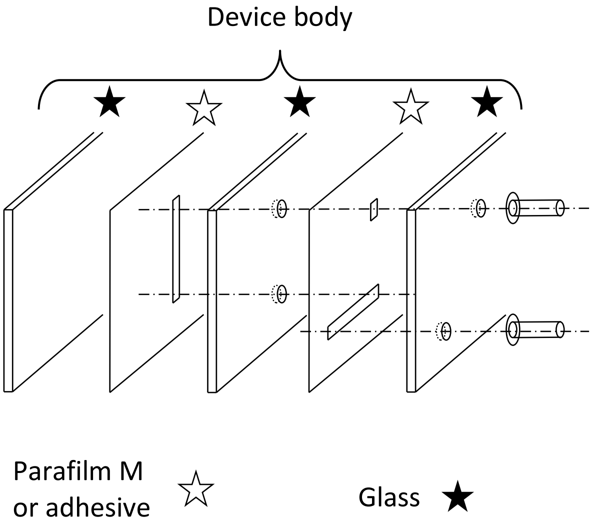

Figure 2.23. Structure of the body of a multilayer MFD.

2.5 Implementation of on-chip electronics

The addition of electrodes to the microfluidic chips whose fabrication has been presented so far, allows the development of many electrochemical applications, both for sensing and synthesis. Most microfluidic applications making use of electrodes were developed for use in the fields of biochemistry,[42] environmental monitoring[43] and even fuel cells,[44] exploiting features such as the rapidity, high sensitivity, reduced power consumption and reagent economy of microfluidic methods.[45] The behavior of the electrodes in such devices is affected both by the “micro” and the “fluidic” regimes, so that operative conditions are different from traditional “bulk”-“batch” systems. There are, however, many ways to account for these changes, so that operations can still be carried out reliably.[46] An in-depth description of electrochemical phenomena goes beyond the scope of this thesis, so the discussion will be limited to those aspects closely pertaining the applications selected for presentation. It is clear, however, that the implementation of electrochemical techniques broaden the range of possible applications of MFDs.

This paragraph describes the techniques that were successfully used to print (or pattern) different types of electrodes on glass surfaces. In doing so, it highlights an interesting application for the cutting plotter that is used for the preparation of both positive and negative masks on an adhesive vinyl sheet.

Silver electrodes

Silver films are mostly useful as references, making silver chloride electrodes with a standard electrode potential, E^0, against the standard hydrogen electrode of 0.230 V. The reaction of a diamine-silver complex $[Ag(NH_3)_2]^+$ (Tollens’ reagent) with an aldehyde, to yield a silver mirror is actually a classic assay for the presence of aldehydes in solution. Carrying the deposition out on a masked glass slide results in patterned silver films that can be used as electrodes.

The silver electrodes prepared by this method are resistant to liquid flows but easily damaged by scratching. They should be handled carefully during any further fabrication steps and should not be allowed to touch other surfaces, lest being damaged. Silver is quick to form strong chemical bonds with sulfur, so microchannels made in NOA resin cannot be fabricated over silver layers without modifying their surface. Upon observation by scanning electron microscopy, the silver film reveals an interesting nanostructure as shown in figure 2.24.

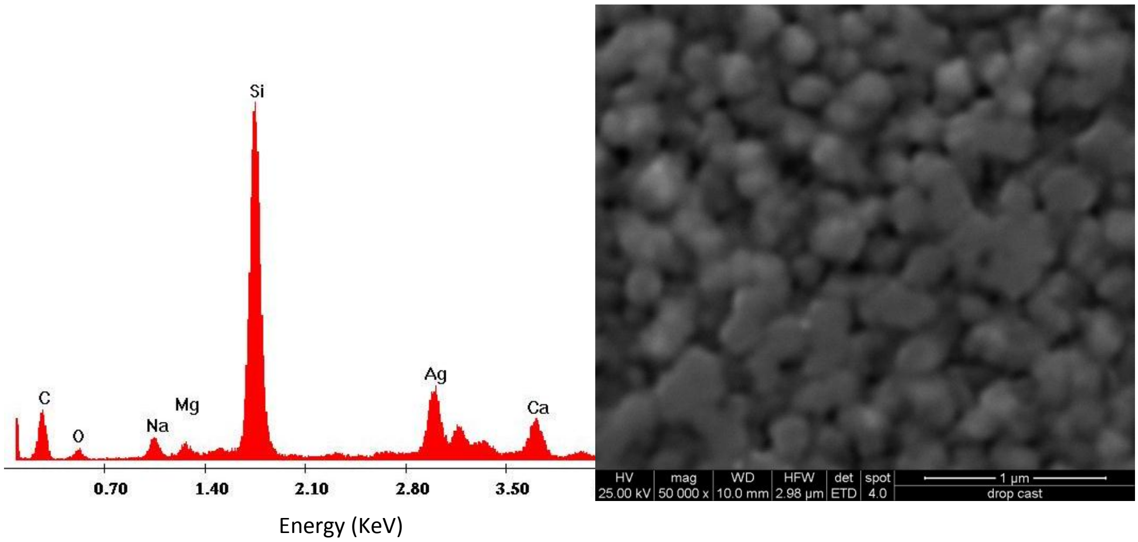

Figure 2.24. Energy dispersive X-ray spectrum and scanning electron micrograph of silver film deposited on glass.

1. **Preparation of Tollens reagent**
    a. To 10 ml of a 0.1 M aqueous silver nitrate solution (0.17 g $AgNO_3$ in 10 ml water) under stirring, add 5 ml of a 0.8 M potassium hydroxide solution (0.22 g KOH in 5 ml water), yielding a brown powder (silver oxide).
    b. While stirring vigorously, proceed to a drop by drop addition of 15 M aqueous ammonia solution untill the precipitate dissolves.

    Tollens' reagent has a short shelf life, it should be used within 24 hours from preparation and kept refrigerated in a dark glass container when not in use. Aging this compound may lead to the formation of silver nitride (Ag_3N), which is explosive. To avoid this, the solution should be disposed after being treated with diluted acid.

2. **Cleaning and masking of the glass slide**
    a. Follow the steps described in the glass cleaning protocol to prepare the glass substrate. A good cleaning is particularly important since it ensures a proper adhesion of the silver film to the glass.

   b. Follow the steps for the fabrication of microfluidic channels on bi-adhesive tape, to cut the vinyl sheet with the negative of the electrodes and apply the mask on the glass slide (figure 2.25a).

3. **Silver deposition**
   a. Prepare a 0.5 M glucose solution by dissolving 0.9 g glucose in 10 ml of water. Other aldehydes may work as well, but glucose gives a good reaction rate for the deposition.
   b. Put isolated drops of glucose on the masked slide.
   c. Add a few drops of Tollens’ reagent to the glucose.

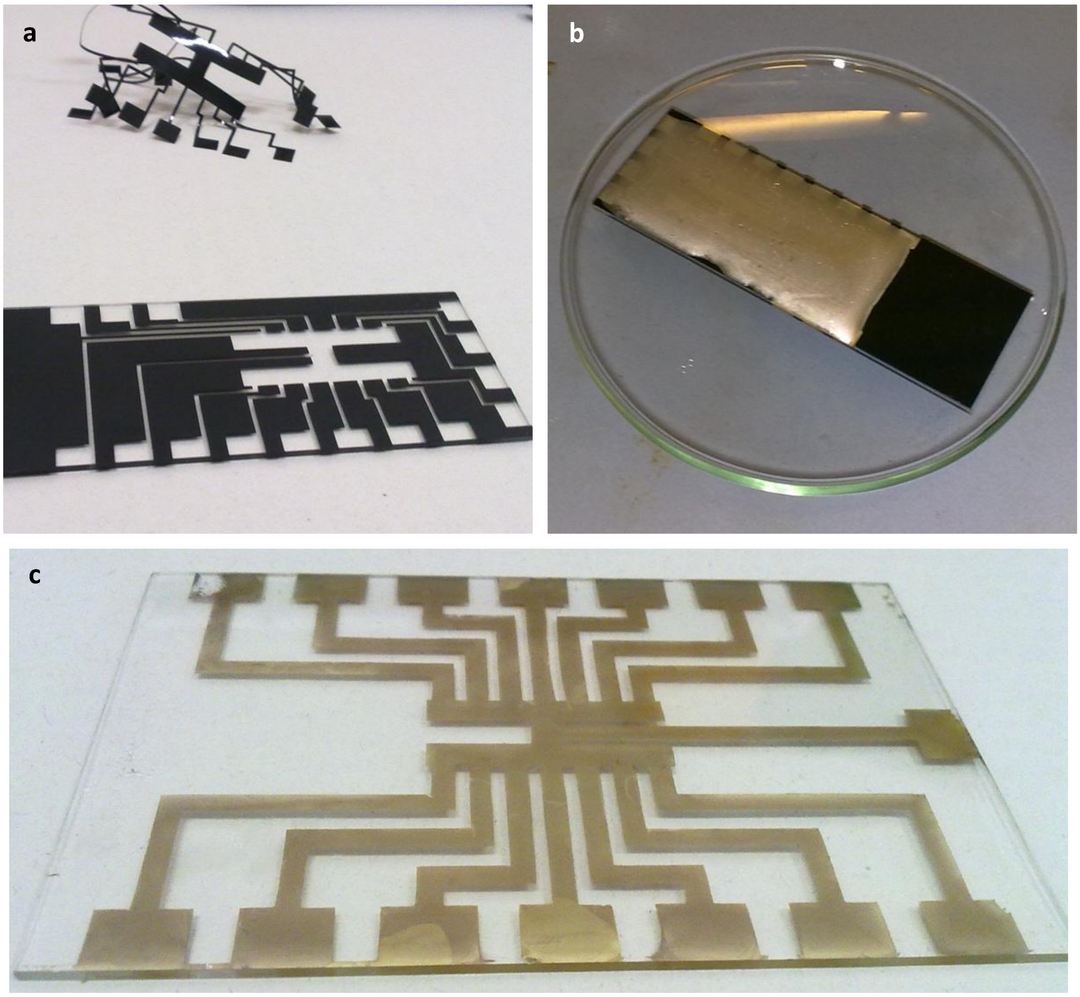

Figure 2.25. Silver deposition by the Tollens method. a) glass slide with negative mask; b) precipitation of the silver flim; c) Example of glass slide after cleaning and mask removal.

   d. Shake the slide for one minute, till a homogeneous coloration starts to develop.
      e. Let the slide sit for 15 minutes. The film of solution on the slide should develop a silver color (figure 2.25b).
   f. Wash the slide with abundant distilled water (the silver film should adhere enough to resist direct flushing even with tap water). The quality of the deposition can be

checked by turning the glass slide around and checking the silver mirror for defects.

g. Rinse with ethanol and dry under nitrogen.
h. Repeat steps b-g to grow a thicker silver film.
i. Remove the vinyl mask (figure 2.25c).

Indium-tin oxide electrodes

Indium-tin oxide (ITO) is a transparent, conducting, 9 : 1 mixture of In_2O_3 and SnO_2. This useful material, shown in figure 2.26, is usually deposited on glass as a thin film by electron beam evaporation, physical vapor deposition or sputter coating. The resistivity of the film depends on its thickness and on the impurities that may be present in the crystal lattice. ITO-coated glass slides are commercially available and such substrates were patterned by simple chemical etching.

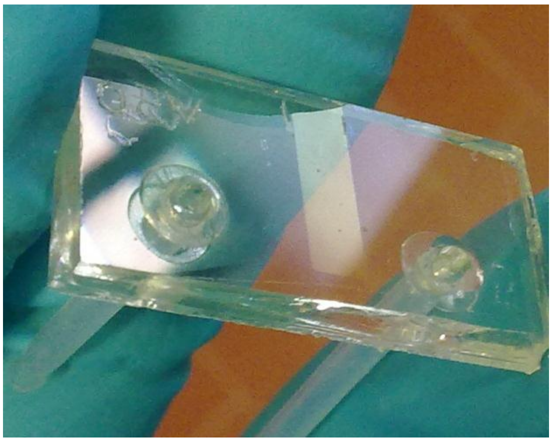

Figure 2.26. ITO electrode, recognizable by its slightly yellow hue, on a microfluidic head.

When used as an electrode, ITO cannot withstand negative potentials, which cause the reduction of In(III) and Sn(IV) to their metallic form. The protocol for the patterning of these electrodes uses masks, as in the case for the deposition of silver, although in this case the mask itself is positive and is used to protect the ITO surface from etching. The masked substrate is simply dip for 5 minutes in a hydrochloric acid solution (36%). After washing with deionized water, the surface is checked for the removal of unmasked ITO. Albeit transparent, this material can be recognized for a yellowish color, as shown in figure 2.26. Once all the oxide have been etched away, the mask can be removed by soaking the substrate in dichloromethane.

Platinum electrodes (over ITO)

Platinum electrodes were patterned by electroplating pre-patterned ITO electrodes. For this electrodeposition[47] a generator is employed and connected to the ITO electrode (negative pole) and a graphite rod counter electrode (positive pole) as in figure 2.27. Both electrodes are immersed in a 1 mM aqueous solution of hexachloroplatinic acid and a 5.00 V potential is established while stirring with a magnetic bar. After 15 minutes the ITO electrode displays a silvery mirror appearance because of the platinum on the surface.

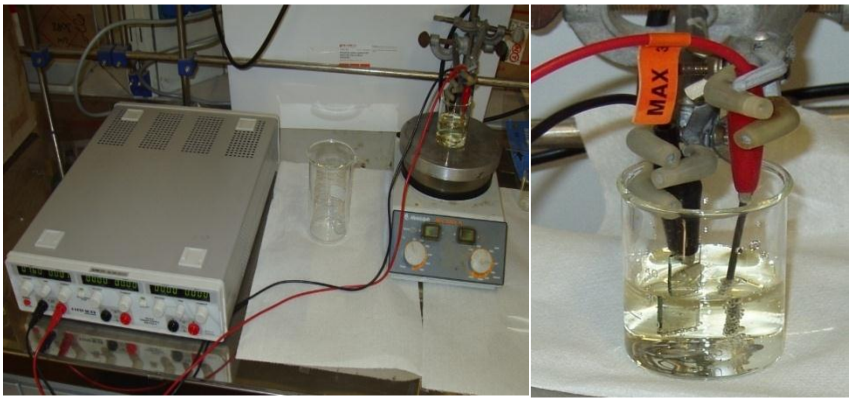

Figure 2.27. Setup for electroplating of ITO electrodes with platinum.

Gold electrodes

Gold electrodes are very useful working electrodes for they are noble metal electrodes and can withstand positive potentials without dissolving. There are different ways to fabricate gold structures on glass, in particular one may choose to etch a pre-formed surface (since gold-coated glass slides are commercially available) or deposit a gold layer by chemical or physical means. At any rate it should be noted that this metal does not adhere well to glass, so that a titanium or chromium layer is often deposited first, but it does not affect the behavior of the electrode.

Chemical etching of gold layers can be carried out in the same way that has been described for ITO, by masking the electrode with a vinyl sticker and exposing it to an acid solution. Anyway, since gold is a noble metal and hardly oxidized by hydrochloric acid, aqua regia (a 3:1 mixture of hydrochloric and nitric acids) has to be used. Short etching times, well under 1 minute, can be expected for this procedure and care must be taken not to expose the substrate for a longer time than necessary, since the gold under the mask may be etched away from the sides.

Another convenient possibility is a sputter-coating process carried out on a masked substrate. In this case, a negative vinyl mask is sticked on the bare glass, before setting the substrate in a sputter coating chamber operated under argon gas with a 18 mA current. The drawback of this technique is the limited thickness that can be achieved. Indeed, sputter coating is typically used in the preparation of insulating sample for electron microscopy, where only a thin layer is required in order to dissipate the charges brought about by the incoming electron beam. The electrodes pictured in figure 2.28 were sputter coated over a masked glass slide (also pictured in the back).

Figure 2.28. Gold electrodes sputter-coated on a glass slide. A masked slide is also pictured in the background.

Lastly, gold can be electroplated over ITO pre-patterned electrodes, as in the case of platinum. The electrodeposition bath in this case is prepared with tetrachloroauric acid.

2.6 Improving the solvent compatibility of NOA 81

As already mentioned, the high specific surface of MFDs can be both a welcome characteristic or a problem for an application. The compatibility of materials with the solvents must receive special attention for applications in synthetic chemistry, where aggressive chemical environment are often generated.[28] Since most fabrication techniques developed in this thesis make use of thiol-ene resin for the fabrication of the head, the body of the MFD, or both, a technique for the improvement of the compatibility of NOA 81 with aggressive solvents was assayed.

In Table 2.1 the effect of various solvents on this material were reported and it is noteworthy how dichloromethane (DCM), one of the most widely used solvents in organic chemistry, causes the delamination of NOA samples and ultimately the failure of NOA-fabricated devices. DMF and acetone only cause a softening of the material, but on the long run this will also affect the behavior of the devices. In order to render NOA MFDs impervious to the action of aggressive solvents, a coating method was developed to deposit a thin layer of silica (SiO_2) on the channel walls. Silicon dioxide presents many advantages, by being very similar to glass as a material, being hydrophilic like NOA (thus not dramatically changing the physical properties of the channels) and its chemistry being studied extensively.[48]

Many examples of silica coatings for different purposes can be found in literature, and it is worth noting that in the field of microfluidics a patent for the inertization of PDMS microchannels with sol-gel coatings has been filed by Hahn, Park and Shin in 2009,[49] while Orhan and coworkers published a technique to obtain borosilicate glass layers on PDMS relying on nonaqueous and alkali-free precursor solution, to overcome the limited adhesion of the silica film to the hydrophobic PDMS surface.[50]

SiO_2 layers can be grown in different ways, not all of which could find an application in the tests that were carried out. The oxidation to silica of an epitaxially deposited silicon surface, for example, would have been too time-consuming for a fast prototyping procedure and temperature issues prevented the employment of methods such as chemical vapour deposition to deposit the protective layer. The precipitation of silica films from aqueous alkoxide solutions (tetraethyl orthosilicate, TEOS, in particular) has been widely described in literature[48] and presents the needed flexibility to be employed in this case. Both the acid-catalysed sol-gel method and the ammonia-catalysed Stöber synthesis can indeed give raise to thin silica layers, but the latter can only do so under precise pH control[51]. This led to the choice of the sol gel method, for ease of preparation and known reproducibility of the deposition.

Results and discussion

Inertization tests were carried out on MFDs consisting of one inlet connected to an outlet by a serpentine. The channels were filled with a pre-aged sol gel precursor solution, before flushing with nitrogen gas. They were then allowed to sit for 2 hours, after which they were flushed with water. This process could be repeated more than once, but multiple iterations eventually lead to the clogging of the device. Early dip coating tests on the adhesion and morphology of sol-gel silica on thiol-ene resin samples, pointed out that the best formulation for the precursor alkoxide solution was a mixture with a 1:2:16:0.02 molar ratio of TEOS : deionized water : ethanol : hydrochloric acid. Different formulations resulted in severely cracked surfaces that tended to delaminate. The ATR-IR spectrum of one slab of as-prepared resin is compared with its silica-coated counterpart in figure 2.29. The presence of bands at 2841 cm^{-1} (stretching of C-H bonds in α to an oxygen atom), 1088 cm^{-1} (Si-O-Si stretching) and 819 cm^{-1} (Si-O bending) confirm the formation of a silica film on the surface.

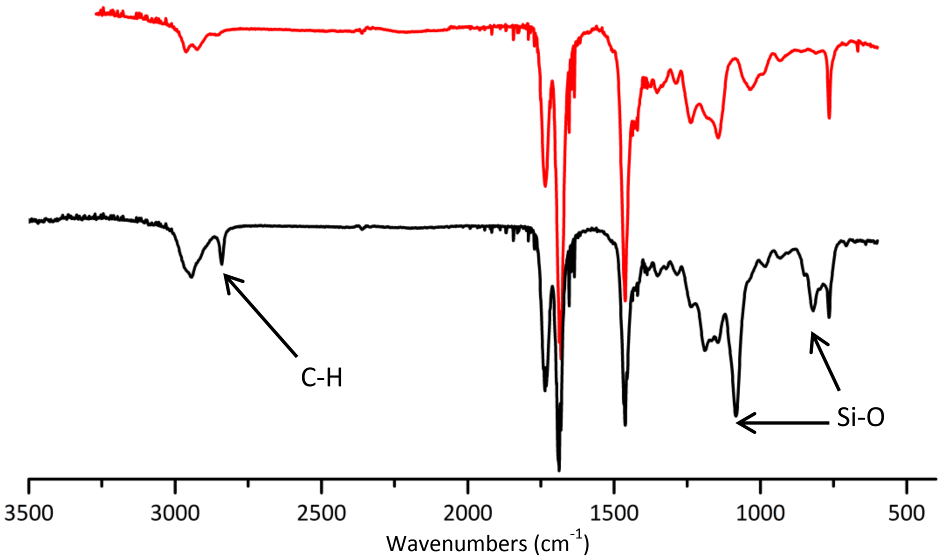

Figure 2.29. ATR-IR spectra of as prepared NOA 81 (red) and of the same sample after coating (black). The band at 2841 cm^{-1} is relative to the stretching of CH_2 bonds in α to oxygen atoms in -$Si(OEt)_3$ groups. The bands at 1088 and 819 cm^{-1} are also typical of Si-O-Si stretchings and Si-O bonds bending.

A first comparison was made between treated and untreated MFDs as to their resistance to a 3 hours acetone flush. After exposition to the solvent, each device was thoroughly rinsed with water and left sitting for 24 hours to settle. A blue tracer was then injected in the channel to check for the integrity of the channel walls. The outcome are pictured in figure 2.30. Upon loading with an aqueous ink, the untreated device was found to bear severe leakage while the treated one was still capable of holding the liquid. Further flushing of the treated channel with acetone resulted in failure of the device after short less than 5 hours.

The delamination of NOA can be observed by naked eye while operating the MFDs. Two further observations can be made about this process: firstly, channels do not start leaking until a secondary path has formed, either toward another channel, bypassing one part of the network, or toward the edge of the device. Before that, the solvent in the delaminating area is stagnant. Secondarily, once delamination starts from a given point on the edge of a channel, its rate does not change between treated and untreated devices. This is expectable, since sol-gel silica is known to be porous if not thermally treated to form a dense structure.[48] Therefore, it takes a certain time for the solvent to cross the porous silicon dioxide barrier but, once it reaches the resin, it starts delaminating it.

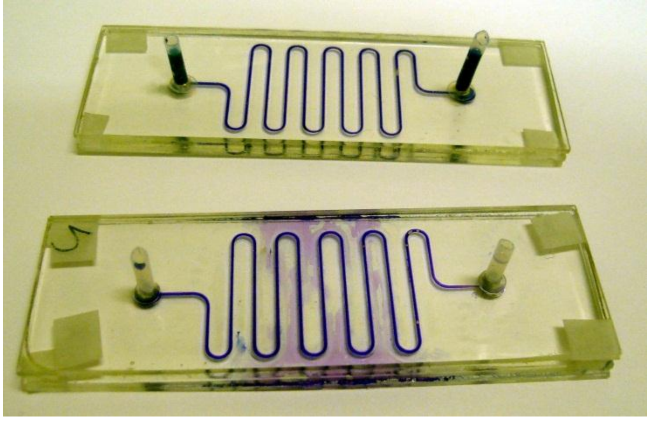

Figure 2.30. Comparison between inertized (top) and non inertized (bottom) MFDs, after flushing with acetone for 3 h.

Next, two similar devices were tested with DCM, the untreated one displaying severe leakage after 6 minutes only, with the delamination becoming visible almost immediately upon starting the solvent flow. Figure 2.31 shows the area in close proximity to the channel wall after the experiment. The channel treated with the sol gel precursor solution did only slightly better, failing after 75 minutes. By increasing the number of inertization cycles the resistance of the channels was increased, as reported in figure 2.32

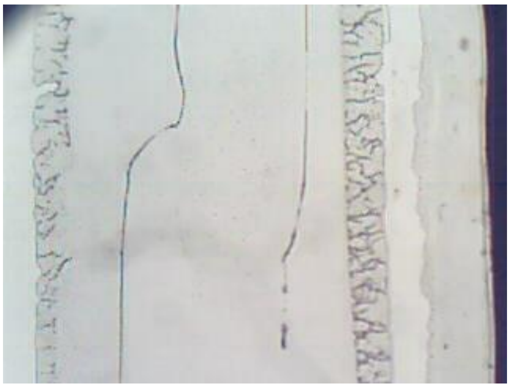

Figure 2.31. Delaminated area close to a channel (the wall is the black area visible on the righe) after DCM exposure.

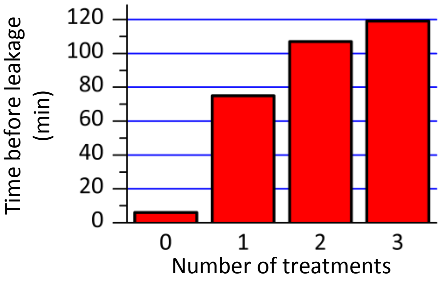

Figure 2.32. Working time of MFDs flushed with DCM as a function of the number of inertization treatments.

Finally, a different device design was tested in the mixing of two streams and generating either a continuous phase flow or a segmented flow. In both cases DCM was used as the solvent in the organic phase. Four identical devices were fabricated, which comprised two inlets, a Y-junction and one outlet. In the first mixing test, an indicator (bromocresole green) dissolved in DCM was mixed with an organic base through the Y junction so that its color changed from yellow to blue. In figure 2.33 a comparison is made between two Y-junctions that had been running for 20 minutes: in a) the device was protected with three inertization treatments whereas in b) the device was used as-fabricated.

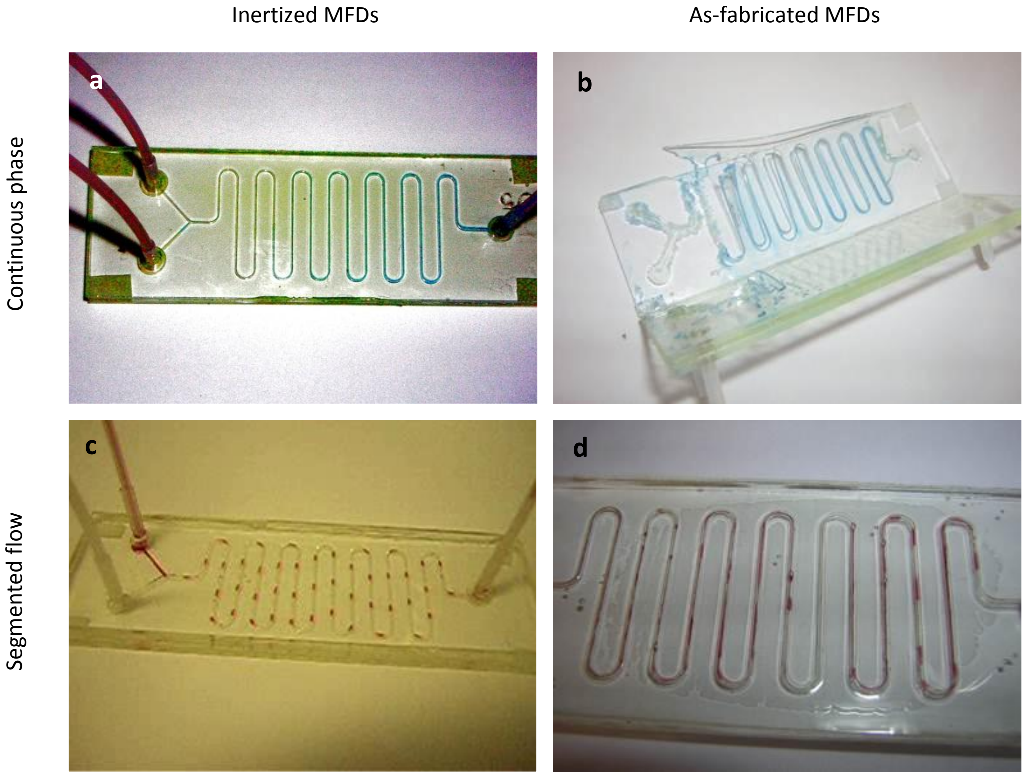

Figure 2.33. Comparison between inertized and non-intertized Y-junction devices after working for 20 minutes in aggressive envinronment. Devices treated with sol-gel precursor solutions are on the left (a,c), untreated devices are on the right (b, d). The top row (a, b) shows the MFDs working with a continuous phase while the bottom row (c, d) displays the generation of segmented flows.

In the second mixing test, the Y-junction was used to generate a segmented flow. To this end, two immiscible fluids were used, an aqueous solution of a surfactant (sodium dodecyl sulfate) and a solution tetraphenylporphyrin in DCM. The formation of the droplets was easily assayed thanks to the red color of the organic phase. The results (figure 2.33c-d) confirm what has been reported so far, with the inertized device working after 20 minutes and its untreated counterpart leaking and in general failing to generate the droplet train.

The mixing tests, whether between miscible or immiscible phases, have confirmed what was observed in the first experiments on the flushing of simple serpentine devices, regarding the increased resistance of the devices upon sol-gel treatment. Moreover, the experiment on the generation of segmented flow regime demonstrates that the sol-gel layer does not drastically change the hydrodynamic characteristics of the conduit, since the formation and the flow of the organic phase droplets was observed to be regular. All MFDs eventually started leaking, in a manner resembling the first set of experiment, with a quick failure after the first signs of delamination. This happened regardless of the segmented flow regime, thus proving that the organic segments were touching the walls of the channels and that DCM residues on the channel walls could not be “washed away” by the stream.

Conclusions

The lifetime of MFDs produced by soft photolithographic patterning of thiol-ene resin NOA 81 can be extended by deposition of a silicon dioxide layer with single or multiple sol-gel treatments. Treated microchannels displayed an increased resistance to the delaminating effects of both acetone and DCM, with a 20x increase in their working lifetime before failure. The presence of the silica layer was assayed by ATR-IR spectroscopy and did not affect the hydrodynamic behavior of the MFD that was employed for the generation of a segmented flow.

Experimental evidences, as well as the literature regarding sol-gel deposition techniques[48] suggest that the protective layer is porous and, while increasing the lifetime of the device, it cannot fully protect the thiolene resin from contacting aggressive solvents. Silicon dioxide deposited by the sol-gel method is usually thermally treated to reduce the number of pores when a dense layer is required, but this is not feasible in this case since the presence of the thiol-ene polymer limit the maximum temperature the device can be exposed to.

Experimental

Tetraethyl orthosilicate (TEOS), hydrochloric acid solution (36.5%) and absolute ethanol for the preparation of sol-gel solutions were all acquired from Sigma-Aldrich and were used without further purification. Deionized water (with a resistivity of 18.2 MΩ·cm) was produced by a Millipore Corporation deionization system. The molar ratio between in the sol-gel mixture was 1 : 2 : 16 : 0.02 (TEOS : deionized water : ethanol : hydrochloric acid). All the solutions used for treating NOA 81 samples (either open surfaces or channels) were stirred for 24 h prior to use and discarded within a few hours afterwards.

NOA 81 surfaces were prepared by injecting the liquid resin in transparent plastic molds sticked on 3’’ × 1’’ microscope glass slides (Corning Inc.). The slides were irradiated for 5 minutes at 365 nm, then the mold was removed and a second irradiation followed for 30 minutes. Thermal postcuring of the resin was carried out by letting the slides sit on a hot plate at 50 °C overnight. Silica-coating of one open surface was carried out by dip coating. The test surface was immersed in the aged sol-gel precursor solution at a 10 cm/min rate, left in solution for 30 s and then extracted at 10 cm/min. After the dip coating procedure, the sample was left drying in open air at 20 °C, 40% relative humidity for 2 hours before heating at 50 °C for 18 hours. FT-IR spectra of the NOA 81 samples were acquired with a resolution of 2 cm^{-1} in attenuated total reflectance (ATR) configuration on a Nicolet 5700 spectrophotometer with a Smart Performer ATR accessory using a zinc selenide window.

The devices used were fabricated according to the protocols outlined earlier in this chapter. NOA-81 was used for both the head and the body of the MFDs. The photolithographic masks used for the patterning of the channels are reported in figure 2.34.

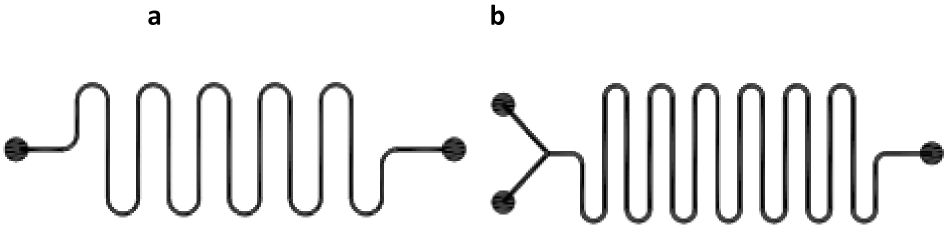

Figure 2.34. Photolithographic masks used for producing the test devices. a) devices used for inertization tests; b) devices used for mixing tests

NE-300 syringe pumps by New Era Pumping Systems Inc. were used throughout this work. MFDs that were inertized underwent a number of cycles of exposition to the aged sol-gel precursor solution. A single cycle comprised the following steps:

1. Priming with deionized water, which was pumped through the channels at 1 ml/min for 10 minutes.
2. Flushing with the sol-gel solution at 1 ml/min for 5 minutes.
3. Stopping the pump and leaving the solution resting in the channels for 20 minutes.
4. Flushing with deionized water at 1 ml/min for 10 minutes.
5. Drying by flushing nitrogen steadily for 10 minutes.

All reagents for the mixing tests, bromocresol green, DBU, tetraphenylporphyrin and sodium dodecyl sulfate were acquired from Sigma-Aldrich. For the single phase mixing, solutions in DCM of bromocresol green indicator and DBU were prepared by adding a few drops of each reagent to the solvent under stirring. The flow rate at each inlet was set at 1 ml/h. For the segmented flow experiment, 2.5 mg/ml sodium dodecyl sulfate were dissolved in water while a 1 mM tetraphenylporphyrin solution DCM was used as the red-colored organic phase. Different segmented flows were generated by varying the ratio between the flows of the water and organic phases, an example with 5:1 water : organic ratio is reported in figure 2.33c.

2.7 Managing the surface properties of NOA 81

A variety of microfluidic devices have been built in NOA that exploit its properties.[36, 37, 52, 53] However, only one of these works, by Hung et al.[54], addresses the tuning of the material wettability that represents an essential feature for a proper functioning of microfluidic chips, for instance for the production and handling of droplets.[55] In the work by Hung, the thiolene surface underwent a chemical modification by exposition to a plasma for different times. This is a standard and fast procedure but presents a series of drawbacks:

- it can only decrease the water contact angle
- the resulting contact angle is not stable over time but slowly recovers the initial value
- it works only for open geometries

This paragraph reports a flexible and simple post-functionalization protocol to tailor the wettability of NOA surfaces in an ample interval of contact angles.

The principal components of the NOA 81 resin are reported in figure 2.35. NOA 81 is a mixture of trimethylolpropane tristhiol (**1**), isophorone diisocyanate ester (**2**), trimethylolpropane diallyl ether (**3**) and a benzophenone photoinitiator (PI). The exposition to 354 nm UV radiation causes the production of a radical on the PI and crosslinking via thiol-ene chemistry between **1** and **3** (as reported in figure 2.36), or via the formation of thiouretane bond (between **1** and **2**). According to this description, the –OH groups in **2** should survive the process and remain available in the cured resin.

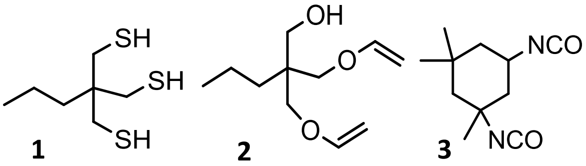

Figure 2.35. Main components of commercial NOA-81 resin. A benzophenone-type photoinitiator is added to start the polymerization.

The presence of surface hydroxide groups is typical for many inorganic materials, such as silica and alumina. One typical reaction used to anchor organic moieties to such surfaces is the condensation of hydroxide groups with chlorosilanes, yielding a siloxane bond with the release of one molecule of hydrochloric acid, as reported in scheme 2.37. Among chlorosilanes, octadecyltrichlorosilane (OTS) is typically used for the functionalization of chromatographic columns, giving silica an hydrophobic surface. On the other hand, chlorosilanes with polyethylene glycol moieties can be used to impart the material an hydrophilic character.

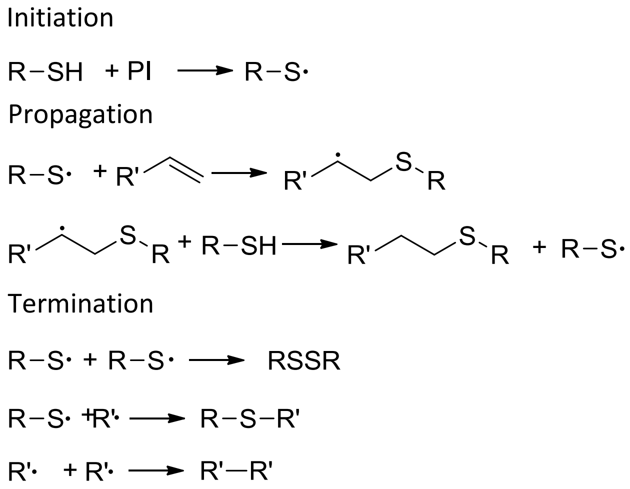

Figure 2.36. General scheme of a thiol-ene photoinduced radical polymerization.

Functionalization tests to yield hydrophobic and hydrophilic surfaces were carried out on open, flat NOA samples first, which allowed for a chemical characterization of the system via FT-IR spectroscopy as well as the observation of sessile water drop contact angles (WCA). Then, the behaviour of a water meniscus was observed in closed NOA 81 microchannels both before and after silanization. Lastly, a device comprising a Y-junction with one hydrophilic and one hydrophobic arm was fabricated and characterized.

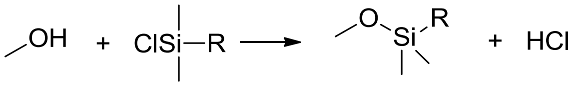

Figure 2.37. General scheme of condensation reaction of a chlorosilane with an hydroxide group.

Results and discussion

Figure 2.38 reports the 3750-2000 cm^{-1} region of the FT-IR spectra of a thin layer of NOA 81 undergoing successive exposition to UV radiation. The progressive disappearance of the bands at 2572 and 3084 cm^{-1}, assigned to the S-H and allyl C-H stretching, respectively, confirm the polymerization route described. The area at around 3500 cm^{-1}, which is typical for the stretching of hydroxide groups, presents somewhat weak peaks that are more difficult to evaluate with respect to the intensity, but appear not to be influenced by exposition time.

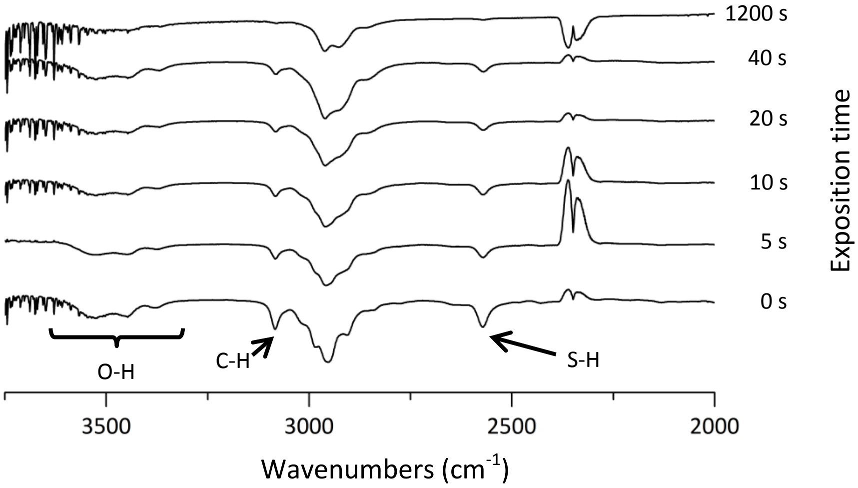

Figure 2.38. FT-IR spectra of NOA 81 resin upon UV exposition at 354 nm for different amounts of time. The disappearence of signals at 2572 cm^{-1} (S-H stretching) and those at 3084 cm^{-1} (C-H bonds stretching on allyl groups) is due to the thiol-ene polymerization reaction.

Surface functionalization tests were carried out on a number of flat NOA 81 surfaces, by exposing them to different chlorosilane solutions and then measuring the resulting sessile drop water contact angle over a period of 3 months in order to assay the stability of the surface. As reported in table 2.3, pristine NOA samples displayed a WCA of about 70°, which typically increased to about 110° upon treatment with OTS and decreased to about 45° when 2-[methoxy(polyethylenoxy)propyl]trichlorosilane (PTS) was employed. This wide range of achievable WCAs holds a very good potential for the development of application where the control of this feature is important. The uniformity of functionalization is another parameter of interest. It this experiment, it was assayed by calculating the WCAs as the average of 5 measurements carried out in random positions over the surface. The value of the mean squared error is generally very low for all samples, indicating a uniform functionalization. The change in the WCA values over the course of time was also negligible in all cases, the drift in the values being comparable to the fluctuations of the values registered for pristine NOA samples. Three images recorded for WCA measurements are reported as an example in figure 2.39.

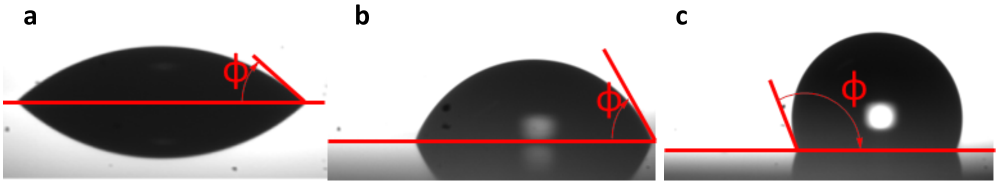

Figure 2.39. Effect of functionalization on WCA of three NOA 81 surfaces: a) hydrophilic functionalization; b) pristine, unfunctionalized resin; c) hydrophobic functionalization.

Pristine NOA						
Months passed	0		1		2	
Sample no.	WCA (°)	σ (°)	WCA (°)	σ (°)	WCA (°)	σ (°)
1	70	2	69	1	74	2
2	68	2	69	1	72	1
3	72	2	75	1	71	1

Hydrophilic NOA						
Months passed	0		1		2	
Sample no.	WCA (°)	σ (°)	WCA (°)	σ (°)	WCA (°)	σ (°)
1	44	3	46	1	46	3
2	49	3	50	2	53	2

Hydrophobic NOA						
Months passed	0		1		2	
Sample no.	WCA (°)	σ (°)	WCA (°)	σ (°)	WCA (°)	σ (°)
1	114	3	115	3	111	3
2	110	2	111	3	106	6
3	111	2	110	2	113	2
4	107	3	108	1	98	1

Table 2.3. Observed water contact angles (WCA), calculated by averaging 5 measurements carried out on random positions over the sample. Standard deviations (σ) are reported as a way to assess the uniformity of the surfaces.

An FT-IR study of the functionalized surfaces was attempted both in transmission and in ATR configurations, but did not yield satisfactory results since the signals for octadecyl and polyethylenoxy moieties were not recognizable. This was probably due to the small number of hydroxide moieties available for functionalization, compared to those in the bulk of the resin. In order to increase the number of surface groups available and ultimately observe the desired features, chunks of NOA 81 were pulverized and the powder functionalized. It was then possible to observe the signals from the octadecyl moieties in ATR configuration, as reported in figure 2.40 (in particular, the C-H bonds in the octadecyl chain resonate at 2925 cm^{-1} and 2853 cm^{-1}) while those from polyethylenoxy moieties remained elusive.

After studying open surfaces, the focus moved to the closed environment offered by microchannels. Here, the parameters describing the interaction of water with the walls are the static contact angle of the meniscus and the pressure drop caused by the friction of the liquid at the channel walls during motion. The former was measured in a way resembling the open-surface case, by injecting water in the channel and recording an image of the meniscus. The values observed for two different channels prior to functionalization, reported in table 2.4 (first entry, third column) were in good agreement with those presented in the previous paragraphs (circa 70°) as can be appreciated from figure 2.41b. Upon functionalization, the contact angle was increased to 112° (figure 2.41c) and reduced to 40° (figure 2.41a) for treatment with OTS and PTS, respectively. The filling rates were also investigated while pumping water at constant pressure, by taking a sequence of pictures of the meniscus at regular intervals. The difference in filling rates, reported in table 2.4 on the last column, confirms that the channels were functionalized in a way analogous to that of open surfaces.

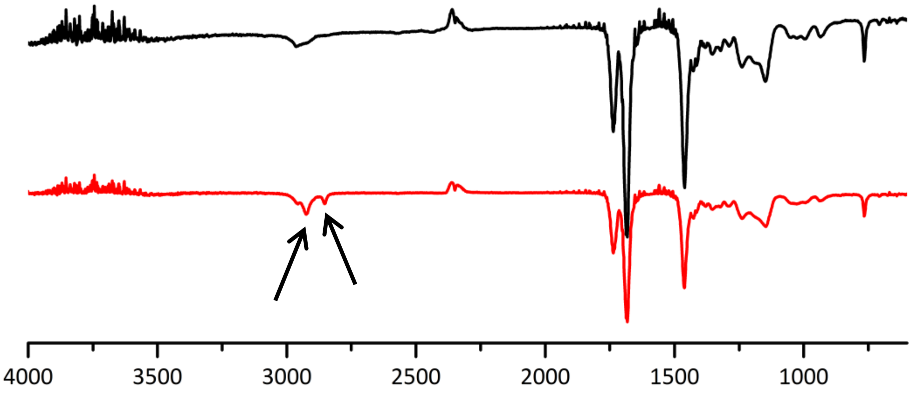

Figure 2.40. ATR IR spectrum of NOA powder before (black) and after (red) treatment with OTS. The bands highlighted can be ascribed to the C-H bonds stretching in the octadecyl chain (at 2959 cm^{-1} and 2853 cm^{-1}).

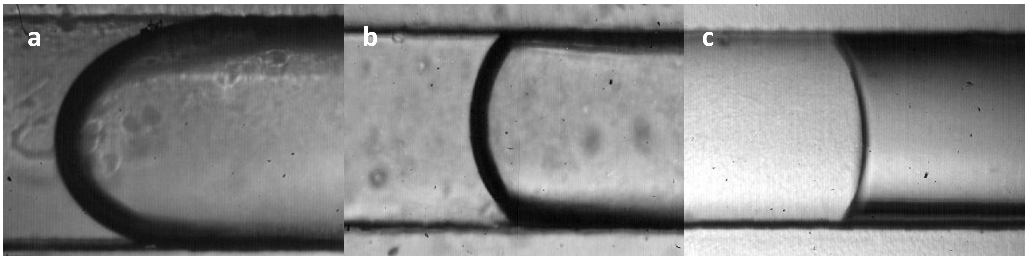

Figure 2.41. Static water contact angle at the water/air meniscus in a microchannel for a) PTS-treated NOA; b) pristine NOA; c) OTS-treated NOA.

		WCA (°)	Filling rate (mm/s)
Sample channel 1	Pristine	70 ± 5	4.6 ± 0.1
	OTS-treated	112 ± 5	2.2 ± 0.2
Sample channel 2	Pristine	72 ± 5	4.7 ± 0.1
	PTS-treated	40 ± 5	5.6 ± 0.1

Table 2.4. Static water contact angles at the water/air interface (WCA) and filling rates measured upon application of a 15 mbar pressure to the water flow.

An application of the functionalized surfaces so far described was developed by treating two "arms" of a NOA-made Y-junction with different chlorosilanes, thus imparting an hydrophilic character to an arm and a hydrophobic character to the other. A scheme of the device is shown in figure 2.42. The device was employed in an "inverted" way: water was pumped through the inlet A, and flowed through the channel with a 70° WCA till the junction. Once there, it pinned the hydrophilic channel more easily than the hydrophobic one, thus flowing in that direction only and reaching outlet C. For the same reason, organic solvents, such as toluene, only exited the device through outlet B. Figure 2.43 report a series of frames of a water front at the Y-junction. Once modified in this way, the device can work as a static valve, or as a phase separator. While the channel is still filling, the water front may still advance slightly in the hydrophobic arm, in particular when the liquid in the hydrophilic channel reaches the outlet and has to wet the Teflon tube (which displays an hydrophobic character on his own). Once the device has been primed, however, water flows towards C only.

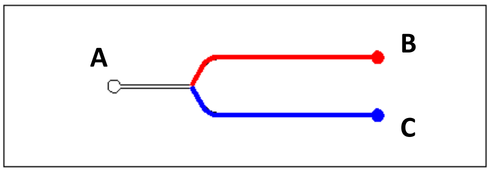

Figure 2.42. "inverted" Y-junction modified to work as a static valve/phase separator. The red channel was treated to become hydrophobic, while the blue one was made hydrophilic.

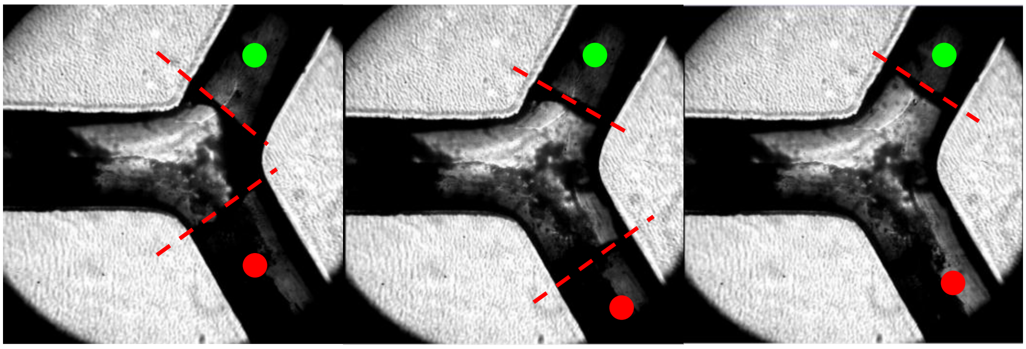

Figure 2.43. Water behaviour at the Y-junction. The red dot indicates the hydrophilic channel, whereas the green dot indicates the hydrophobic one. The water front (where visible) is also highlight by a red broken line.

Conclusions

A study of the functionalization of NOA 81 thiol-ene resin was carried out in order to control its wettability. The chemistry behind the functionalization process has been elucidated through FT-IR spectroscopy and the interaction of the surface with water was observed both for flat, open surfaces and closed microchannels with round section as well. The treatment of the resin with chlorosilane derivatives was found to be an excellent way to bring organic moieties on NOA 81 surfaces in order tune their properties. This result is general and not limited to wettability, since the chemistry of chlorosilanes is very well developed and a wealth of different derivatives are available, even on the market.

Finally, this functionalization method was exploited in the fabrication of a Y-junction that can be used as a passive valve, to selectively direct the flows of incoming organic/aqueous solvents towards different outlets.

Experimental

The polymerization process of NOA 81 resin was observed by FT-IR in transmission mode on a Nicolet 5700 spectrophotometer, by applying a layer of liquid resin on a potassium bromide disc and thinning it with a blade until a satisfactory transmittance was achieved. The disc was then irradiated with a Spectraline SB-100P handheld UV lamp (sporting a maximum intensity at a wavelength of 365 nm) for increasing amounts of time and the spectrum of the resin recorded between expositions.

Experiments on open, flat surfaces were carried out on glass microscope slides (Corning Inc.) spin coated with NOA 81 on a SCS 6800 Spin Coater (Specialty Coating Systems). Samples were spun at 200 rpm for 15 s, then brought to 2000 rpm over 10 s and spun at that speed for 30 s before slowing to stop in 10 s. The liquid NOA layer was then irradiated with a UV400 Reinraumtechnik Lanz collimated UV source for 5 minutes and allowed to postcure overnight at 50 °C on a hot plate.

A 50 ml round bottom flask was silanized, in order to be used for the preparation of all trichlorosilane solutions later on. The flask, topped with a condenser and a calcium chloride cap, was loaded with 18 ml HPLC toluene, 2 ml of octadecyltrichlorosilane (OTS, from Sigma-Aldrich) and a magnetic stir bar. It was then heated while stirring and held at reflux temperature for 2 hours. After this treatment, the inner surface of the round bottom flask appeared hydrophobic.

Functional NOA surfaces with controlled wettability were prepared by exposing NOA samples to $5\%_{vol}$ solutions of either OTS (for hydrophobic surfaces) or 2-

[methoxy(polyethylenoxy)propyl]trichlorosilane (PTS, from ABCR GmbH, for hydrophilic surfaces). Open NOA surfaces were dip in these silanizing solutions for 15 minutes. The slides were then rinsed with abundant toluene, isopropanol, dried under nitrogen flow and stored in a box until characterized.

WCAs of water droplets were measured with a custom apparatus consisting a motorized syringe pump (Ultra Micro Pump II, World Precision Instruments), collimated light and a telecentric telescope mounted on video-camera. Small drops (volume ~0.5 ml) were produced with the syringe pump and gently deposited on the surface where then image was recorded. For each image, the drop profile was fitted with a polynomial function; the error fitting procedure was typically less than ± 1°. At least five drops for each sample were analyzed to obtain statistically sound results. Then, the averages were taken as the representative contact angles and the standard deviations as the errors.

NOA powders were prepared by scratching chunks of polymerized resin with a diamond point mounted on a Dremel tool working at low speed. Two samples were prepared in this way which consisted in roughly 300 mg of material. Each powder sample was treated by suspending in one of the solutions described in the previous paragraph for 15 minutes. The samples were then filtered on paper and washed thoroughly with HPLC toluene and isopropanol, then dried under reduced pressure. Characterization via FT-IR in attenuated total reflectance configuration on a Nicolet 5800 spectrometer with a Smart Performer ATR accessory followed to qualitatively assay the chemical composition of the surface.

Two straight channels were fabricated according to the standard techniques described in chapter 2.3. The channel in this case was sandwiched between two glass plates previously spin-coated with NOA 81, so that all four surfaces were resin. The final cross section of the channel was 500 × 200 µm. After thermal postcuring, the channels were dried by flushing with nitrogen for 15 minutes, then primed with HPLC toluene before surface modification. Silanizing solutions were pumped through the channels with a New Era Pumping Systems Inc. model NE-300 syringe pump at a flow rate of 100 µl/min flow rate for 15 minutes, then the channels were rinsed with toluene (200 µl/min flow rate for 15 minutes) and flushed again with nitrogen for 15 minutes.

The static water/air meniscus and the flow of water inside the functionalized microchannels were observed with the same setup used for WCA determination on flat surfaces. In this case, water was pumped into the system with a constant differential pressure of 15 mbar and images of the moving meniscus were collected with a 50 Hz frame rate.

Finally, a demonstrator device consisting of a Y-junction was fabricated according to standard techniques (with NOA 81 head and body) by using glass slide spin coated with NOA 81. As in the case of the straight channels, this allowed to have NOA resin on all four surfaces. The channel network of the device is shown above, in figure 2.42. After the thermal postcuring, the device was flushed with nitrogen for 15 minutes, then primed with toluene. Nitrogen was then blown in from the outlet of the hydrophobic channel, while the silanizing solution containing PTS was slowly injected with a syringe by hand from the outlet of the hydrophilic channel, until the solvent front reached the Y junction, but didn't go any further. The nitrogen flow in this case served as a protection, since any extra silanizing solution injected would not enter the hydrophobic arm and would instead be quickly flushed out. The device was kept with one arm filled of silanized solution for 10 minutes, the solution was sucked back in by the syringe and the device flushed again with toluene (200 µl/min for 15 minutes). Then, the nitrogen was blown in from the outlet of the hydrophilic arm and the hydrophobic arm loaded with the OTS silanizing solution for 10 minutes. After 15 minutes wash with 200 µl/min toluene and drying under nitrogen flow, the device was ready for testing.

Acknowledgements

The characterization of water contact angles and the analysis of the images for the determination of flow rate inside functionalized channels were carried out by Dott. Davide Ferraro and Prof. Giampaolo Mistura, and the author wishes to thank them for their help and the fruitful discussions.

3. Applications of prototype chips

The fabrication techniques presented in chapter 2 were developed in parallel with a number of microfluidic applications in different fields of chemistry. Four such applications are presented in this chapter, where microfluidics is presented as a tool to carry out scientific investigation, rather than the object for the development of fabrication techniques.

An elegant application to chemical synthesis is presented in §3.1, a multilayer reactor sporting a NOA 81 head and a Parafilm M body, capable of producing a reactive intermediate *in situ* and using it to run two different reactions in parallel producing different diazo-dyes. In §3.2, then, a technique is presented to carry out an online monitoring of a dye absorption on titania. To this end, a simple microfluidic flow cell is used together with a spectrophotometric system.[56] The transparency of thiolene-made MFDs is exploited in §3.3 to carry out the LED-light driven growth of silver nanoparticles resulting in nanostructures with controlled morphologies. Lastly, a prototype MFD with built-in electrodes, whose channel network was embossed from biadhesive tape is described (§3.4), for use in electrochemical impedance spectroscopy measurements.

Every paragraph in this chapter represents an experimental work on its own, which in some cases has been carried out with the help of investigators from other departments or institutions. Proper credits is given at the end of every paragraph.

3.1 Parallel synthesis of diazo dyes

Azo compounds are a class of molecules with general formula R_1-N=N-R_2. Aryl azo compounds present aryl moieties as R_1 and R_2 substituents, thus possessing π-conjugated systems. These compounds often display intense colors, most often in the red-orange-yellow spectrum. They are therefore used as dyes and are commonly termed azo dyes, a famous example being methyl orange (figure 3.1). Moreover, many azo dyes can also be used as acid-base indicators, since the protonation/deprotonation of their functional groups is bound to change the electronic density on the molecule's delocalized π-system, thus affecting its spectroscopic properties.

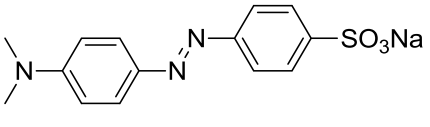
Figure 3.1. Methyl orange

The synthesis of azo compounds has been important in the development of industrial chemistry in XIX century and is often part of organic chemistry undergraduate laboratory courses, to demonstrate the function-structure relationship in organic molecules.[57, 58] The typical synthesis, reported in scheme 3.1, starts with a diazotization reaction on an aniline derivative, carried out in acid conditions in presence of sodium nitrite. This first reaction yields a diazonium salt, which is an instable intermediate due to the diazo group N_2^+ and whose tendency is to release nitrogen gas and form either an aryl carbocation or an aryl radical. For this reason, the reaction is carried out at low temperature in a water ice bath. When an electron-rich arene such as a phenol is available, however, the diazonium salt can undergo an azo coupling reaction and form the final product. Besides the coupling reaction, diazonium salt can undergo a range of other transformations, the most interesting involving alkenes such as in the Maarwein arylation (addition of the aryl residue to an electron-poor alkene)[59, 60] and the Heck-Matsuda coupling reaction, where the diazonium salts have shown a good versatility as substitutes for aryl halides traditionally used for the Heck reaction.[61]

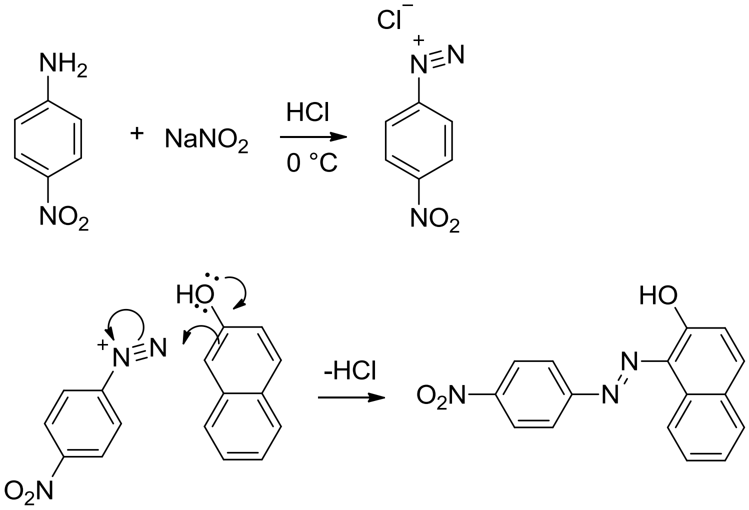

Scheme 3.1. Mechanism of the synthesis of a diazo dye, via diazotization and coupling reactions.

This study presents a three dimensional microfluidic device that carries out the diazotization reaction on sulfanilic acid at room temperature, producing the relative diazonium salts *in-situ* before performing two parallel diazo-couplings to different substrates, 2-naphthol and salicylic acid as illustrated in scheme 3.2.

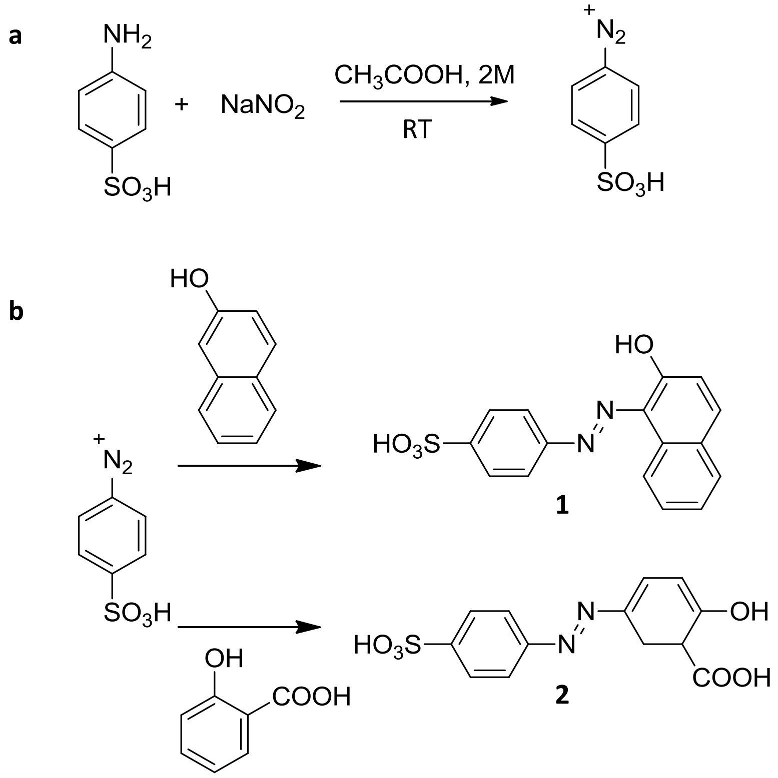

Scheme 3.2. a) Diazotization of sulfanilic acid at room temperature and b) couplings with 2-naphthol and salicylic acid to yield two different diazo dyes, **1** and **2**.

Results

The device, which can be seen with back lighting in figure 3.2, was prototyped with a thiol-ene head and a two-layers Parafilm M body (the thickness of each layer being 60 µm), separated by a glass slide. Its channel network was developed on two levels, so that the coupling reactions (scheme 3.2b), whose products are easily detected thanks to their brilliant colors, were carried out on the top level where they could be better observed. The diazotization reaction (scheme 3.2a), on the contrary, took place on the bottom level. The two levels were connected by a hole in the middle glass slide (marked with “C” on figure 3.2) after which the flow of solvent carrying the diazonium salt was divided in equal parts, each meeting a different coupling agent.

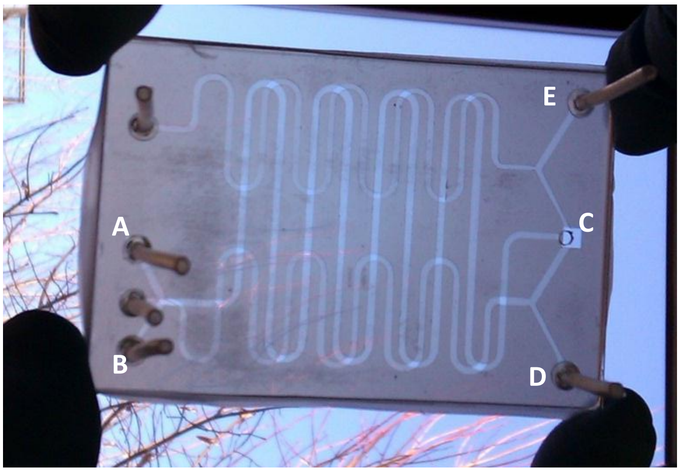

Figure 3.2. The MFD used in this work. Various features are assigned different letters for reference in the text.

The channel network was firstly fluxed with colored India inks to assay the sealing of the device and the splitting of the flow. Blue ink was used in lieu of the solution carrying the diazonium salt, while yellow and red colors were employed for the coupling agents. In figure 3.3, it can be seen how a laminar flow is established at each Y-junction, and the inks of different colors flow parallel without mixing thanks to their viscosity, which is higher than that of the solutions used for the diazo coupling. This effect helps in confirming the correct working conditions of the device regarding the splitting of the blue ink, which appeared to be in steady state, without noticeable fluctuations over time.

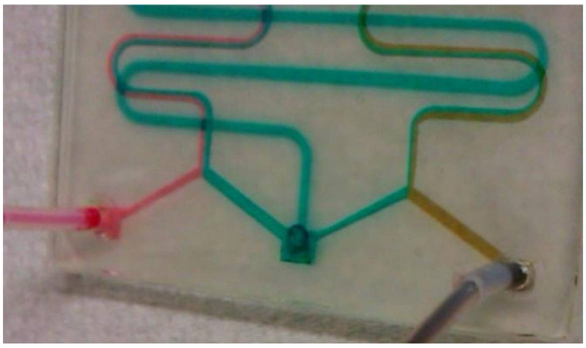

Figure 3.3. Detail of MFD testing with colored india inks.

During the synthesis of the dyes, the sulfanilic acid together with the catalyst (acetic acid) were fluxed through inlet A, and mixed with 2.5 eq of sodium nitrite from inlet B. The serpentine along the bottom level of the chip (with a volume of about 140 µl) allowed for mixing and reacting of the reagents, then the flow was split in two parts in C, and each part was mixed with 1.0 eq of coupling agent incoming from inlets D and E, in the serpentines on the top level (each with a volume of 80 µl). No evolution of nitrogen was observed during the process, meaning that the diazonium salt did not get degraded and instead reacted with the phenols, even though the reaction mixture was kept at room temperature (as opposed to the traditional synthesis, which is carried out at about 0 °C). To a first approximation, the diazonium salt holdup in the reactor at any instant cannot exceed the concentration of the limiting reagent in for its production, sulfanilic acid, times the total volume of the reactor. This is, of course, an overestimation, since it hypothesizes an immediate and total diazotization of sulfanilic acid at the first Y-junction and no consumption of the diazonium salt for the coupling reaction. Since the total volume of the reactor can be estimated as 300 µl, one can expect the total amount of diazonium salt never to exceed 4.5 µmol, thus ensuring safe operations.

The reaction yielding the colored compounds clearly took place on the top level, as shown in figure 3.4. As the thickness of the microchannel is of the order of 60 µm, only the dark-colored solution of product (**1**) can be appreciated, whereas only a faint color was visible with naked eye in the serpentine where (**2**) was forming. Both dyes can however be seen in the relative collection vials, confirming the outcome of the synthesis.

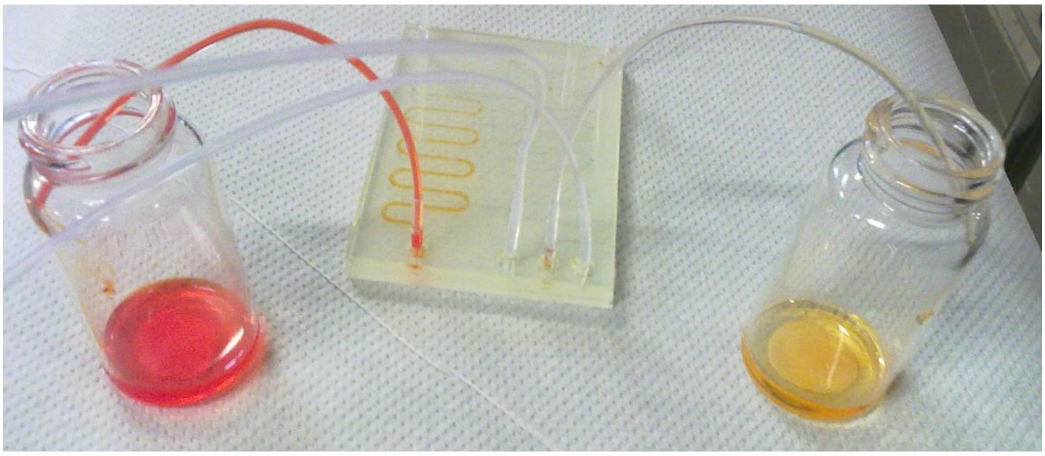

Figure 3.4. Formation of coloured diazo dyes.

The same procedure was also carried out with 4-nitroaniline as a starting material replacing sulfanilic acid. The coupling product with 2-naphthol, however, displayed poor solubility and precipitated in the microchannel, clogging the system which needed to be rinsed with abundant ethanol before it could be used again. Interestingly, the device survived the clogging and could be used again afterwards.

Conclusions

This study exemplifies many interesting features of microfluidic technology, together with the flexibility of the fast prototyping techniques that have been outlined in the second chapter of this thesis. Here, microfluidics is highlighted as an enabling technology that allows a safe, *in situ* production of a reactive (and potentially explosive) intermediate with very low holdup and its immediate use for parallel syntheses of different derivatives, by working at room temperature without the need for cooling. It should be noted that, while only salicylic acid and

2-naphthol were used in this study, it would be easy to design a similar MFD for an increased number of parallel couplings, by splitting the diazonium salt flow in more fractions, allowing for the fast, high throughput screening of reaction products. Moreover, the first layer of this prototype chip makes very reactive and flexible intermediates, such as diazonium salts, readily available for any further chemical reaction.

Experimental

The fabrication protocol for multilayered devices has been reported earlier, in paragraph 2.4; here, only the channel and drilling patterns for the two body layers and the head, respectively, are reported in figure 3.5.

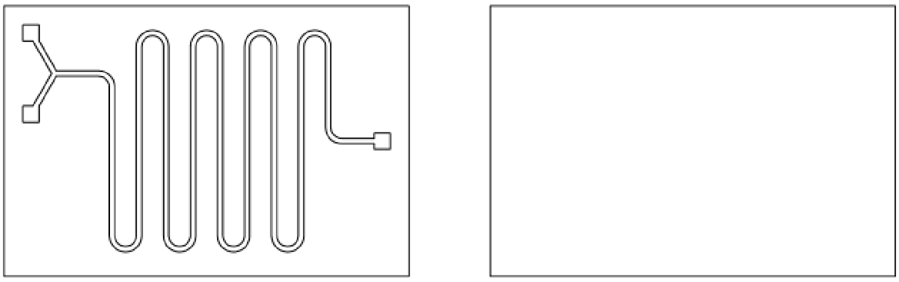

Bottom level

Bottom glass slide

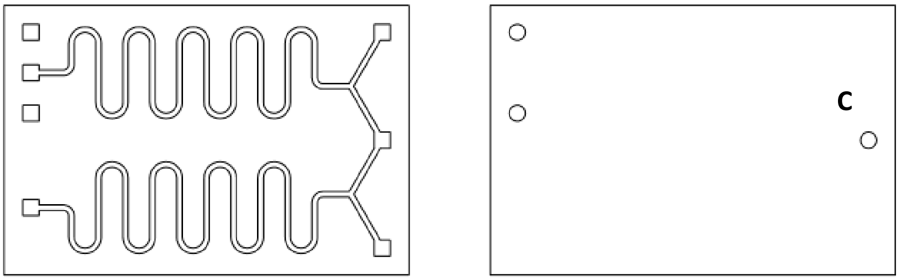

Top level

Middle glass slide

Head

Figure 3.5. Design of the MFD used in this work. On the left column are the channel patterns cut on Parafilm M; on the right column are the drilling patterns of the glass slides, from the bottom to the top of the reactor. For reference, the letters markings correspond to those in figure 3.2.

New Era Pumping Systems Inc. model NE-300 syringe pumps were used throughout this work. Colored India inks were used as tracers to check the sealing of the device. All chemicals were received from Sigma-Aldrich and used without further purification. The four solutions injected in inlets A, B, D and E for the syntheses were prepared as follows:

- Solution A: 0.30 mmol (52.0 mg) of sulfanilic acid were dissolved in 10 ml of a 2 M aqueous solution of acetic acid.
- Solution B: 0.75 mmol (51.8 mg) of sodium nitrite were dissolved in 10 ml deionized water.
- Solution D: 0.15 mmol (21.6 mg) of 2-naphthol were dissolved in 10 ml absolute ethanol
- Solution E: 0.15 mmol (20.7 mg) of salicylic acid were dissolved in 10 ml absolute ethanol

All solutions were pumped with equal rates (20 µl/min, 1.2 ml/h) in the respective inlet, both during testing with inks and during the synthesis of the dyes.

3.2 Online monitoring of dye absorption on titania

Dye-sensitized solar cells (DSSCs)[62] are attracting widespread academic and industrial interest as a low-cost alternative to conventional silicon solar cells. Since the pioneering work by O’Regan and Grätzel in 1991,[62] the performances of DSSCs have been remarkably improved and overall power energy conversion efficiencies up to 11.1% for N719 dye (figure 3.6b),[63] over 10% for “black dye” (figure 3.6a),[64] and 11.5% for C101[65] have been reported. However, fabrication of state-of-the art devices is far from being a straightforward and reproducible process. Device production is indeed a rather complex multistep procedure in which a number of steps have not been fully rationalized yet. As a consequence, the fabrication of a DSSC is often based on the meticulous repetition of reported protocols and subjected to a large batch-to-batch variability making difficult to evaluate univocally the real performance of a new dye as well as the impact of an innovative electrolyte. From the industrial viewpoint, it is unlikely that fabrication procedures, originally optimized for prototype cells, are implemented to scale up the manufacture of DSSCs, not to mention the fact that a low reproducibility contrasts with the strict industrial quality control criteria. These issues are inevitably affecting the development of DSSC technology.

In this section, the adsorption of organic dyes on the surface of TiO_2 photoanode, an important process in the fabrication of DSSC, will be assayed. The general procedure for photoanode dyeing contemplate its immersion in a solution of the dye for 15-20 hours. A number of variables affect this process, such as immersion time, dye solution concentration, the choice of the solvent, presence of additives, temperature of the bath. Many literature reports focus on the hastening of this process. Grätzel himself described a procedure for the preparation of DSSCs with good efficiencies, based on a static impregnation of the 12 µm-thick TiO_2 photoanode with 20 $\mu l/cm^2$ of a 2×10^{-2} M solution of N719 dye. The high concentration of the dye solution, in that case, allowed for a very short sensitization time.[66] More recently, Holliman et al. reported on a 10 minutes, continuous flow sensitization method working at 50 °C.[67]

In order to study the kinetics of the adsorption of the dye, the general procedure consist in the determination by spectrophotometric means (UV-Vis) of the concentration of the dye in the solution contacting the photoanode at various time during the impregnation process. However, the dye displaying a very high absorption coefficient, this technique work only for concentrations well below those generally used for the actual sensitization processes. Photoanodes themselves can be extracted from the bath for analysis, but in this case they need to be rinsed to remove any trace of un-adsorbed dye, then dried to remove the solvent.

Such treatment can alter the sensitization process resulting in inaccurate data, especially for dyes that can bind only weakly to the surface. *In-situ* monitoring presents many advantages over the techniques described so far. For example, Peic et al. recently used optical fibers to monitor the adsorption of N719 on a porous titania film prepared on top of a gold substrate, using prism coupling to create a waveguide in the nanocrystalline film.[68]

In this study, the performance of a continuous flow sensitization technique was assayed in real-time with a novel custom setup and compared with the traditional dipping impregnation process. To this end, UV-Vis spectrophotometry was employed by interfacing a simple MFD (NOA 81 head, Parafilm M body) with an optical fiber system.

In the flow experiments, dyes were allowed to flow through the cell at a constant rate (200 µl/min) so that the TiO_2 substrate was always in contact with a fresh solution rather than with a stagnant dyeing bath, in which concentration gradients are easily developed. The dye can thus be considered in a steady state concentration, simplifying the kinetic modeling of the process. Moreover, the use of an optically transparent TiO_2 layer composed of nanoparticles with a diameter well below the critical diameter for light scattering in the visible spectral range allowed the direct monitoring of dye loading under transmission conditions along the entire film thickness. As a result, a signal with an optimal signal/noise ratio was recorded. Two benchmark dyes for DSSCs were employed, namely cis-bis(isothiocyanato)bis(2,20-bipyridyl-4,40-dicarboxylato)ruthenium(II) (N3, see figure 3.6a) and di-tetrabutylammonium cis-bis(isothiocyanato)bis(2,20-bipyridyl-4,40-dicarboxylato) ruthenium(II) (N719, figure 3.6b) and two concentrations were considered for the dyeing bath, i) 0.5 mM, usually adopted for dyeing by impregnation and ii) 5.0 mM, in order to study the effect of concentration on dyeing kinetics.

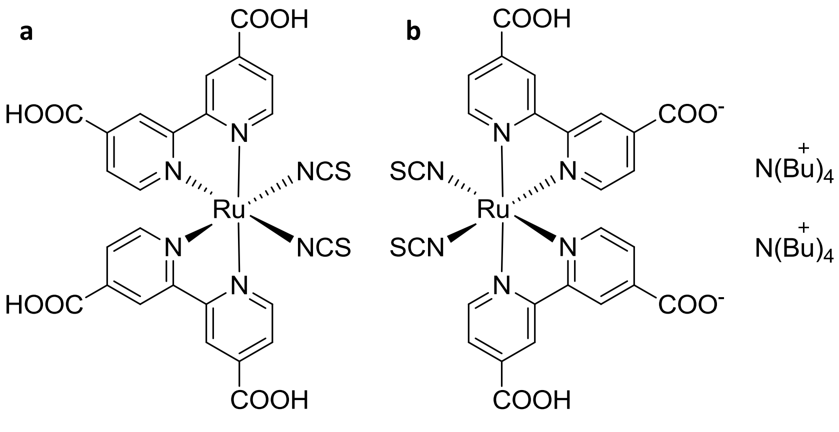

Figure 3.6. Dyes employed in this work: a) N3; b) N719.

Results and discussion

N719 and N3 showed markedly different uptake kinetics, the loading of N719 on TiO_2 being much slower than N3 (Figure 3.7). This difference can be explained considering that N719 dye carries two tetrabutylammonium counter ions, whose steric hindrance slows down the absorption process. For both dyes, the absorption kinetic curve shows two main contributions: a first, rapid growth, in the range from tens to hundreds of seconds, followed by slow absorption increase, in the range of hours, indicating a two-step process for dye uptake. The first step can be satisfactorily modeled by a pseudo-first order kinetic process:

$$\mathrm{T} + \mathrm{D} \overset{k_1}{\rightarrow} \mathrm{TD}$$

$$\frac{\partial[\mathrm{TD}]}{\partial t} = k_1[\mathrm{T}][\mathrm{D}] = k_1'([\mathrm{T}]_0 - [\mathrm{TD}]) \qquad (3.1)$$

$$[\mathrm{TD}] = [\mathrm{T}]_0\left(1 - e^{-k_1' t}\right) \qquad (3.2)$$

where T refers to the sites of the TiO_2 surface available for dye attachment, D and TD indicate the dye in solution and loaded onto the TiO_2 surface, respectively. k_1 is the kinetic constant for the direct reaction, while the inverse process is not considered, being assumed to be much slower. Fresh dye solution is constantly fluxed and the microfluidic chip works in steady state conditions, so the dye concentration in the dyeing solution, [D], can be considered constant during the observation and its value incorporated in k_1, thus obtaining the pseudo-first order kinetic constant for dye absorption, k_1'. In addition, the free sites on titania, [T], are related to the total sites initially available, $[T]_0$, and to those already occupied, [TD], by the following mass balance,

$$[\mathrm{T}] = [\mathrm{T}]_0 - [\mathrm{TD}] \qquad (3.3)$$

The second contribution to the loading curve was a slow, linear growth of the dye uptake, which can be fitted by a zero-order kinetic law:

$$[\mathrm{TD}] = [\mathrm{TD}]' + k_2 t \qquad (3.4)$$

Where [TD]' refers to the amount of dye loaded at the time when the absorption kinetics changes from the fast to the slow stage. Two step kinetics for N3 uptake has been firstly remarked by Fillinger and Parkinson,[69] who explained it as due to the two carboxylic groups involved in binding the TiO_2 surface. More recently, Holliman et al. observed the same behavior,[67] attributing it to the several processes that are believed to take place during the dye loading, namely rapid surface adsorption along with slower mass transfer.

As expected, the pseudo-first order phase becomes faster upon increasing the dye concentration (figure 3.8a). In contrast, the slower contribution (figure 3.8b) is independent from the concentration of the dye, in line with a zero-order profile. Final dye loading obtained by static impregnation is not affected by dye concentration (entries 1 and 2 in table 3.1). On the other hand, under continuous flow conditions, the loading of the N3 increases by 30% upon changing the concentration of the dyeing solution from 0.5 mM (entry 3) to 5.0 mM (entry 4). It is worth nothing that the dye loading in flow is markedly lower than the one under static conditions in both the cases under study.

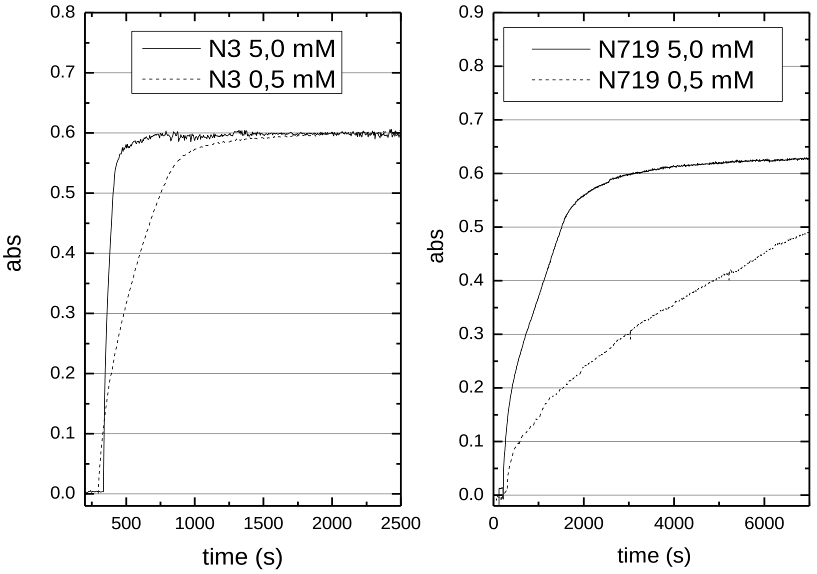

Figure 3.7. Dye uptake of N3 (left) and N719 (right) at different concentrations (0.5 and 5.0 mM in ethanol)

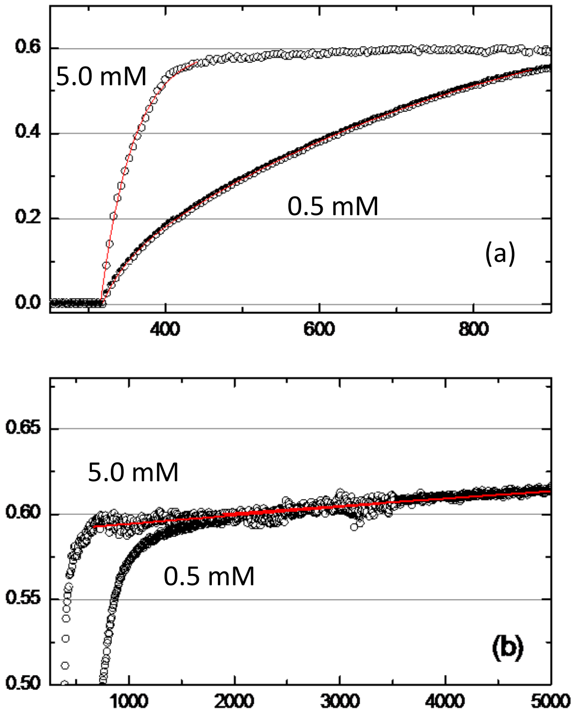

Figure 3.8. Fitting of dye uptake curves for N3 at different concentrations. Equation 3.2 models the initial, fast uptake in (a), while in (b) equation 3.4 fits the slower kinetic regime.

This difference can be rationalized in terms of the kinetic behavior of the dyeing process. Under flow conditions, the *quasi*-plateau regime, reached rather quickly, corresponds to the end of the fast, pseudo-first order, kinetic phase of the N3 dye uptake. During this stage, only about 60–70% of the maximum amount of dye is loaded onto the TiO_2 layer. As a confirmation, an estimation of the amount of the dye loaded under flow conditions at 20 hours on the basis of the zero-order kinetic constant led to a value comparable with that achieved under static conditions. The behavior of N719 is markedly different since both dynamic and static dyeing yield a similar dye loading upon concentration increase. This is likely due to a leveling effect resulting from the slower binding kinetics of N719 with respect to N3. By comparing the pseudo-first order kinetic constants, an increase of almost one order of magnitude in the value of k_1' under dynamic loading (from 2.8 to 22 s^{-1} by increasing dye concentration from loading at 0.5 to 5.0 mM) was recorded for N3. In the case of N719, k_1' increase was not as relevant as recorded for N3 (0.4 to 1.0 s^{-1}). This implies that, for short dyeing times, the rate in loading for N719 is not fast enough to allow a significant increase in the overall dye content.

Entry	**Dye**	**Method**	**[Dye]**	**Adsorbed dye***	k_1'	k_2	**PCE**
			(mM)	(M/mm^3) × 10^7	(s^{-1}) × 10^3	(M · s^{-1}) × 10^6	(%)
1	N3	Static	0.5	3.56	0.9	-	5.82
2	N3	Static	5.0	3.54	-	-	5.39
3	N3	Flow	0.5	1.81	2.8	4.4	4.39
4	N3	Flow	5.0	2.58	22.0	4.6	5.29
5	N719	Static	0.5	2.48	0.3	-	6.86
6	N719	Static	5.0	2.60	-	-	6.96
7	N719	Flow	0.5	1.68	0.4	4.2	5.39
8	N719	Flow	5.0	1.70	1.0	4.9	6.09

Table 3.1. Kinetic experimental data, dye loading quantification and photoconversion efficiency (PCE) of DSSCs sensitized with N3 or N719 under different dyeing regimes. Static impregnations were carried out over 20 h; a 200 µl/min flow rate was used for flow impregnations. *Determined by UV-Vis spectroscopy upon removal of the dye with aqueous 0.1 M NaOH.

Sequential UV-Vis measurements carried out at increasing dyeing times for static loading using a 0.5 mM dye solution indicate almost the same value of k_1' for static as well as dynamic impregnation in the case of N719, while a remarkable increase (0.9 to 2.8 s^{-1}) was recorded for N3. The shape of the entire loading curves for N3 and N719 dyes is the same for both loading methods and the zero-order kinetic constants for N3 and N719 are almost identical. These data imply that the same mechanism is operating for both dye uptake.

The k_1' increase from static to dynamic loading of N3 is most likely due to the slower mass transfer process taking place when N3 is immobilized onto titania by static impregnation: concentration of dye molecules available for grafting is depleted at the surface contact between dye solution and TiO_2. In the case of dynamic uptake, no depleted regions are present at the interface, due to the continuous refilling of dye molecules by the flowing solution. The value of k_1' is almost the same for N719 in static and dynamic uptake for 0.5 mM solution, probably as a result of the ammonium counter ions that slow down the uptake rate. This latter effect results thus predominant if compared to the mass transfer process (in contrast, N3, though still binding with two carboxylic functions, possesses four acidic groups for which the absence of counter ions translates into faster kinetics). Interaction of dye molecules with the TiO_2 surface was investigated with infrared spectroscopy in order to verify if different loading approaches could result in different grafting modes. However, infrared analyses showed no differences between cells sensitized with different techniques, thus indicating that N719 and N3 dyes graft on the titania surface in only one way, irrespectively of the sensitization technique.

Further studies were carried out on DSSCs fabricated with photoanodes impregnated by the static and flow techniques thus far described. These measurements are not reported in detail here, but different dye loadings were reflected by dissimilar photo conversion efficiencies for DSSCs fabricated under static or dynamic impregnation (table 3.1, last column). For both N3 and N719, photoanodes prepared by static impregnation presented slightly better photovoltaic performances than those prepared in flow. This result is in line with the lower dye loading achieved under dynamic impregnation (see the “adsorbed dye” column in table 3.1). In all the cases, the concentrated dyeing solutions led to improved functional properties. In particular, differences of about 9% and 12.5% in photo conversion efficiencies were recorded for N3 and N719 dyes, respectively, for the best operating cells by different impregnation protocols.

Conclusions and perspectives

This study sharply points out that care should be taken when comparing dynamic and static impregnation. The two approaches give indeed very similar results only if compared homogenously in terms of dye loading and contact time. Nevertheless, dynamic sensitization is a powerful tool towards the reproducible fabrication of DSSCs through the full control of the critical parameters of the dyeing process. Moreover, and perhaps more relevant, it is expected to be strategic for the co-sensitization of photoanodes with dyes of complementary absorption spectra.[70-73] A sequential loading of more than one dye at concentrations chosen *a priori* is expected to be possible under flow conditions.

Experimental

The experimental setup used for data acquisition in flow experiments is reported in figure 3.9. The fluidic part of the apparatus was made according to the fast prototyping procedure previously reported, with a head made in NOA 81 resin and a Parafilm M layer providing sealing between the head itself and a FTO substrate carrying the TiO2 layer to be impregnated (both the head and the gasket can be seen, assembled on a normal glass slide, in figure 3.10). The flow-cell was lined inside a black plastic box, **D**, carrying two built-in optical lenses serving as collimators for optical coupling of the flow-cell with the light source, **A** (Avantes HL-2000-LL halogen lamp) and the UV-Vis spectrophotometer **B** (AvaSpec-2048). A syringe pump (NE-300, by New Era Pumping Systems Inc.), **C**, was employed to flux the cell with either ethanol, for conditioning the TiO2 layer before the dyeing or removing excess dye after the sensitization, or with a the dye solutions. A 200 µl/min flow rate was used for all flow sensitization procedures.

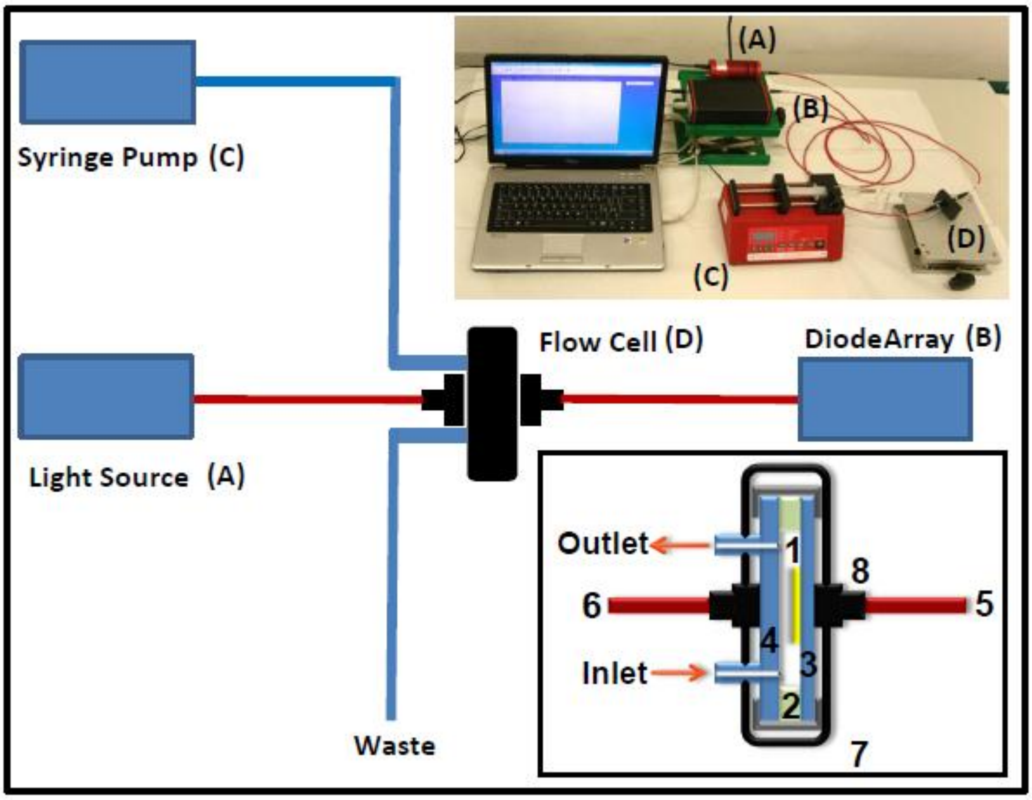

Figure 3.9. MFD integrated in a UV-Vis monitoring system. The inset details the flow-cell components. 1 – TiO_2 layer; 2 – Parafilm M gasket; 3 – FTO glass; 4 – NOA 81 head; 5 – optical fiber to the spectrophotometer; 6 – optical fiber from the light source; 7 – black box for shielding the flow cell from ambient light; 8 – optical lens for light collimation.

The real-time monitoring of the dyeing process was carried out by interfacing the UV-Vis spectrometer to a personal computer running the data acquisition/elaboration dedicated software (Avantes AvaSoft 7.5.3). Absorption was monitored at three different wavelengths. Wavelengths corresponding to the absorption maxima of the dyes were monitored since they provide the maximum sensibility for the analytic method, but the corresponding signals reach a saturation value (absorbance > 2.5 a.u.) well before the dyeing process is finished. Thus, absorbance was also monitored at wavelength far from the absorption maxima, that allowed to witness the whole process. Since the dyeing solution is relatively diluted and the optical path of the flow cell is less than 1 mm, it is reasonable to assume that the recorded absorbance is proportional only to the dye uptake, without any need of considering the contribution of the dye in solution.

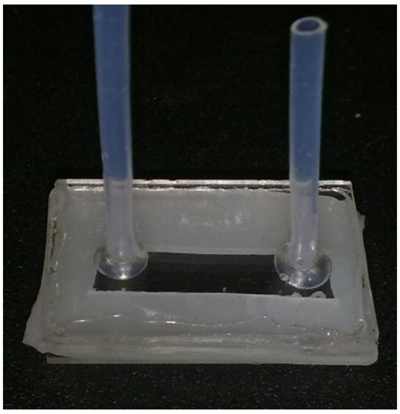

Figure 3.10. MFD head and parafilm M gasket, mounted on a microscope glass slide.

Static impregnations were carried out by dipping of the titania-bearing FTO glass in ethanol solutions of the dyes for 20 hours, then removing the samples and washing with abundant ethanol.

Quantification of dye loading on titania layers at the end of impregnation experiments was carried out by washing the samples with an aqueous 0.1 M NaOH solution to remove the dye, which was then quantified by UV-Vis spectrophotometry on a T80 PG instruments spectrophotometer, using 1 cm quartz cells, by comparison with calibrated solutions.

Acknowledgements

The data presented in this paragraph, together with a more in-depth study on the performance of the DSSC produced, have been published in 2011 on Chemical Communications.[56]

The author of this thesis would like to thank in particular Prof. Tommaso Carofiglio for the important contribution to the setup of the measurement system and dott. Enrico Frison for the hours of experimental work devoted to the project.

3.3 Photochemical synthesis of metal nanoparticles

The number of applications of silver nanomaterials in the last years has increased considerably, in fields such as optoelectronics,[74] surface plasmon spectroscopy[75, 76] and biomedicine, just to name a few.[77] On the nanometric scale, matter exhibits properties that can vary significantly from the bulk. A few examples are the change of plasmon frequency leading to the color change in gold (AgNP), copper (CuNP) and silver nanoparticles(AgNP), the modification of energy gaps between the valence and conduction bands in semiconductors due to quantum confinement[78] and the paramagnetic behavior of magnetic nanoparticles even below the Curie temperature of their bulk counterparts. Mechanical properties are affected, too, so copper nanoparticles smaller than 50 nm are considered super-hard materials that do no exhibit the same malleability as the bulk metal. The high surface-to-volume ratio and high radii of curvature provide a tremendous driving force for diffusion, and open up a wealth of possibilities in the field of catalysis.[79, 80] Lastly, the interactions of nanomaterials with living organisms is subject of research and debate, with a broad range of possibilities and dangers, many of which have not been explored up to this day.[81, 82]

The examples reported above highlight how the achievement of a complete control over the morphology of the metal nanoparticles has become one of the main goals of nanosciences in general.[83] The synthetic routes for the preparation of metal nanoparticles, can be divided into three broad categories: (i) physical vapor deposition (PVD), (ii) ion implantation and (iii) wet chemistry. PVD techniques rely on the evaporation of the metal and its condensation on a surface. Evaporation can occur in high temperature/vacuum conditions, or by bombardment of a metal target with a laser beam (pulsed laser deposition), an accelerated cloud of plasma (sputter deposition) or an electron beam (electron beam PVD). The use of PVD results in a surface covered with a metal nanoparticles layer. With ion implantation, on the other hand, metal ions accelerated by an electric field are shot on a target (glass, polyurethanes and silicones are just a few examples) which they penetrate. These atoms are allowed a certain mobility in the medium, so they tend to aggregate and form structures, resulting in a solid medium with embedded nanoparticles. Lastly, in wet chemistry methods, metal ions in solution are reduced to obtain a suspension that can be more or less stable over time. In this case, the two processes of nucleation and growth concur to the formation of the final suspension and the relative rate of these two processes have a strong impact on the morphology of the final products.

From a thermodynamic point of view, growth is always favored over nucleation because the addition to a preformed surface requires less energy than the formation of a new surface from scratch. From a kinetic point of view, the faster nucleation is compared to growth during the reduction of the metal ions, the more particles will be formed and the less they will grow, resulting in a large number of small particles. On the other hand, when growth is faster than nucleation, the opposite happens and the resulting samples show fewer particles with larger radii.

Once all the metal ions in solution have been reduced and have coalesced, the resulting nanoparticles are still in a dynamic equilibrium, constantly exchanging material with the suspending medium and possibly undergoing coarsening effects commonly known as Ostwald ripening. The activity of the metal on the surface is described by the Gibbs-Thomson equation, which relates the ratio between the interfacial activity a_{int} and the equilibrium activity (in this case, solubility) a_{eq} of the metal atoms of a particle to the surface curvature of the particle itself, given by its radius r:

$$\frac{a_{int}}{a_{eq}} = e^{\frac{r_{critical}}{r}} \tag{3.5}$$

Where

$$r_{critical} = \frac{2\gamma V_{atom}}{K_b T} \tag{3.6}$$

γ being the surface tension, V_{atom} the atomic (or molecular) volume, K_b the Boltzman constant and T the absolute temperature.

By thinking of a dispersion of spheres with a distribution of radii, the interface activities a_{int} of metal atoms depend not only on the solubility of the atoms themselves, but also on the Gibbs-Thomson relation. As a consequence, the concentration far away from a particle interface is no longer the solubility a_{eq} but is determined by a mean field value, set by the whole ensemble of spheres. This value is referred to as a_{bulk} and its value is greater than the equilibrium activity

$$a_{eq} < a_{bulk} \tag{3.7}$$

The gradient of the activity is the driving force of diffusion phenomena, according to Fick's first diffusion law

$$J = -D\frac{\partial a}{\partial x} \tag{3.8}$$

where J is the molar flow per unit of surface per unit of time, D is the coefficient of diffusion and the gradient is calculated over the direction perpendicular to the surface of the particle, x.

To describe the dynamics of the equilibrium of the metal nanoparticles in suspension, it is convenient to define another radius, r^*, as the radius of a sphere which has an interface activity of metal ions equal to a_{bulk}. A particles with radius r^* will have an null average activity gradient and will therefore not grow. For smaller particles, $r < r^*$ and as a consequence $a_{int} > a_{bulk}$, meaning that there will be a net diffusion from the particle to the medium, making smaller particles shrink. On the other hand, particles with radii larger than r^* will grow. It should be noted that the values of both r^* and a_{bulk} will evolve over time, the latter tending to a_{eq}, which it would only reach in the case of a single particle of infinite radius (in that case, $a_{int} = a_{eq}$ would also be true).

Both γ and T are variable controlling the size of the nanoparticles being produced by tuning the relative ratio of nucleation and growth phenomena. Strong reducing agents, for example, hasten nucleation resulting in large quantities of small particles. Temperature affects both nucleation and growth and, typically, higher T favors the formation of larger particles, by destabilizing them, thus reducing the term $r_{critical}$ in equation 3.5. The typical route to control γ, is the use of capping agents, molecules that weakly adsorb on the surface of the particles, thus shielding them from addition of reduced atoms (slowing growth) by setting up an extra energy barrier and increasing γ and $r_{critical}$. These molecules also stabilize the particles in the coarsening stage following nucleation and growth.

Many reducing agents are available for the production of metal NPs, the most widely used being hydrides, especially $NaBH_4$, exploited in the Brust method for the preparation of AuNPs,[84] and citrates, as in the Turkevich method.[85, 86] Sodium citrate has the advantage to present three carboxylic groups that can adsorb on the metal surface in a reversible way, which make it a common capping agent as well as a thermal-activated reducing agent. The activation of citrate involves decarboxylation and formation of reactive radicals which readily react with metal ions. The effects of heating, however, are controversial as to the final morphology of the NPs, as described above, so that the Turkevich method (like other analogue methods for metals other than gold) is known to produce rather large particles with a high degree of polydispersity. Photoinitiators such as benzophenones offer a low-temperature way to produce reducing radicals.

Stamplecoskie et al. investigated a novel, seed-mediated growth process of AgNPs in 2010,[87] proposing a commercial Igracure photoinitiator (I-2959, produced by BASF), or 4-(2-hydroxyethoxy)phenyl-(2-hydroxy-2-propyl)ketone, as a photoactivated reducing agent for the production of silver seeds, whose mechanism of action is reported in figure 3.11. The author then goes further, employing light emitting diodes (LEDs) to irradiate AgNP suspensions, driving the Ostwald ripening process towards the formation of larger NPs by exciting specific surface plasmons and causing an anisotropic reduction of surface energy, γ. Silver atoms were therefore added preferentially where the surface energy is reduced in this way, resulting in the growth of AgNPs along specific direction and ultimately in the formation of NP with controlled morphologies.

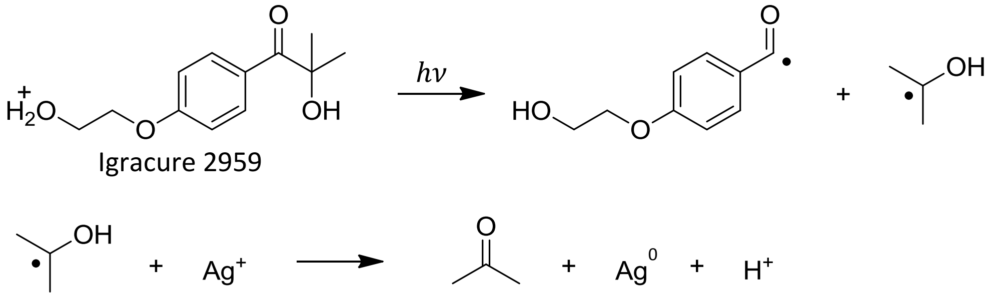

Figure 3.11. Silver reduction with I2959 photoinitiator

The light-induced shape conversion phenomenon for AgNPs had been reported back in 2001 by Jin and coworkers, for the formation of triangular nanoprisms through the illumination of a colloidal suspension with conventional fluorescent light for times spanning from 40 to 70 hours.[88]. Stamplecoskie, on the other hand, used monochromatic light for this process and observed the formation of AgNP with different morphologies, depending on the wavelength used for the irradiation, over the course of few hours.

In this work, Stamplecoskie's seed-mediated method for the control of AgNP morphology is further improved by the use of MFDs coupled with LED illumination systems, resulting in a multistep process capable of delivering NP with decahedral, triangular, hexagonal and cylindrical shapes. The seed generation step is also transposed from a batch to a continuous flow process, by adapting a photoreactor to use with a continuous flow setup.

Results and discussion

A scheme for the whole process for the preparation of silver colloids with controller shapes is reported in figure 3.12. In the first step, the preparation of seeds, it is important to produce small particles that can later be grown. An aqueous mother solution consisting of all the starting materials was de-oxygenated and pumped through a PTFE tube (0.5 mm inner diameter) coiled around a photoreactor for the activation of I2959 with its UV-A radiation. Reaction time was tuned by varying the flow rate, and the silver colloid was characterized by UV-Vis spectroscopy.

An induction time of a few minutes was observed at this stage, which was necessary for the depletion of oxygen gas absorbed in the material of the tube. A yellow color could then be spotted in the solution, and it varied from intense and clear, to light and opalescent, by increasing exposition times. Figure 3.13 reports the UV-Vis spectrum of different colloids. Small nanoparticles with a radius of about 3 nm were nucleated, which present a surface plasmon band centered at 402 nm, consistent with the data reported in literature for the dipolar plasmon absorption of AgNP in this size range.[89] An exceedingly long exposition to the unfiltered, low-pressure mercury lamp, provoked a quick aggregation of the nanoparticles (as proved by the opalescent hue of the products and the low absorbance of the red spectrum in figure 3.13). On the contrary, this was not an issue when the seeding was carried out in a quartz cuvette exposed to a UV source filtered with a bandpass filter centered at about 300 nm. A 8 minutes exposition time was usually employed in that case.

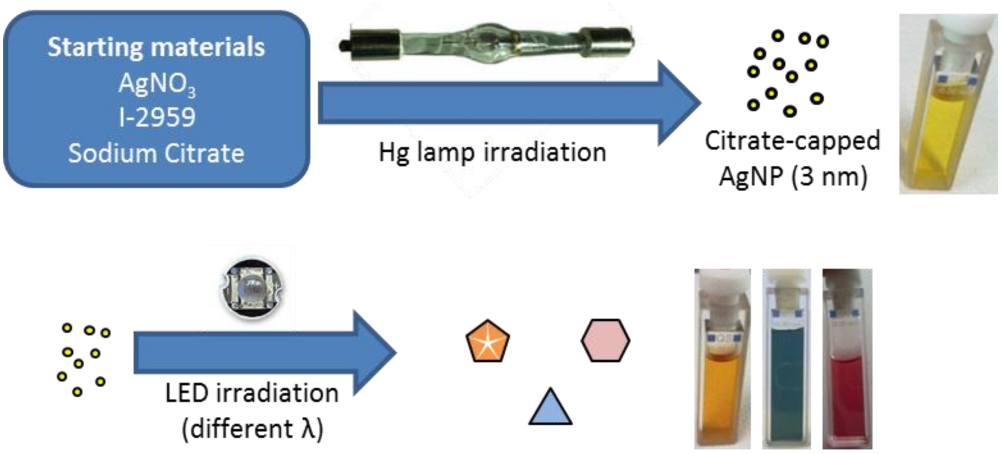

Figure 3.12. LED-light directed, seed-mediated growth of silver nanoparticles

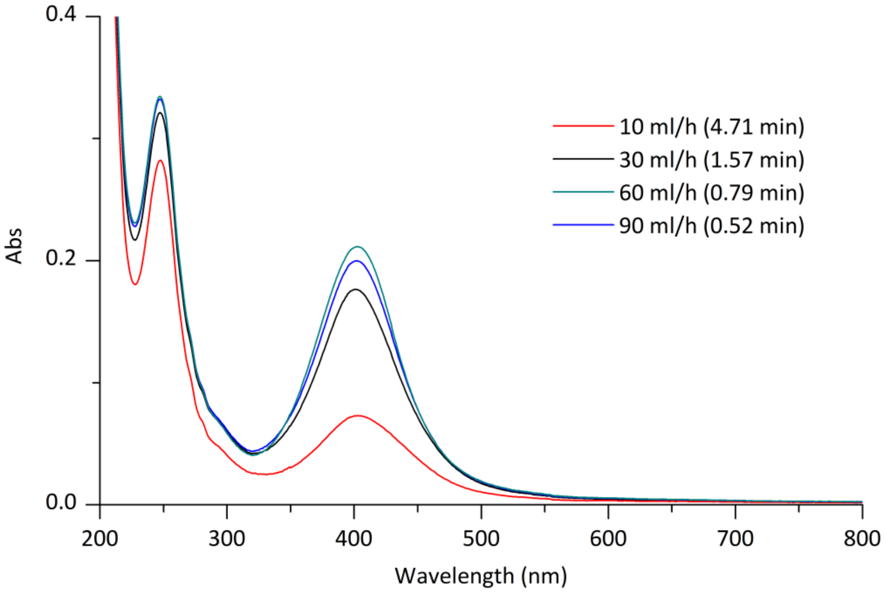

Figure 3.13. UV-Vis spectra of silver seed colloids produced at different flow rates

Deoxygenation of the mother solution before irradiation is necessary because molecular oxygen would easily quench the radicals generated by the Igracure photosensitizer. On the other hand, oxygen is necessary in the growth phase, as reported by Maillard.[90] Moreover, seed NPs do not display any significant absorption above 590 nm, so that long wavelength irradiation does not affect the conversion process. In the work by Stamplecoskie these two issues were addressed by performing the irradiation in an open vessel, so that oxygen could dissolve in the solution, and by exposing the seeds to ambient light for several days, in order to allow for the formation of small amounts of anisotropic seeds, which constituted the base for further, long-wavelength driven growth.

In this case, a MFD, whose testing with a red ink is reported in figure 3.14, was used in order to optimally oxygenate the silver colloid during irradiation. Air bubbles were generated at a T-junction and flowed together with the colloid. A stainless steel tube had to be inserted in the outlet connection to reduce the turbulences generated by the periodical wetting of the hydrophobic PTFE tube by the aqueous solution, lest the bubbles regime became chaotic and lacked reproducibility over time.

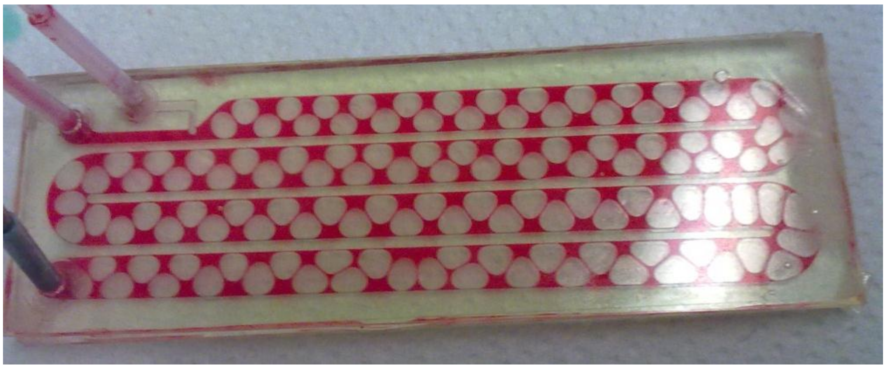

Figure 3.14. Testing of the MFD used for light-induced shape conversion of silver colloids.

Irradiation of the silver colloid in a 1 cm quartz cuvette with 455 nm (blue) LED light caused the spectral changes shown in figure 3.15, over the course of 5 hours. The stronger band arising at 483 nm is due to the in-plane dipole of decahedral-shaped AgNP, while the weaker bands at 335 and 413 nm are due to their out-of-plane and in-plane quadrupole plasmon modes, respectively.[89] The same treatment was carried out in microfluidic conditions, in the device pictured above (estimated total volume: 430 µl), with a total flow rate (air + silver colloid) of 400 µl/h. The UV-Vis spectrum of the resulting solution was recorded in a 1 mm glass cuvette and is superimposed to the previous one (broken line in figure 3.15) along with a TEM micrograph of the nanoparticles.

Carrying out the irradiation with a reduced sample thickness undoubtedly helped to achieve a more uniform and intense illumination on the sample, improving the rate of the process. The height of the channel in the MFD was roughly 300 µm, less than 1/30 that of the cuvette, meaning that the the light reaching the deepest liquid layer was much more intense. Besides an increased process rate, another interesting feature of the absorption spectra is the reduced formation of anisotropic NPs upon microflui dic treatment that can be assessed by considering the absorbance between 600 and 700 nm.

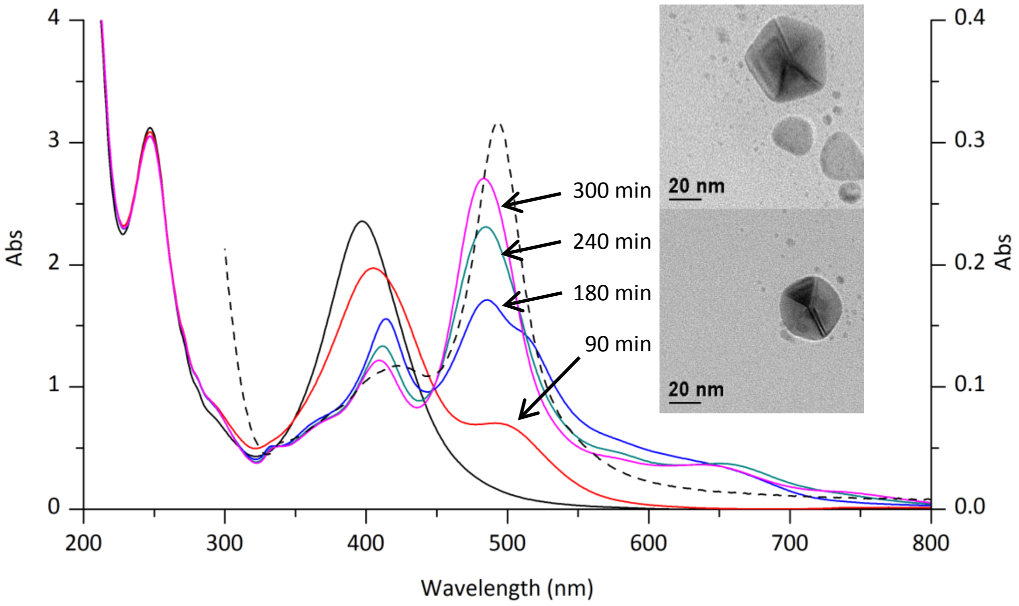

Figure 3.15. Spectral change upon irradiation at 455 nm. Solid line spectra (left Y-axis) are for colloids treated in a 1 cm, open quartz cuvette; the broken line (right Y-axis) spectrum was collected in a 1 mm glass cuvette after flow treatment in microfluidic conditions. Insets: TEM micrograph of two decahedral nanoparticles.

When a 505 nm (cyan) wavelength was used to treat the sample, the spectral evolution was different than in the previous case. In Figure 3.16, the spectra recorded for irradiation in a 1 cm cuvette (solid lines) over a 4 hours timespan and in the MFD (broken line) with the same flow rate as in the previous experiment can be appreciated. In this case the bands arising in the two experiments appear to be centered on a different wavelength.

The spectrum recorded upon treatment in the MFD, with an absorption maximum at 542 nm is actually in good agreement with that reported by Stamplecoskie, and suggests the formation of hexagonal nanoplates (which, alas, could not be observed via TEM due to technical difficulties). Notwithstanding the difference in the absorption spectra, the absorbance value at high wavelengths is, again, lower for the sample treated in microfluidic conditions, indicating a more homogeneous system shape-wise. The same considerations as in the case of the 455 nm irradiation can also be made regarding the comparison between the rate of the microfluidic and batch process. Both processes appears to be slower than the former case, this could be expected, since the colloidal solution has an higher absorbance at 455 nm than at 505 nm, thus interacting more easily with the photons of the former wavelength.

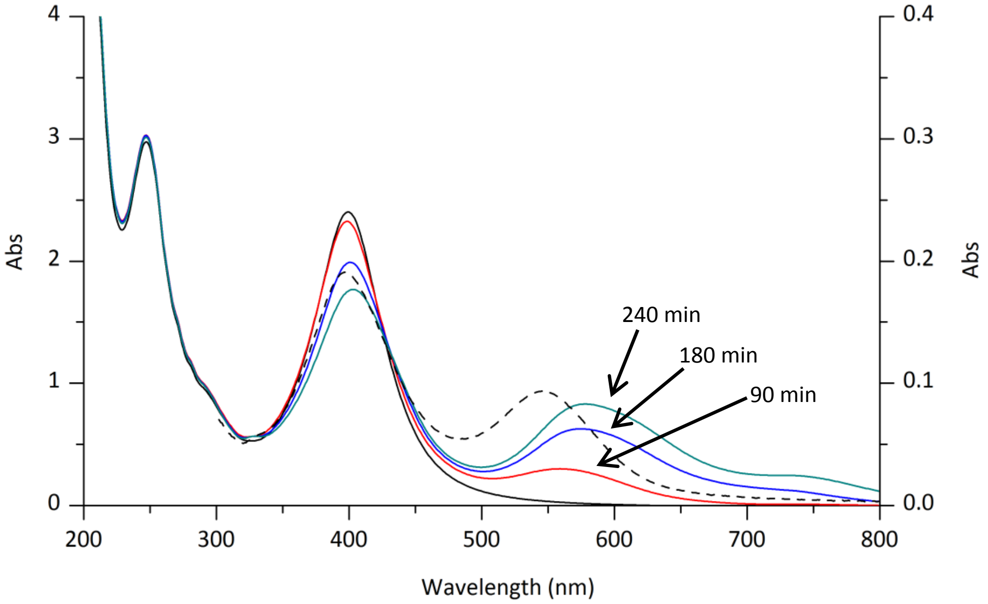

Figure 3.16. Spectral change upon irradiation at 505 nm. Solid line spectra (left Y-axis) are for colloids treated in a 1 cm, open quartz cuvette; the broken line (right Y-axis) spectrum was collected in a 1 mm glass cuvette after flow treatment in microfluidic conditions.

Indeed, the lack of photon absorption at higher wavelengths did not allow any evolution in the morphology of the AgNPs when irradiations at 590 nm (yellow) and 627 nm (red) were performed. In order to generate the anisotropic particles necessary for the growth at such wavelengths, a seed solution was first irradiated at 455 nm in the MFD for a short time (flow rate: 800 µl/h). To validate this approach, figure 3.17 shows the UV-Vis spectra of a seed solution (black solid line) which was irradiated at 627 nm with no noticeable change (black dotted line). The same colloid was then illuminated at 455 nm (blue solid line, with the spectral changes compatible with those already shown above) and then again at 627 nm (red solid line).

The band arising at 704 nm is due to the conversion to platelets, and can be ascribed to the longitudinal plasmon mode absorption, while the a weaker band at 330 nm that could be expected for the transversal plasmon absorption is not recognizable.[91] One isolated triangular nanoplate can be seen in the inset in figure 3.17 together with its selected area diffraction (SAD) pattern, displaying the typical [1,1,1] pattern for FCC crystals structures.

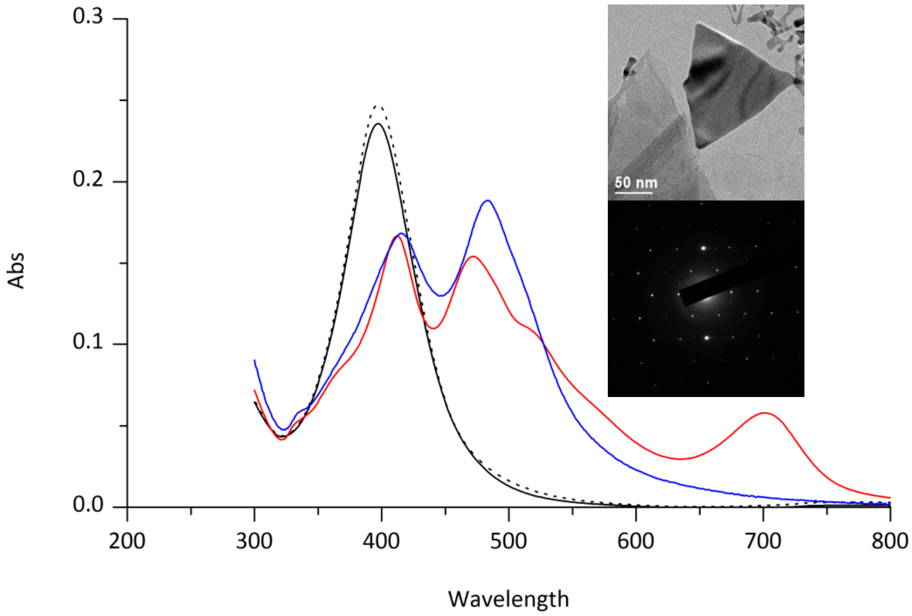

Figure 3.17. Spectral change upon consecutive irradiations in MFD of a seed solution (solid black line): first, at 627 nm (dotted black line), then at 455 nm (blue line) and again at 627 nm (red line). Spectra were collected in 1 mm glass cuvettes. Inset: TEM micrograph of the resulting colloid and relative SAD pattern.

According to the cited literature, both 590 nm and 627 nm irradiation should lead to the formation of platelets such as those observed above. In this case, though, an absorption band at 656 nm was observed upon illumination at 590 nm, as displayed in figure 3.18. As in the previous case, the seed colloid had to be exposed at 455 nm first, to observe any spectral evolution.

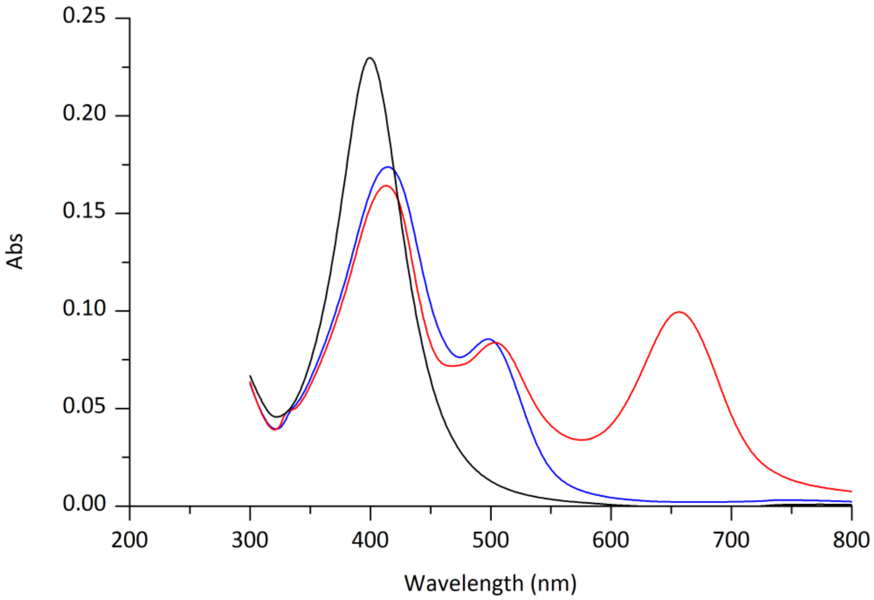

Figure 3.18. Spectral change upon consecutive irradiations in MFD of a seed solution (solid black line): first at 455 nm (blue line) and then at 590 nm (red line). Spectra were collected in 1 mm glass cuvettes.

Clearly, yellow and red lights did not have the same effect on the morphology of the sample. Moreover, in figure 3.17 the band at 492 nm, typical of silver decahedra, shrinks upon illumination, while in figure 3.18 the same band does not evolve over time and the band at 405 nm (seeds) appears to shrink slightly, instead. This difference has yet to be rationalized.

Conclusions and perspectives

This work shows how microfluidics can be exploited as an enabling technology for the optimized production of silver nanoparticles with controlled morphologies via a light-induced, seed-mediated growth approach. The use of a photoinitiator (Igracure 2959) as a reducing agent for initial nucleation of the nanoparticles allows for the whole process to be carried out at room temperature, using the mercury lamp of a standard photoreactor for initial seeding and then high-efficiency LED irradiation to direct the growth of the colloid. The use of LED light for activation of the Igracure photoinitiator in the initial step was not deemed convenient because i) LED sources operating in the UV-C range are very expensive (up to 200€/W) and ii) a quartz/fused silica MFD would have been necessary since soda lime glass is not transparent at such short wavelengths.

The comparison between the spectroscopic properties of the samples prepared in bulk-discontinuous conditions and those prepared with a custom-made MFD, showed that the latter presented a better conversion of the seeds in a reduced exposition time. Lower production of particles with anisotropic shapes were also observed in MFD conditions. Finally, the growth procedure for colloids requiring high-wavelength irradiation was rationalized, by substituting the traditional few-days-long exposure to ambient light with a short irradiation with 455 nm light in order to produce the needed morphological intermediates able to absorb photons with wavelength exceeding 590 nm.

Given the scientific interest surrounding silver nanoparticles and metal nanostructures in general, this research line will be further developed, by undertaking a more in-depth study on the growth process, in particular to explain the outcome of the experiment carried out with 590 nm irradiation (which differed from what was previously reported in literature). Besides the fundamental research on the growth process, silver nanoparticles will also be employed for surface enhanced Raman resonance spectroscopy (good preliminary results have already been achieved in this sense). Moreover, the same setup used for the nucleation of AgNPs, also proved to be useful for the synthesis of their gold and copper counterparts, opening up a wealth of possible applications.

Experimental

4-(2-hydroxyethoxy)phenyl-(2-hydroxy-2-propyl)ketone (I-2959), sodium citrate tribasic dihydrate and silver nitrate were purchased from Sigma-Aldrich. To one liter of deionized water, 34 mg (2×10^{-4} mol) of $AgNO_3$ were added under stirring together with 45 mg (2×10^{-4} mol, 1 eq) of I-2959 and 294 mg (10^{-3} mol, 5 eq) of sodium citrate. All colloids were prepared from this mother solution over the course of a few months.

Figure 3.19. PTFE tube coiled around a photoreactor, as used for the production of AgNP seeds.

The microfluidic reactor for the nucleation of silver seed consisted in a 4 m long PTFE tube with 0.5 mm internal diameter (total volume 785 µl), coiled around a photoreactor, as shown in figure 3.19. The tube was connected to a NE300 syringe pump by New Era Pumping Systems Inc. The optimization of the seeding procedure indicated a flow rate of 60 ml/h the best setting for this synthesis.

UV-Vis spectra were recorded on an Agilent Cary 5000 instrument in the 200 – 800 nm range when 1 cm quartz cuvettes were used or in the 300 – 800 nm range when glass cuvettes with a 1 mm optical path were used. Absorption spectra for all starting materials, as well as for the degradation products of I-2959 were recorded for reference and are reported in figure 3.20.

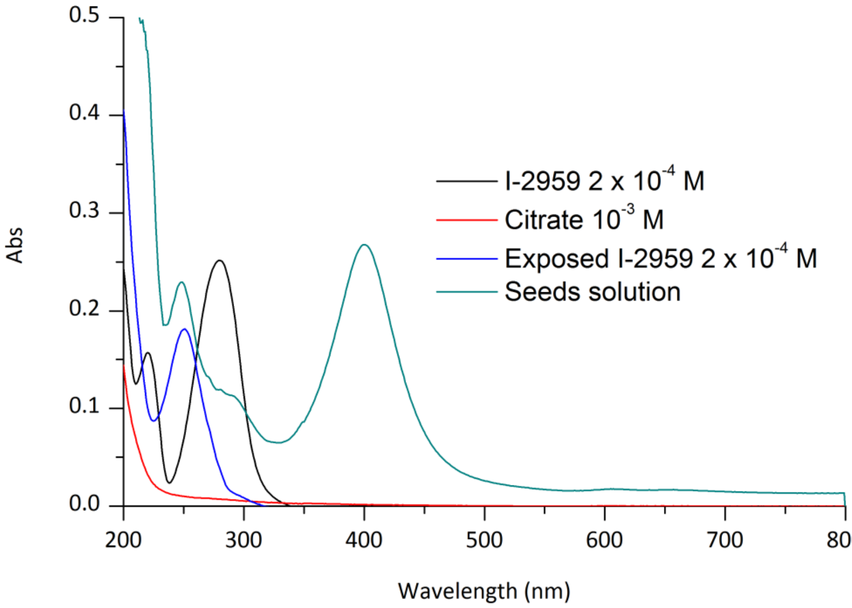

Figure 3.20. UV-Vis spectra of starting materials, I-2959 and sodium citrate, together with the spectra of degradation products of I-2959 and that of a silver seeds colloid.

For the LED-light induced microfluidic growth of AgNPs, the MFD displayed in figure 3.14 was fabricated by soft photolithographic means as described in chapter 2.4. The mask bearing the channel pattern is reported in figure 3.21. Silver seed colloid was injected in inlet A at 350 µl/h, while air entered the MFD from B, at 50 µl/h. Since air is compressible, bubbling did not start right away but an induction period of about 30 minutes was needed before observing a regular flow.

Figure 3.21. Soft photolithography mask used for the fabrication of the MFD pictured in figure 3.14. A is the inlet used for the silver colloid injection, while B was used to insufflate air for the oxygenation of the solution; C is the outlet.

During operation, the MFD was illuminated by 5 high power LEDs (C11A1 series, received from Roithner LaserTechnik) mounted on an aluminum heat dissipator. In this work, LEDs operating at 455, 505, 590 and 627 nm wavelengths were used, each with a 10 nm FWHM and an efficiency exceeding 90%.

Batch growth experiment were carried out with the same LED illumination system, by loading the seeds solution in a quartz cuvette with a 1 cm optical path length, which was stirred with a magnetic bar.

3.4 MFD for Electrochemical Impedance Spectroscopy

Electrochemical impedance spectroscopy (EIS) is not a new technique in chemistry, having been known to the electrochemistry community for more than a century.[92] It was initially applied to the determination of the double-layer capacitance[93] and has nowadays evolved to a powerful tool for the investigation of electrochemical reaction mechanisms,[94] in the characterization of technologically advanced materials such as conducting polymers[95] and in photo-electrochemistry with an increasing interest from the scientific community devoted to the development of dye-sensitized solar cells[96, 97].

EIS studies the response of the system to the application of a periodic difference of potential between two electrodes. Measurements are carried out over a range of frequencies and bring about information about the electrode-electrolyte interface, and the electrolyte bulk alike. In general, any system possessing energy storage and dissipation capabilities (including electrochemical cells and biological tissues) can be examined by EIS. The interpretation of EIS data remains one of the main issues of this application due to the simultaneous presence of faradic and non-faradic currents. Both these charge transport phenomena are indeed present, so that the data must be interpreted using accurate equivalent electrical circuits (EECs).[98] This, in turn, allow to identify the contribution of each fundamental electrochemical process, such as the transport of the reactive species in solution, their adsorption on the electrode surface or electrochemical and chemical reactions at the interface.[99] The use of EECs when interpreting heterogeneous data is a widely acknowledged method. Its application in the field of bioelectrodes, for example, allows to perform electrical measures on living cells.[100] In this approach, called “impedance network” the system is described as a circuit of connected impedances, whose values are determined by the electrical properties of the specific elements, such as density, conductivity and dielectric constant.

This work presents the fabrication of a low cost microfluidic chip with implemented electrodes to be used for EIS measurement. The MFD, pictured in figure 3.22, encompasses a single, straight channel that crosses two couples of gold electrodes on its path from the inlet to the outlet. It can be described with a variation over the EEC model developed by Randles,[101] illustrated in figure 3.23. Each electronic element in the EEC has a precise physical meaning:

R_e	Resistance of the electrodes.
R_{ct}	Resistance to charge transfer at the interface (for faradic processes).
R_m, C_m	Parameters correlated to the electrochemical characteristic of the bulk of the solution.

C_{dl} Capacitance of the dual layer at the electrode (according to Helmholtz model).

C_w Capacitance due to ion spillover from the electrode (Gouy-Chapman model)

Each of the electronic parameters therein reported has been studied by measuring the impedance as a function of the frequency of the applied alternated potential and the salinity of the solution flowing in its channel. It should be noted that in a EIS experiment, the EEC describes the whole measurement system (including the MFD) and is not limited to the electrochemical system being studied (in this case, the electrolyte solution). For this reason it is necessary to find the right model to describe the chip's electronic behavior prior to its use for any other experimental activity. Moreover, studying the electronic parameters of the MFD allows an estimation of the potentialities of this class of prototype chips.

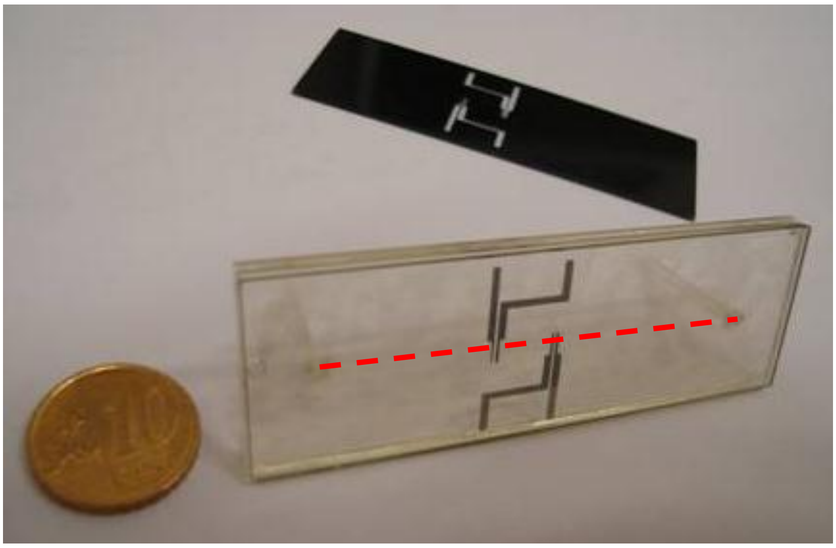

Figure 3.22. Microfluidic chip for EIS. The channel can hardly be seen in the image, because the biadhesive layer forming the body is transparent, so it has been highlighted by a red broken line.

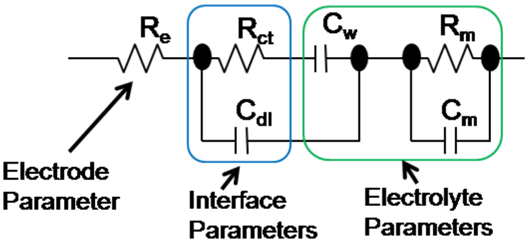

Figure 3.23. Equivalent electronic circuit for the MFD. Re is the resistance of the electrode; Rct is the charge transfer resistance and Cdl the capacity associated to the electrode-electrolyte dual layer; Cw describes the spillover of metal ions in the solution; Rm and Cm are the resistance and capacitance describing the electrolyte.

Results and discussion

The total impedance of the EEC shown in figure 3.23 can be written as a function of the impedances of its single elements which, in turn, depend on the concentration of sodium chloride in the electrolyte solution and the frequency of the current. The general expression for the impedance of the EEC considered in this work is:

$$Z = ZR_e + \frac{ZC_{dl}*(ZC_w+ZR_{ct})}{ZC_{dl}+(ZC_w+ZR_{ct})} + \frac{ZC_m*ZR_m}{ZC_m+ZR_m} \tag{3.9}$$

The impedance of resistors, Z_R, only has a real part (as a resistor on its own does not cause a phase change in the current), which equals the resistance itself. On the other hand, the impedance of a capacitor, Z_C, is a function of both the capacity C and the frequency of the current, ω:

$$Z_R = R \tag{3.10}$$

$$Z_C = \frac{1}{j\omega C} \tag{3.11}$$

where j is the imaginary unit. Experimental data are presented in figure 3.24 in form of Bode plots, where the two components of impedance (magnitude and phase) are plot against frequency.

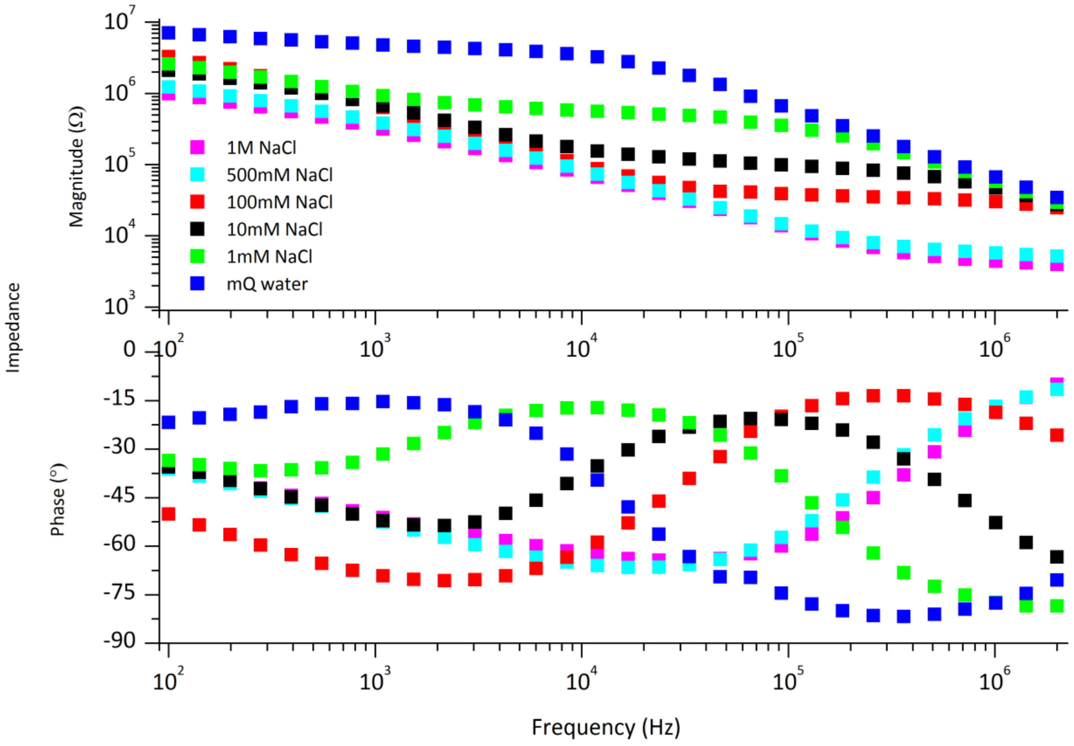

Figure 3.24. Bode plots of experimental data. The component of impedance are plot against frequency for every electrolyte solution.

Fitting each dataset with equation 3.9 yields the impedance value, and ultimately the resistance/capacity, of each element in the EEC as a function of the concentration of NaCl in the electrolyte solution. The resistance of the electrodes, and the associated impedance, ZR_e, do not depend on the frequency or the salinity of the electrolyte. It was thus convenient to determine it in the conditions with a lower contribution of the interface parameters, at [NaCl] = 1M.

The data are reported in table 3.2.

[NaCl] mM	**R_e × 10^3 Ω**	**R_{ct} × 10^4 Ω**	**C_{dl} × 10^{-12} F**	**C_w × 10^{-10} F**	**R_m × 10^5 Ω**	**C_m × 10^{-10} F**
0	4.3 ± 0.1	400 ± 1	2.50 ± 0.04	6 ± 1	21 ± 2	1.3 ± 0.2
1	4.3 ± 0.1	54 ± 1	2.89 ± 0.07	13 ± 2	12.9 ± 0.9	2.8 ± 0.2
10	4.3 ± 0.1	10.1 ± 0.3	3.2 ± 0.2	13 ± 2	11.9 ± 0.8	2.0 ± 0.1
100	4.3 ± 0.1	4.1 ± 0.7	9 ± 2	17 ± 3	11 ± 2	2.7 ± 0.1
500	4.3 ± 0.1	6 ± 1	80 ± 10	22 ± 4	6.8 ± 0.6	3.8 ± 0.3
1000	4.3 ± 0.1	6.8 ± 0.6	199 ± 9	30 ± 3	5.8 ± 0.3	5.0 ± 0.3

Table 3.2. Calculated values of resistances and capacitances in the EEC, at varying sodium chloride concentrations.

In order to describe the dependency of the five non-constant elements on the concentration of sodium chloride, two empirical relationships were used, each based on three parameters a, b, c. For resistors

$$R = a[\mathrm{NaCl}]^b + c \tag{3.12}$$

and for capacitors

$$C = a[\mathrm{NaCl}]^2 + b[\mathrm{NaCl}] + c \tag{3.13}$$

the sets of values (a, b, c) were calculated by least square fitting of the data in table 3.2 and provide a complete electronic characterization of the system. They are reported in table 3.3, and the good values for the R^2 fitting parameters attests the soundness of the results.

R_{ct}	a	3.91 × 10^2	R^2	0.9968
	b	-1.03		
	c	5.18 × 10^4		
R_m	a	-9.18 × 10^5	R^2	0.9976
	b	2.32 × 10-1		
	c	1.48 × 10^6		
C_w	a	-3.46 × 10^{-10}	R^2	0.9998
	b	1.97 × 10^{-9}		
	c	1.36 × 10^{-9}		
C_{dl}	a	8.44 × 10^{-11}	R^2	0.998
	b	1.11 × 10^{-10}		
	c	2.43 × 10^{-12}		
C_m	a	-1.29 × 10^{-10}	R^2	0.9965
	b	4.21 × 10^{-10}		
	c	2.10 × 10^{-10}		

Table 3.3. Parametric description of the electronic elements in the EEC.

Conclusions

A low-cost prototype MFD was fabricated in a short time and used as a fluidic platform for EIS measurements. The values of the resistive and capacitive elements in the EEC were evaluated as a function of the frequency of the current and the concentration of sodium chloride in the electrolyte used for the experiments, resulting in a comprehensive electronic description of the system.

During the experimental work, the MFD performed extremely well for a device so simple, thus demonstrating a good potential for future applications. In particular, EIS being a non-destructive technique, this prototype chip would well fit in a modular microfluidic setup for the online analysis of solutions, with the potential for detecting analytes and microstructures alike.

Experimental

The microfluidic platform with implemented electrodes used in this work was rather simple, with a single, straight biadhesive microchannel sandwiched between a head (fabricated in NOA 81 as described in paragraph 2.4) and a glass slide where gold electrodes were sputtered (this process was also described in paragraph 2.5). For sake of brevity, only the masks used for the deposition of the electrodes and the pattern embossed by the cutting plotter are reported, in figure 3.25.

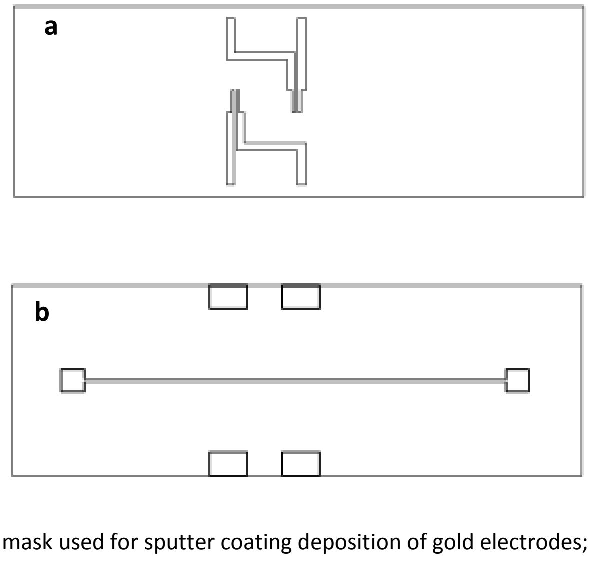

Figure 3.25. MFD design: a) mask used for sputter coating deposition of gold electrodes; b) pattern of the channel.

The rectangles cut at the edge of the device in 3.25b serve to bring an electrical contact out of the device, since the gold electrodes are very easily scratched. After sealing the device, those areas resulted empty and were filled with silver paint, which was allowed to dry overnight before using the chip.

All solutions for electrochemical experiments were prepared starting from deionized water (with a resistivity of 18.2 MΩ · cm); Sodium chloride was received from Sigma Aldrich and its concentration in the solutions for device characterization were 1mM, 10mM, 100mM, 500mM, 1M. Electrochemical impedance spectroscopy measurements were carried out in the 100 Hz – 100 KHz frequency range, with a signal amplitude of 25 mV and a 0 V bias voltage. A frequency response analyzer (Solartron 1260) coupled with an electrochemical interface module (Solartron 7081) was used to this end. A peristaltic pump (Gilson Minipuls Evolution) was used for flow handling. The instrument was driven by a custom LABVIEW 8.6 control and acquisition program, and data post-processing was carried out with MATLAB software.

A first experiment was carried out in a constant flow of milliQ water (0.1 µl/min) at room temperature. NaCl solutions at different concentrations were then used (0.1 µl/min, room temperature) and a 10 minutes rinse with 0.5 µl/min DI water was used to ensure the removal of salt residues from the channel in between measurements.

The geometry of the electrodes allowed to run different tests, with worker/reference electrodes at different distances. All electrode couples were found to work with similar results.

Acknowledgements

EIS measurements were carried out at the department of information engineering (DEI) by dott. Giorgio Marinaro, dott. Matteo Scaramuzza and Dr. Alessandro de Toni. The author wishes to thank them for their accurate work and their help in better understanding EIS techniques.

4. Flow synthesis of fullerene derivatives: kinetic studies

Following the discovery of fullerenes in 1985,[102] the chemistry of these fascinating molecules has been intensively investigated. In particular, the chemistry of [60]fullerene is now well established[103] and a large number of derivatives have been proposed for applications ranging from materials science[104, 105] to medicinal chemistry.[106] The production of new derivatives with tailored properties is central to the development of fullerene-based materials,[107, 108] and scientists have not passed up the opportunity to employ flow chemistry in order to optimize the yields of their reactions.[109]

This chapter presents the studies dealing with the kinetics of two of the most important reactions in fullerene chemistry: the cyclopropanation reaction with bromomalonates and the 1,3 dipolar cycloaddition of azomethine ylides. A batch *versus* flow approach was employed critically, and was aimed at the determination of rate constants for the aforementioned reaction (which, oddly, had never been reported before in literature) in order to describe the process and understand it thoroughly.

Kinetic data were recorded through the determination of the relative composition of the crude reaction mixture at different residence times. For experiments carried out in flow conditions, residence time was varied both by changing the length of the reaction coil at constant flow rate or *vice versa*. This is possible since, for MRs operating in steady state conditions, the residence time (rt) is both a function of the length of the channel l and of the flow rate Q according to equation 1.11. During an experiment, the composition of the reaction mixture at the outlet of the flow reactor is constant over time but it is not at equilibrium, so a quenching step is needed to stop the reaction. On the other hand, for batch experiments, the reaction mixture can be sampled and quenched multiple times during the course of the test.

4.1 Cyclopropanation to [60]fullerene

Among the most useful synthetic strategies in fullerene chemistry, the cyclopropanation reaction with bromomalonates producing methanofullerenes (scheme 4.1), is widely employed. This reaction, originally described by Bingel[110] and then further developed by the group of Hirsch[111] has been exploited over the years by several groups to make fullerenes more soluble,[112] combine their electronic and electrochemical properties with those of a wide variety of appended organic functionalities,[113] and to elucidate the principles that govern multiple additions to their carbon backbone.[114] The reactive bromomalonate intermediate (scheme 4.1) is typically produced *in situ* by reacting the corresponding malonate with a brominating agent, such as carbon tetrabromide, in the presence of a slight excess of a non-nucleophilic base (DBU, 1,8-diazabicyclo[5.4.0]undec-7-ene). After that, deprotonation of the bromomalonate, followed by intermolecular nucleophilic addition of the corresponding anion to [60]fullerene and intramolecular ring-closure, gives a methanofullerene monoadduct. However, since [60]fullerene possesses 30 reactive double bonds at corresponding 6,6-ring junctions, multiple cyclopropanations of the fullerene framework may be expected. The reaction can be driven selectively towards the monoadduct, or multiple adducts with a well-defined addition pattern.[115]

Herein reported is a kinetic study for the cyclopropanation of [60]fullerene that has been carried out under continuous flow conditions using 1,2-dichlorobenzene (ODCB) as a solvent. Quantitative data on the rate constants governing this very fast process have not been reported earlier, notwithstanding the vast amount of studies carried out on this class of carbon nanostructures. These constants have been assayed in a simple and straightforward way, by exploiting the steady state conditions in which the microfluidic setup operates,

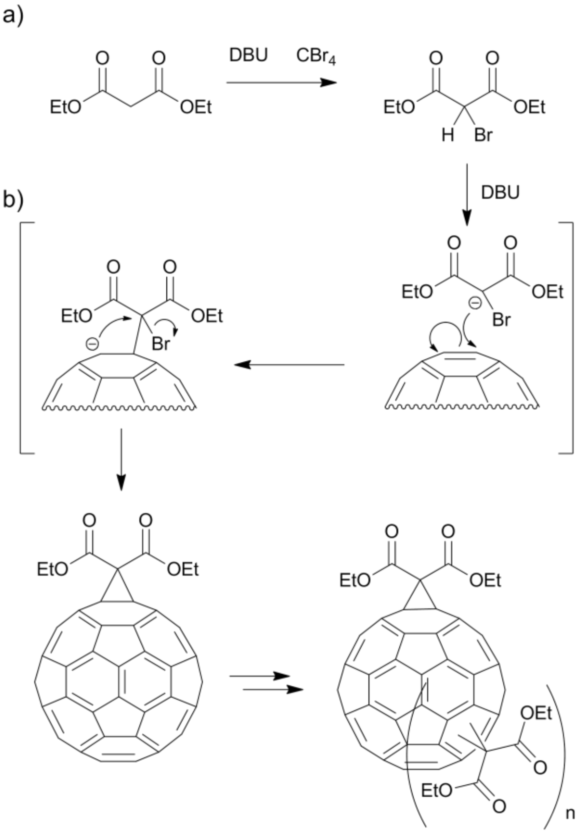

Scheme 4.1. Cyclopropanation of [60]fullerene with diethyl bromomalonate and the non-nucleophilic base DBU. a) formation of diethyl bromomalonate; b) intermolecular nucleophilic attack of the bromomalonate anion on the fullerene cage and intramolecular ring closure

and employed in a predictive manner to optimize the reagent monoaddition to the [60]fullerene cage while maintaining the best possible conversion.

Microfluidic setup

The [60]fullerene cyclopropanation under flow conditions was carried out within a microfluidic apparatus schematically depicted in figure 4.1. A 'Y'-shaped microreactor made of glass (150.332.2 chip type, by Micronit Microfluidics BV) or a commercial slit interdigital micromixer (with a mixing time in the order of tens of milliseconds) were used to combine the solution streams.

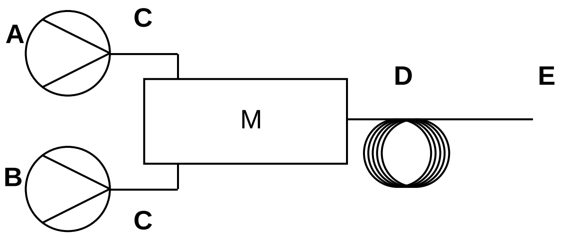

Figure 4.1. Experimental setup for the microfluidic production of methanofullerene derivatives (A, B = syringe pumps with the reagent mixtures; M = mixing element; C, D = coil of fused silica capillary, E = sample collector).

Continuous flow experiments were carried out using two approaches, depending on whether the diethyl bromomalonate (Et_2BrMal) intermediate was generated in situ within the mixing unit in the presence of [60]fullerene (Scheme 4.1a) or added externally (Scheme 4.1b). Both approaches were carried out under the two different mixing regimes outlined above. Quenching of the reaction was carried out right at the outlet of the MR by diluting with toluene.

Theoretical modeling of the kinetic process

Three kinetically pertinent steps were considered for modeling the process reported in Scheme 4.1. Step R1: Formation of the reactive intermediate Et_2BrMal, starting from CBr_4 and diethylmalonate (Et_2Mal) precursors. Step R2: Reaction of Et_2BrMal with [60]fullerene to give the monoadduct derivative P. Step R3: Reaction of P with Et_2BrMal. The latter process leads to formation of the bisadduct side products, S. Further reaction steps, generating higher poly adducts to [60]fullerene, would become relevant only at higher conversions, therefore they were not considered further in this study.

In summary:

R1: $CBr_4 + Et_2Mal \xrightarrow{DBU} Et_2BrMal$

R2: $C_{60} + Et_2BrMai \xrightarrow{DBU} P$

R3: $P + Et_2BrMai \xrightarrow{DBU} S$

The variation of concentration c_i of the i^{th} species in time (or space) equals the sum of its production and consumption rates:

$$\frac{dc_i}{dt} = \sum_n \nu_{i,n} r_n \tag{4.1}$$

where t is the residence time, r_n is the rate of the n^{th} reaction and $\nu_{i,n}$ is the stoichiometric coefficient of the i^{th} species in the n^{th} reaction, positive for products, negative for reagents and null for species not appearing in the reaction itself. In particular, for the three reaction steps R1, R2 and R3 the following expressions were used for r_n:

$$\begin{aligned} r_1 &= k_1[\mathrm{CBr_4}][\mathrm{Et_2Mal}][\mathrm{DBU}] \\ r_2 &= k_2[\mathrm{C_{60}}][\mathrm{Et_2BrMal}][\mathrm{DBU}] \\ r_3 &= k_3[\mathrm{P}][\mathrm{Et_2BrMal}][\mathrm{DBU}] \end{aligned} \tag{4.2}$$

The three rate constants, k_1, k_2 and k_3 were calculated by least-square-fitting of experimental data with the set of equations 4.1 and 4.2. The boundary conditions for the fitting procedure (i.e., starting concentration of [60]fullerene, DBU, and Et_2BrMal) differ within each experiment, but the parameters to be fit, k_n, appear in every equation set with the same physical meaning. Thus, it is convenient to fit every dataset separately, to check for the homogeneity of the results, and then refine the calculated values of the rate constants by using all the data from different experiments in a single fitting session. In this case, the procedure minimized the function E, defined as:

$$E = \sqrt{\left(\frac{\sum_{Exp}\sum_{Sp}\sum_{rt}\left(c^{exp}-c^{calc}\right)^2}{N}\right)} \tag{4.3}$$

where c^{exp} and c^{calc} refer to the experimental and calculated concentrations respectively and the three sums run over all reaction times (rt), species (Sp) and all experiments (Exp), for a total of N experimental points.

Results and discussion

The study started by carrying out the reaction under batch conditions, dissolving all reagents in ODCB in a round-bottomed flask at room temperature (see the experimental section for further details). Diethyl bromomalonate formed in situ and underwent the cyclopropanation to [60]fullerene according to the mechanism illustrated in scheme 4.1. Samples of the reaction mixture were taken at regular time intervals, quenched by dilution with toluene and analyzed by HPLC. Figure 4.2 reports a plot of the relative amounts of monoadduct (red squares), isomeric bis-adducts (blue squares), and unreacted [60]fullerene (black squares) *versus* time. Clearly, the reaction is quite fast, reaching a plateau after about 120 seconds. For this reason, the effectiveness and reproducibility of both sampling and quenching procedures were carefully verified, as reported in the experimental section.

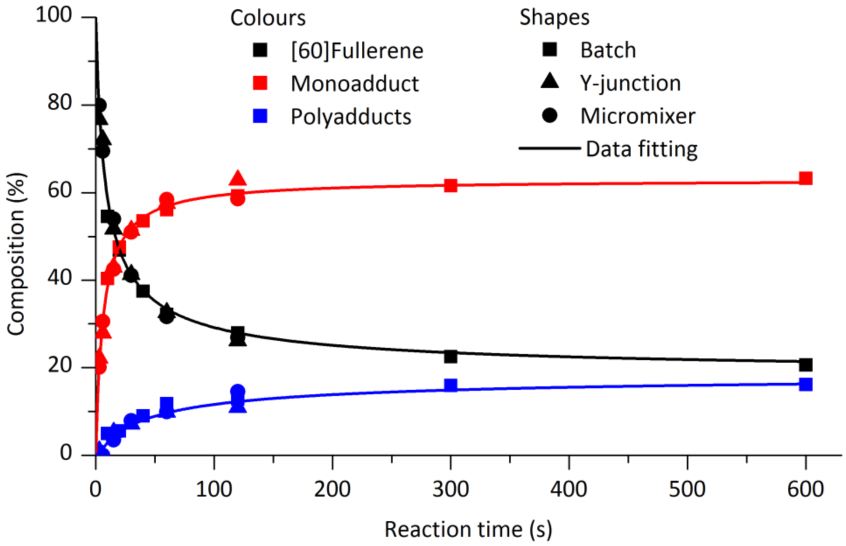

Figure 4.2. Results of the experiments involving the production of diethyl bromomalonate in situ. Data for batch and flow experiments are plotted together. (Squares) Data acquired in batch experiments; (triangles and circles) Data from experiments run under microfluidic conditions (Y-junction and micromixer MR respectively). Solid lines are the fitting curves according to the kinetic equations. Colors are associated with the species quantified in the experiments: (black) unreacted [60]fullerene; (red) monoaddition product; (blue) polyaddition side-products.

The reaction was then carried out under continuous flow conditions. To this end, the reagents were loaded into two different syringes. Because the reaction does not take place in the absence of a base, one syringe was loaded with a mixture of [60]fullerene, CBr_4, and diethylmalonate in ODCB, and the second was filled with a solution of DBU in ODCB. Two different mixing methods were considered. In the simplest case, a Y-junction was employed. Here, a strictly laminar flow is operative, thus the solution streams travel side-by-side and mixing occurs by diffusion only. As a more efficient mixing system, a slit interdigital micromixer was used, which speeds up liquid mixing by a combination of multi-lamination and geometric focusing. The kinetics of the reaction were studied by changing the length of the fused silica reaction channel or the flow rate. By progressively shortening the tubing, it was possible to change the reaction time-frame in the range from 1–120 seconds. It should be noticed that the continuous flow regime sets a steady-state composition of the solution at the MR outlet. This fact allows multiple sampling to be performed as needed, enabling more reproducible and accurate data to be obtained. The possibility offered by this simple setup to perform kinetic experiments with times in the order of a few seconds without recurring to any stop-flow system, is also remarkable.

The results obtained from the studies of the reaction under the flow regime are also reported in figure 4.2 (as triangles and circles), superimposed on the batch-wise counterpart for easier comparison. It is evident that the data are substantially equivalent, regardless of the experimental setup. This qualitative result was confirmed by fitting the kinetic data; the good quality of the fit was confirmed by the value of the function E (1.1 %), which was calculated by using equation 4.3. An ideal mixing model fits the experimental data very well for all three setups, in spite of the intrinsic differences in their hydrodynamic properties. It should be noted that, although no data were collected for the diethyl bromomalonate intermediate Et_2BrMal, its concentration was provided by the solution of the system of kinetic equations 4.2. The values of the rate constants were evaluated as:

R1: $CBr_4 + Et_2Mal \xrightarrow{DBU} Et_2BrMal$ $k_1 = 3.13 \times 10^{2}$ L^2 mol^{-2} s^{-1}

R2: $C_{60} + Et_2BrMai \xrightarrow{DBU} P$ $k_2 = 2.10 \times 10^{4}$ L^2 mol^{-2} s^{-1}

R3: $P + Et_2BrMai \xrightarrow{DBU} S$ $k_3 = 5.23 \times 10^{3}$ L^2 mol^{-2} s^{-1}

k_1 is lower by two orders of magnitude than k_2 and k_3. Thus, the bromomalonate intermediate is limited throughout the length of the reactor, therefore setting a bottleneck for the reaction rate. As a consequence, R1 was identified as the rate-determining step of this process. Next, the selectivity of the process was considered in order to maximize the production of the mono-addition product P. In this multistep process, selectivity is both a function of the relative values of rate constants (k_2 and k_3) and of the degree of conversion. In particular, because the selectivity is expected to decrease as the reaction progresses, working at lower conversions may be convenient. However, it is not an easy task to stop a fast reaction at a desired conversion level, especially if it is carried out under batch conditions.

Flow conditions, on the other hand, ensure the so-called space-time equivalence, that is, the reaction time is a function of the length of the channel according to equation 1.11. Because this length can readily be varied, reaction times of fractions of a second can easily be handled.

Focusing on steps R2 and R3, the dependence of the selectivity on process parameters could be monitored. For this reason, a set of experiments was run, using commercial diethyl bromomalonate (Et_2BrMal) instead of producing it in situ; in this way, the bottleneck-step R1 was removed. Three experiments were run under microfluidic conditions, by employing a Y-junction reactor and different ratios of [C_{60}] to [Et_2BrMal] (1:1, 1:1.5, and 1:2). The reaction profiles for these experiments are reported in figure 4.3a–c. Furthermore, one experiment was run using the micromixer instead of the Y-junction to evaluate the effect of mixing on the reaction profile. In this case the experiment with a ratio of [C60] to [Et2BrMal] of 1:2 was chosen, because the reaction was faster and thus more likely to be affected by mixing issues; the results can be seen in figure 4.3d. The values of the rate constants, calculated for each of the datasets thus far presented are reported in table 4.1. In the first column the values calculated for the experiments with the bromomalonate intermediate produced in situ are reported. The following columns refer to the experiments with external addition of commercial intermediate in different amounts (1.0, 1.5, and 2.0 eq) with a Y-junction microfluidic chip. Finally, the last column reports the values of k_2 and k_3 calculated for the flow experiment with external addition of intermediate with the micromixer. The values of E (see equation 4.3) for the fitting are also reported in the last row.

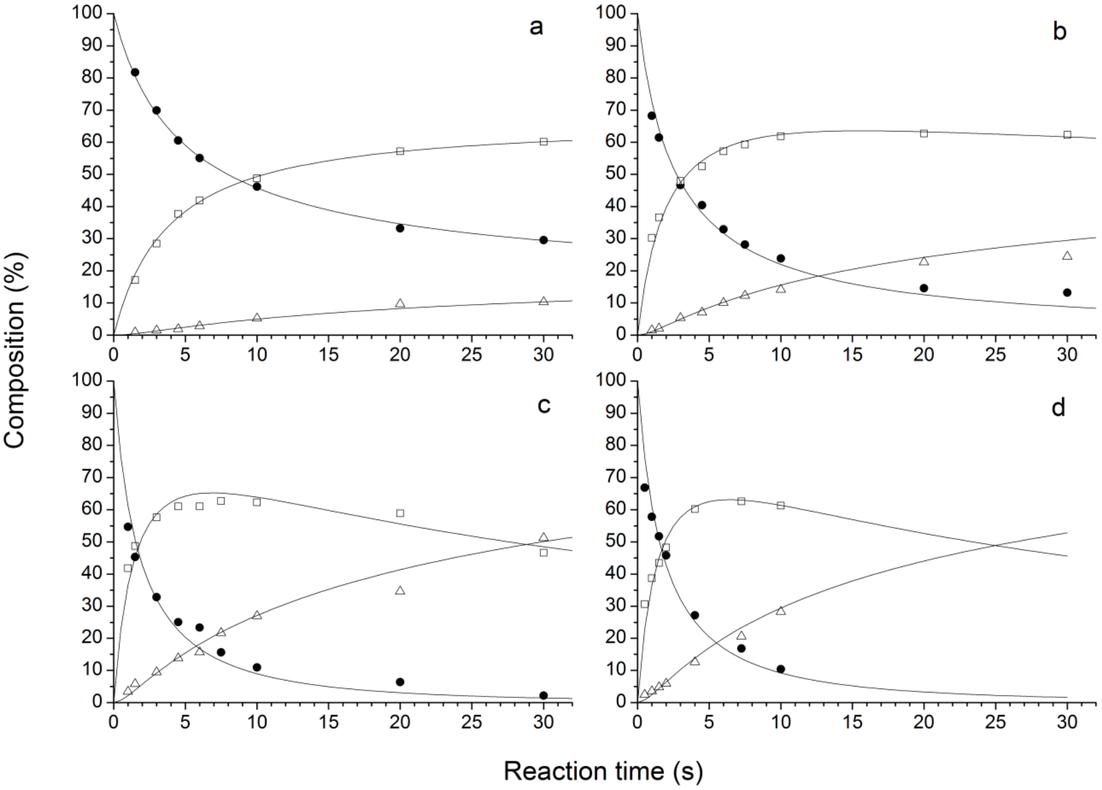

Figure 4.3. Results for the flow experiments with commercial diethyl bromomalonate. Circles, squares and triangles represent the observed concentrations of [60]fullerene, monoaddition, and polyaddition products, respectively. Experimental points and fitting curve (solid line) for reactions with (a) 1.0, (b) 1.5, and (c) 2.0 eq of diethyl bromomalonate in Y-junction microfluidic chips. (d) Data and fitting curve obtained with 2.0 eq of diethyl bromomalonate and micromixer.

	3-step process	1.0 eq. Y-mixer	1.5 eq. Y-mixer	2.0 eq. Y-mixer	2.0 eq. µ-mixer
k_1[a]	3.13×10^2	-	-	-	-
k_2[a]	2.11×10^4	2.44×10^4	2.38×10^4	2.10×10^4	2.13×10^4
k_3[a]	5.23×10^3	5.39×10^3	5.78×10^3	4.62×10^3	5.18×10^3
E[b]	1.11 %	0.78 %	1.53 %	2.59 %	2.30 %

[a] All values given in $L^2\ mol^{-2}\ s^{-1}$. [b] Calculated as per equation 4.3

Table 4.1 Calculated rate constants

The observed values of the constants k_2 and k_3 do not differ much from one experiment to another, and a comparison of the values of the error function suggest that mixing does not significantly hamper the productivity of the system. Finally, by simultaneously fitting all the data from all experiments, the values of the rate constants were further refined. The error associated with each constant was assessed as half the dispersion of the values of that constant calculated in the single experiments:

$k_1 = (3.1 \pm 0.3) \times 10^2\ L^2\ mol^{-2}\ s^{-1}$

$k_2 = (2.1 \pm 0.2) \times 10^4\ L^2\ mol^{-2}\ s^{-1}$

$k_3 = (5.2 \pm 0.6) \times 10^3\ L^2\ mol^{-2}\ s^{-1}$

Once all the parameters describing the system were evaluated, the model was used for predictive purposes. In particular, it was possible to calculate the selectivity *versus* conversion achieved by using commercial diethyl bromomalonate, which does not depend on the stoichiometry of the reaction (figure 4.3). Conversions of [60]fullerene ($Conv$) and selectivities (Sel) towards the monoadduct were calculated with the following equations:

$$Conv = 100 - C_{60} \qquad (4.3)$$

$$Sel = \frac{Mono}{Mono + Poly} \qquad (4.4)$$

where C_{60} is the percentage of unreacted fullerene observed in the mixture, $Mono$ and $Poly$ are the percentages (or concentrations) of P and S products, respectively. From this diagram, it can be deduced that, in order to work at a high level of selectivity (ca. 95 %), the payback is that lower conversions result (ca. 32% at best).

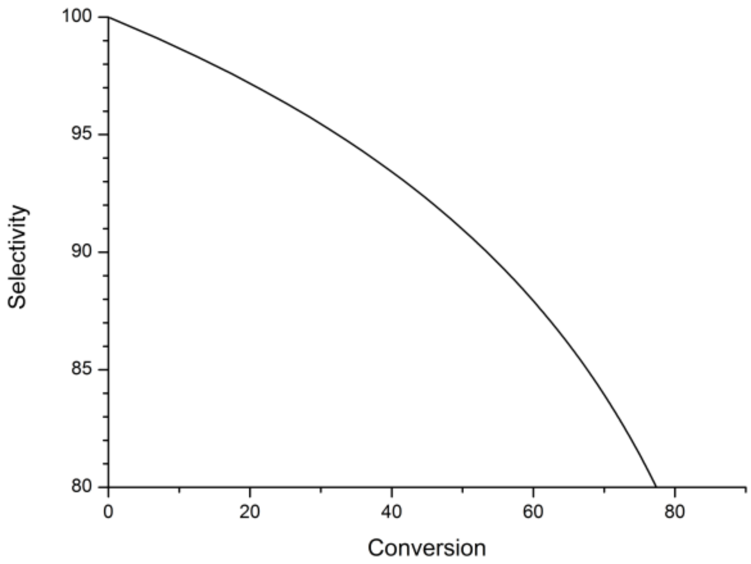

Figure 4.4. Selectivity *versus* conversion for the flow synthesis of a methanofullerene monoadduct.

Conclusions

This work reports a kinetic study of the cyclopropanation reaction of [60]fullerene with diethyl bromomalonate in a microfluidic reactor. The kinetic equations were used to determine the rate constants k_1, k_2, and k_3 for each step of the reaction by fitting experimental data collected in different mixing regimes. Because of the steady-state conditions along the length of the microchannels it was possible to sample the reaction mixture, even at short reaction times, and perform HPLC separation/analyses in a manner resembling a stop/quenched flow system with the addition of a chromatographic separation before the analysis. This result is general and may find application in the study of other reactions. The values of the rate constants allowed the rate-determining step for the cyclopropanation to be identified as the formation of the diethyl bromomalonate intermediate. It has been found that the rate constant for its formation was two orders of magnitude lower than those of the following steps, creating a bottleneck for the reaction. It can be noted that the microfluidic production of methanofullerenes, which are valuable intermediates in fullerene chemistry, possesses many advantages over the traditional methods in that: i) it is possible to achieve high selectivities by sacrificing conversion, to avoid lengthy separation procedures and recycling reagents, and ii) the process is continuous and the crude reaction mixture at the outlet has a very reproducible composition. Furthermore, both fluidic setups proposed in this work could be adapted for the production of methanofullerene derivatives on a large scale.

Experimental

[60]fullerene (99.5%) was purchased from Bucky-USA. Diethylmalonate (99%), diethyl bromomalonate (92%), tetrabromomethane (99%), 1,8-diazabicyclo[5.4.0]undec-7-ene (DBU, 98%) and anhydrous 1,2-dichlorobenzene (ODCB) (99%) were bought from Sigma-Aldrich and used as received. HPLC-grade toluene was used to quench the crude reaction samples prior to analysis. The 92% grade for diethyl bromomalonate was confirmed by ^{13}C-NMR spectroscopy (not reported here). The amounts of diethyl malonate and dibromo diethylmalonate were evaluated as 5% and 3%, respectively. Two different microfluidic chips were used for experiments under flow conditions: i) a glass Micronit Microfludics BV chip model R150.332.2, consisting of a Y-junction and a square-section ($\Sigma = 2.25 \times 10^{-2}$ mm^2) serpentine channel with total internal volumes of 6 µl and ii) a commercial slit interdigital micromixer with a characteristic mixing time of a few tens of milliseconds. KD-Scientific syringe pumps, model KDS-212, equipped with Hamilton 1 mL gastight syringes, mounting Swagelok peek fittings and Supelco fused silica GC capillary (øint = 250 µm), were used for fluid handling. HPLC analyses of reaction mixtures were performed on a Nacalai-Tesque Cosmosil Buckyprep column (250 × 5 mm) mounted on a Shimadzu LC-10AD pump system equipped with a Jasco 875-UV detector at 340 nm (eluent: toluene, flow = 1 ml/min). Raw data were corrected for the different molar extinction coefficient ε of the different species at 340 nm ([60]fullerene, $\varepsilon = 45535$ M^{-1} cm^{-1}, monoadduct, $\varepsilon = 32041$ M^{-1} cm^{-1}), UV-Vis absorption spectra are reported in figure 4.5. The extinction coefficient for polyadducts was assumed to be equal to that of the monoadduct.[116]

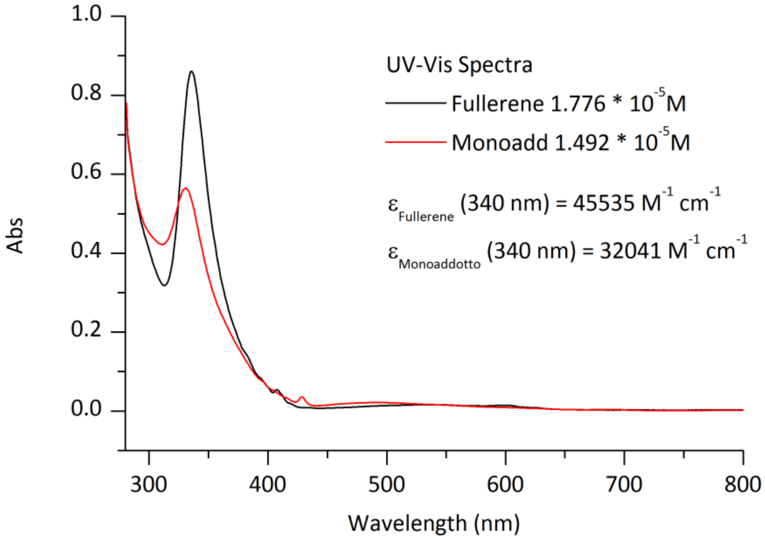

Figure 4.5. UV-Vis spectra for pristine [60]fullerene and the monoaddition product P.

Cyclopropanation under batchwise conditions: In a dry, 25 ml, two-necked round bottomed flask equipped with magnetic stirrer, [60]fullerene (100 mg, 0.139 mmol) and CBr_4 (46.1 mg, 0.139 mmol) were dissolved in 12 ml of dry ODCB under nitrogen atmosphere at room temperature. Diethyl malonate (22.3 mg, 0.139 mmol) was added to the mixture, followed by the base DBU (52.9 mg, 0.347 mmol). Aliquots of the crude mixture (100 µl) were taken at regular intervals with a micropipette, diluted into a vial with 10 ml of HPLC-grade toluene and analyzed by HPLC.

Cyclopropanation under flow conditions: Glass syringes were filled with the reagent solutions and connected to the mixing element M shown in figure 4.2 through fused silica capillaries. The concentrations of all reagents in the syringe were doubled with respect to the batch conditions, to achieve the same concentration after mixing. The residence time was calculated as the ratio between the total volume of the reactor and the actual flow rate according to equation 1.11. After the mixer, a fused silica capillary provided extra reaction volume. During the experiments, at least two reactor volumes were discarded before starting samples collection in order to reach a steady-state for the system. Sampling was carried out by placing the terminal silica capillary into a vial containing 4 ml of HPLC-grade toluene. Roughly 50-100 µl aliquots of reaction crude were collected for every sampling.

The syringe pumps were operated at a constant flow rate of 150 µl/min. Typically, the residence time was progressively reduced by cutting down the fused-silica capillary (i.e. a length of 3584 mm provided a 40 s reaction time). To achieve the shortest reaction times of 1.5 and 1 s, it was necessary to increase the flow rate to 300 and 450 µl/min respectively, with a capillary length of 31 mm.

Reproducibility of the analytical method: to test the sampling method for analytical reproducibility, the sampling procedure was repeated several times in the same conditions during the experiment employing 1.5 equivalents of commercial diethyl bromomalonate as a starting material and a reaction time of 1.5 s. This assay was performed in the worst possible conditions, at low conversion and low reaction time, meaning that the system was far from equilibrium and the driving force of the reaction was still strong. Owing to that, the quenching of the reaction at this stage was most difficult to achieve and any mistake in the sampling procedure on behalf of the operator would result in large experimental errors. The results are reported in table 4.2. The last sample was also injected in the HPLC column twice more, after allowing it to age for 10 and 20 minutes. This was done to assay the ability of the quenching technique to effectively stop the reaction. The results are reported in table 4.3.

Test number	C_{60} (%)	Monoadduct (%)	Polyadducts (%)
1	69.19	29.19	1.69
2	69.22	28.96	1.82
3	69.21	29.15	1.63
4	68.84	29.30	1.86
5	68.87	29.43	1.70
Mean	69.1	29.2	1.7
STD[a]	0.2	0.2	0.1

[a] Standard Deviation

Table 4.2 Evaluation of sampling procedure

Time before injection (min)	C_{60} (%)	Monoadduct (%)	Polyadducts (%)
0	68.87	29.43	1.70
10	68.24	289.36	2.40
20	68.16	29.76	2.08

Table 4.3 Evaluation of quenching procedure

The data in table 4.2 allow to evaluate the systematic error associated with the analytical method, as the double of the standard deviation. An error of ± 0,4 % is obtained. For comparison, a test on the volume dispensed by the syringes, that were used to pump the reagent solutions, showed a 2% error, so the sampling method appears to be precise and robust. On the other hand, repeating the HPLC analysis of the same quenched sample after extended periods of time did not show a trend toward higher conversion of the fullerene as all the data were within experimental error from the average. The composition change in the crude aliquots, in the timespan between sampling and analysis, was negligible. This statement can further be backed up considering that, while this test covered a time span of 20 minutes (sequence of three tests, each 10 minutes long) between the injection of the first and the last sample, each sample used for kinetic studies of flow syntheses was injected in less than 3 minutes from its collection.

Acknowledgements

The data presented in this paragraph were published in 2011 on the European Journal of Organic Chemistry.[117] The author of this thesis would like to thank the co-authors, in particular Dr. Daniela Dalle Nogare and Prof. Paolo Canu for the help with data treatment.

4.2 Addition of azomethine ylides to [60]fullerene

Another, widely applied functionalization method for the [60]fullerene molecule is the 1,3-dipolar cycloaddition of azomethine ylides to the fullerene backbone. The products of such reaction, fulleropyrrolidine derivatives, present a proline ring fused on a 6,6-ring junction of the fullerene spheroid.[118, 119] This family of molecules are important for materials chemistry, as they allow to tune the solubility and electronic properties of fullerene by choosing reactive azomethine ylides with suitable functional groups.[120, 121] Given the availability of different strategies for the generation of reactive azomethine ylides, starting from a variety of starting materials and the ease of functionalization of the reaction products, a wide range of fulleropyrrolidines have already become available. Two drawbacks of this reaction are its moderate yield and relatively long reaction time.

Among the routes for the generation of azomethine ylides, are thermal activation of aziridine and oxazolidinone derivatives. Another possibility, which this work focuses on, is shown in scheme 4.2, where an amino acid reacts with an aldehyde by heating. The 1,3 dipolar species forms with the release of one molecule of water, then further reacts with a double bond on the fullerene backbone, at a 6,6 ring junction. As in the case of the cyclopropanation described in the previous paragraph, 30 double bonds are available for functionalization on the carbon backbone, so multiple addition are typically observed.

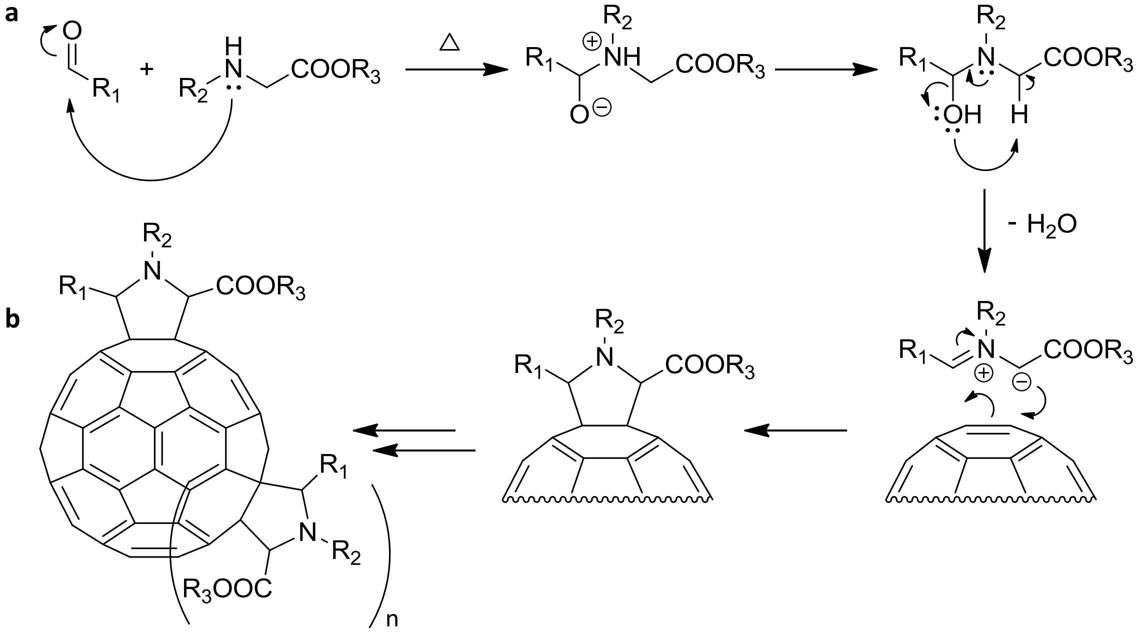

Scheme 4.2. 1,3-dipolar cycloaddition of an azomethine ylide generated in situ by a) reaction of an amino acid (in this case, a sarcosine ester) with an aldehyde to give an azomethine ylide. In b) the 1,3 dipole fuses with a 6,6 double bond on the fullerene cage to give mono- or poly-addition products.

This work reports a kinetic study on the addition of an azomethyne ylide, generated by the reaction of sarcosine ethyl ester and heptanaldehyde, to [60]fullerene, that has been carried out under both batch and flow conditions using a 3 : 1 mixture of ODCB : dimethylformamide (DMF) as a solvent. The effect of temperature on reaction rate has been assayed together with the effects of the residence time distribution on the composition of the reaction mixture in regard to mono- and poly-addition products. The evaluation of the rate constants for the process then allowed for the optimization of the reaction in order to achieve the best possible conversion towards the desired adduct.

Microfluidic setup

Given the relatively long reaction time, flow experiments were carried out in within a PTFE tube (0.5 mm inner diameter, 3 m length). Moreover, since the reaction does not proceed at room temperature, reagents were mixed prior to loading in the syringe pump and the setup did not need a mixing element, as shown in figure 4.6. An oil bath was used to provide heating; the PTFE tube was coiled and rested in the bath during operations.

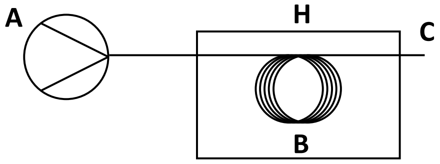

Figure 4.6. Experimental setup for the microfluidic production of fulleropyrrolidine derivatives (A = syringe pump with pre-mixed reagents; H = oil bath providing heating; D = coil of PTFE tube, C = sample collector).

Quenching of the reaction was carried out right at the outlet of the MR by diluting with ice-cold toluene.

Theoretical modeling of the kinetic process

The determination of the pertinent steps to be considered for the correct modeling of 1,3-dipolar cycloaddition process could was an important task in order to describe the process. Pre-emptive experiments were therefore carried out to assess the thermal stability of the starting materials. Indeed, in principle, the model that was probed presented 6 reactions:

$$\mathrm{SEE} \overset{\Delta}{\rightarrow} \mathrm{SEE}^*$$

$$\mathrm{HA} \overset{\Delta}{\rightarrow} \mathrm{HA}^*$$

$$\mathrm{SEE + HA} \overset{\Delta}{\rightarrow} \mathrm{Y}$$

$$\mathrm{Y} \overset{\Delta}{\rightarrow} \mathrm{Y}^*$$

$$\mathrm{C_{60} + Y} \rightarrow \mathrm{FP}$$

$$\mathrm{P + Y} \rightarrow \mathrm{PFP}$$

where the following acronyms were used for brevity: SEE – sarcosine ethyl ester; HA – heptanaldehyde; Y – azomethyne ylide; FP – fulleropyrrolidine monoadduct; PFP – fulleropyrrolidine polyadduct. Species denoted with "*" are considered inactivated. The first two reaction are generic thermal inactivation of the aldehyde and the amino acid, which were ruled out thanks to NMR studies (reported in the "results and discussion" paragraph). The following system was therefore considered in a way analogous to that of the previous kinetic study:

$$\begin{array}{llcll}
\mathrm{R1:} & \mathrm{SEE + HA} & \overset{\Delta}{\rightarrow} & \mathrm{Y} & r_1 = k_1[\mathrm{SEE}][\mathrm{HA}] \\
\mathrm{R2:} & \mathrm{C_{60} + Y} & \rightarrow & \mathrm{FP} & r_2 = k_2[\mathrm{C_{60}}][\mathrm{Y}] \\
\mathrm{R3:} & \mathrm{P + Y} & \rightarrow & \mathrm{PFP} & r_3 = k_3[\mathrm{FP}][\mathrm{Y}] \\
\mathrm{R4:} & \mathrm{Y} & \overset{\Delta}{\rightarrow} & \mathrm{Y}^* & r_3 = k_4[\mathrm{Y}]
\end{array} \tag{4.5}$$

(reaction rates r_n are reported on the right, with their respective rate constants k_n). The mass balances for the species taking part in the process are therefore:

$$\begin{gathered}
\frac{d[\mathrm{SEE}]}{dt} = \frac{d[\mathrm{HA}]}{dt} = -r_1 \\
\frac{d[\mathrm{Y}]}{dt} = +r_1 - r_2 - r_3 - r_4 \\
\frac{d[\mathrm{C_{60}}]}{dt} = -r_2 \\
\frac{d[\mathrm{FP}]}{dt} = +r_2 - r_3 \\
\frac{d[\mathrm{PFP}]}{dt} = +r_3
\end{gathered} \tag{4.6}$$

The rate constants, $k_1 \ldots k_4$ were calculated by least-square-fitting of experimental data with the set of equations 4.5 and 4.6. The boundary conditions for the fitting procedure (i.e., concentration of the starting materials at t = 0) were the same for all experiments and only the temperature was varied.

Results and discussion

The reaction was carried out by mixing the aldehyde (heptanaldehyde, HA) and the amino acid (sarcosine ethyl ester, SEE) in a 3 : 1 mixture of 1,2-dichlorobenzene (ODCB) and dimethylformamide (DMF), then heating the reaction mixture at different temperatures (110 °C, 125 °C and 150 °C). DMF was added to ODCB in order to solubilize the sarcosine derivative at room temperature, necessary condition in order to work in flow conditions.

Early NMR experiments were carried out to assess the interactions between solvents and starting materials at working temperature. SEE and HA were each loaded alone in a NMR tube, containing a 3 : 1 mixture of deuterated ODCB : DMF. The tubes were heated in an oil bath at 130 °C and ^{1}H-NMR spectra were recorded at regular intervals. For the aldehyde, ^{1}H-NMR spectra were also recorded at different temperatures to assay the possible formation of hydrated species, such as geminal diols. Only the spectra recorded before thermal treatment of the mixtures are reported here for brevity, in figure 4.7 and 4.8 for SEE and HA, respectively.

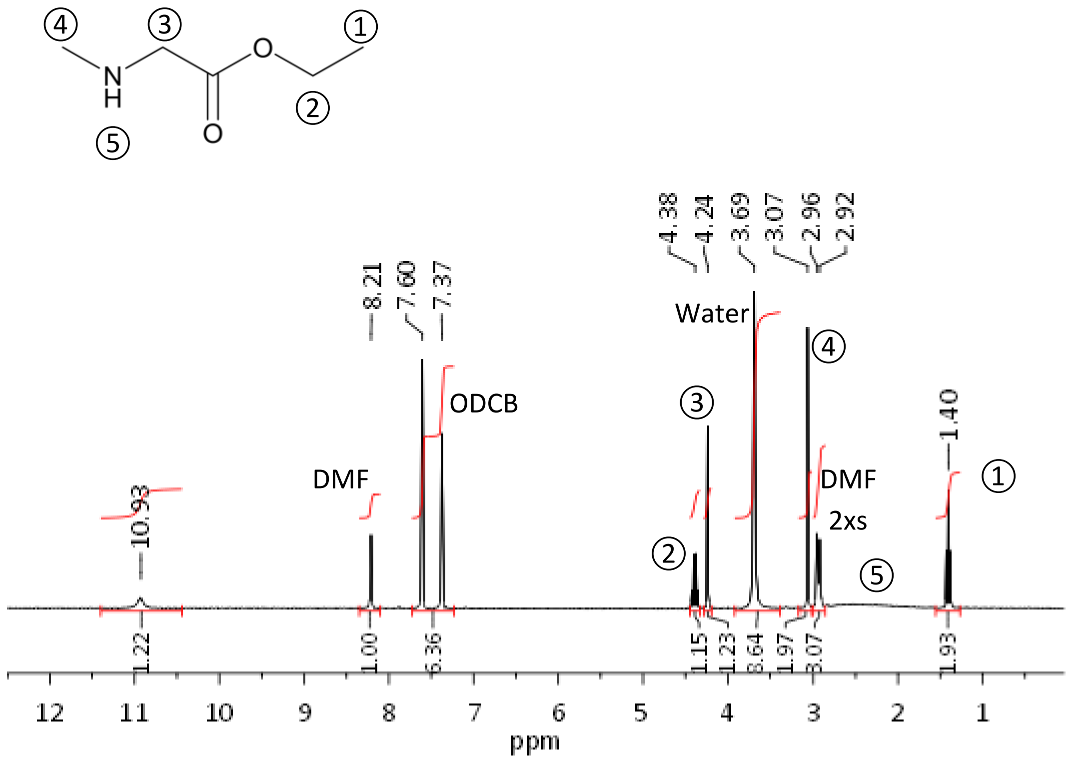

Figure 4.7. ^{1}H-NMR (300 MHz, 3 : 1 ODCB-d$_4$: DMF-d$_7$) of sarcosine ethyl ester hydrochloride.

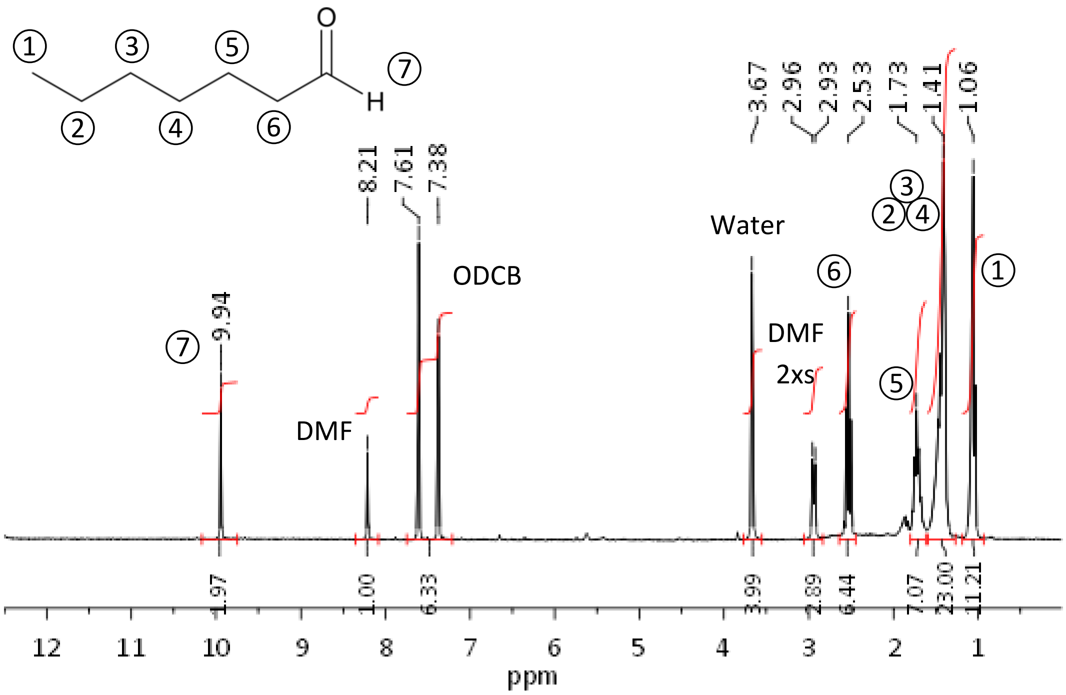

Figure 4. 8. ^{1}H-NMR (300 MHz, 3 : 1 ODCB-d_4 : DMF-d_7) of heptanaldehyde.

The peaks are assigned to the relative protons in the spectra; tables 4.4 and 4.5 report the evolution of the most notable integrals (or their ratios) in the description of the system. Signals from the solvents can be observed in the 7.0-8.5 ppm range for all the samples. The ratio between the integrated intensity of the peaks of the protons of ODCB (7.61 and 7.38 ppm) and DMF (8.21 ppm) is stable over time for both species (column 2 in both tables), so the solvent mixture can be considered stable after extended periods at 130 °C. An increase of the amount of water in the samples and the disappearance of HCl after a few minutes in the amino acid ethyl ester sample can also be observed.

For SEE, the ratio between the integrated intensity recorded for the various protons are (with reference to the figure) 1 : 2 : 3 : 4 = 3.00 : 1.78 : 1.91 : 3.07. These are close to the expected values 3.00 : 2.00 : 2.00 : 3.00. The signal from the formic proton of DMF can be used as an internal standard, since DMF is never added to the system and is stable over time (as pointed out above). Ultimately, the signals from all the protons of SEE appear to increase in integrated intensity, but the ratio between them does not vary appreciably, indicating that this starting material is stable and does not undergo thermal degradation.

t (min)	oDCB:DMF	①	③	①:③	Water	②	HCl
00	6.36	1.93	1.23	1.60	8.64	1.15	1.22
10	6.51	2.48	1.64	1.51	10.40	1.57	1.27
20	6.34	2.62	1.67	1.57	13.45	1.74	0.46
30	6.51	2.64	1.94	1.36	15.05	1.77	-

Table 4.4 ^{1}H-NMR experiment results for SEE

t (min)	oDCB:DMF	①	⑥	①:⑥	Water
00	6.33	11.21	6.44	1.74	3.99
10	6.40	11.75	7.17	1.64	4.85
20	6.48	10.73	6.55	1.64	5.38
30	6.67	13.33	8.18	1.63	7.82

Table 4.5 ^{1}H-NMR experiment results for HA

The ratio of the integrated intensity for the protons of HA are 1 + (2 + 3 + 4) : 5 : 6 : 7 = 3.00 : 6.16 : 1.89 : 1.72 : 0.53, so the only unexpected value is that of the aldehydic proton (expected: 1). This may be due to an hydration process on the carbonyl carbon, leading to a germinal diol in equilibrium with the aldehyde, but further experiments showed that no such species are formed, even by recording the spectrum at higher temperatures (up to 333 °K). The integrals ratio (signals indicated with 1 and 6 are easiest to consider in this respect) also keep constant after heating to 130 °C. Therefore, it is reasonable to assume that the aldehyde starting material can be considered stable *per se*.

The determination of concentration profiles was carried out in a way analogous to that of the previous kinetic study, by sampling the reaction crude at different times and characterizing its composition via HPLC chromatography both in batch and in flow experiments. Here, the stoichiometry of the reaction was not varied between the tests and the ratio between reagents' concentrations, [C_{60}] : [SEE] : [HA] was kept constant throughout, as 1 : 2 : 4. As pointed out earlier, the reagents were pre-mixed at room temperature before the reaction, which was starting upon heating, so their mixing was not an issue for the outcome of the process. The observed concentration profiles the batch experiments are plotted in figure 4.9 together with the fitting curves. Table 4.6 reports the calculated rate constants appearing in equation 4.5. Although it was not quantified in the chromatographic process, the concentration of the azomethyne ylide was calculated during the fitting procedure and is reported for reference. The fast initial production of the ylide highlight that, in this case, the generation of the reactive intermediate is not the rate determining step for the reaction.

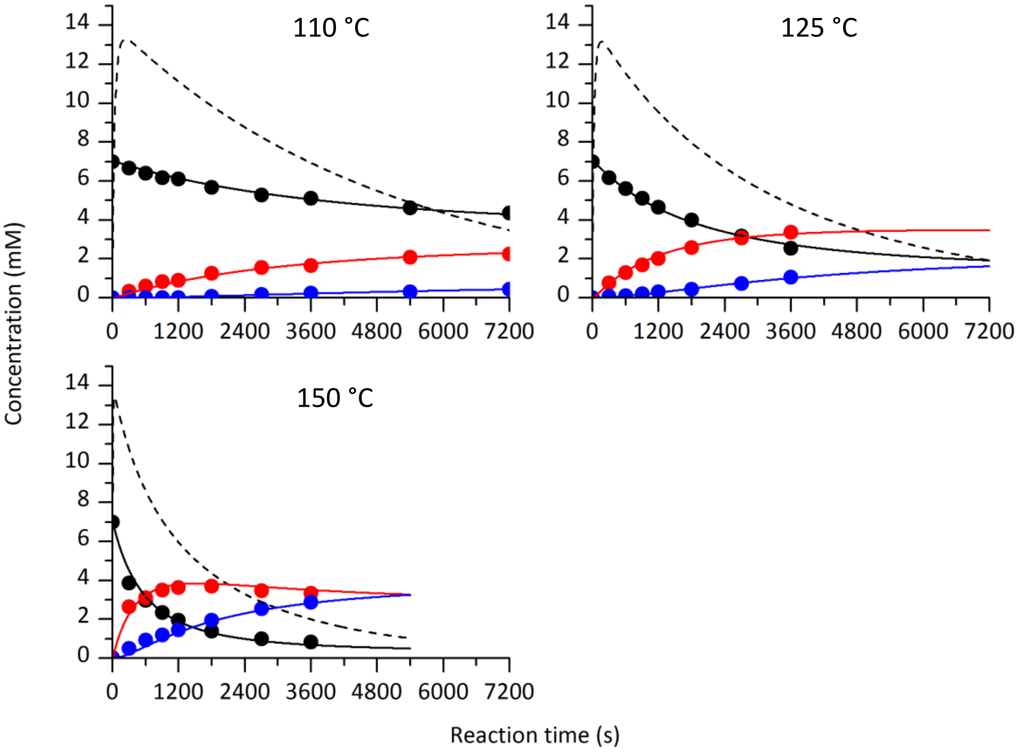

Figure 4.9. Concentration profiles for batch experiments. Black, blue and red data are for pristine [60]fullerene, monoaddition and polyaddition products, respectively. Fitting curves are also reported as solid lines.

T (°C)	k_1	k_2	k_3	k_4
110	1.09	0.94×10^{-2}	0.54×10^{-2}	1.23×10^{-4}
125	1.53	3.15×10^{-2}	1.59×10^{-2}	1.31×10^{-4}
150	7.44	12.20×10^{-2}	4.76×10^{-2}	1.48×10^{-4}

Table 4.6. Calculated rate constants, k_n at varying temperatures.

Rate constants k are functions of temperature T, according to Arrhenius equation

$$k = Ae^{-E_a/RT} \tag{4.7}$$

where A is a pre-exponential factor, R is the universal gas constant and E_a is the activation energy for the reaction. Equation 4.7 can be linearized as

$$ln(k) = ln(A) - \left(\frac{E_a}{R}\right)\frac{1}{T} \tag{4.8}$$

and the term $\frac{E_a}{R}$ can be computed by linear fitting, once $ln(k)$ is plotted against $\frac{1}{T}$. The results of the fit are reported in table 4.7 together with the linearity coefficient, which is a quality factor for the whole procedure. Indeed, reaction R_1 suffers from a sloppy R^2 factor, which is to be expected since a single reaction rate was used to describe a multistep process such as the formation of the reactive ylide. For the other reactions, a good (although not excellent) linearity coefficient is observed, and the value of the activation energy can provide interesting information about the reaction.

Reaction		E_a/R (°K)	$\ln(A)$	R^2
R1	$SEE + HA \overset{\Delta}{\rightarrow} Y$	$(8 \pm 2) \times 10^3$	20 ± 5	0.886
R2	$C_{60} + Y \rightarrow FP$	$(10.2 \pm 0.9) \times 10^3$	22 ± 2	0.986
R3	$P + Y \rightarrow PFP$	$(8.7 \pm 0.9) \times 10^3$	17 ± 2	0.975
R4	$Y \overset{\Delta}{\rightarrow} Y^*$	$(7.6 \pm 0.5) \times 10^2$	-7.0 ± 0.1	0.991

Table 4.6. Calculated rate constants, k_n at varying temperatures.

The difference in activation energies between the mono-addition and poly-addition reaction are not so large, the former being 17% higher than the latter. This indicates that the reactivity of the un-functionalized fullerene cage is not so different after the formation of one proline ring. This can be explained, considering that the fullerene cage is rather large with respect to the appended organic moieties, so only little steric hindrance limits a second addition. However, it should be noted that not all bis-adducts are identical as to the relative positions of the attached groups,[114] so the value reported here can only represent an average value. The last reaction only shows little dependence from temperature. This indicates that the reactive intermediate is probably not thermally deactivated, but follows a different inactivation path.

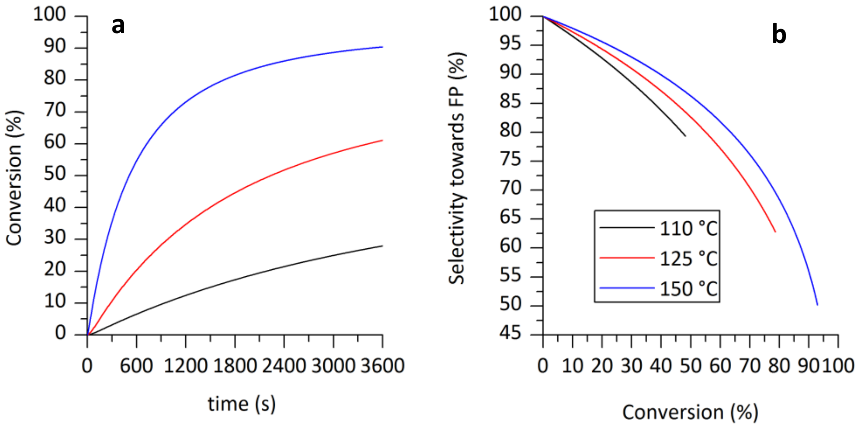

Figure 4.10. Conversion and Selectivity as a function of temperature. In a) conversion is plot against reaction time while in b) selectivity is plot against conversion.

Conversions and selectivities (calculated as per equations 4.3 and 4.4) for the process are displayed in figure 4.10 at different temperatures. Temperature affect both parameters, making the reaction faster, thus improving conversion, but also improving selectivity towards the product FP, since the reaction yielding the fulleropyrrolidine mono-adduct has an higher activation energy then the one generating poly-adducts.

Three kinetic profiles were also recorded for the flow process at 125 °C. Experimental data are plot (solid shapes) together with those collected in batchwise conditions (empty squares) in figure 4.11. While the reproducibility within the set of flow experiments appears good, the profiles differs from those displayed earlier, in that they seem to anticipate their batch counterparts. This is an effect of the residence time distribution, clearly outlined in figure 1.8: once am element of fluid in injected in the tube and flows diffusing according to the description given, it takes more than four average residence times for the 90% of its volume to flow out from the reactor. Indeed, the convolution of the RTD function $E(t)$ with the constant function describing the flow of [60]fullerene entering the tube, gives the age distribution of the flow elements exiting the reactor. The determination of a rate constant from these kinetic profiles is therefore not meaningful, unless the contributions of fluid elements with different residence times can be deconvoluted.

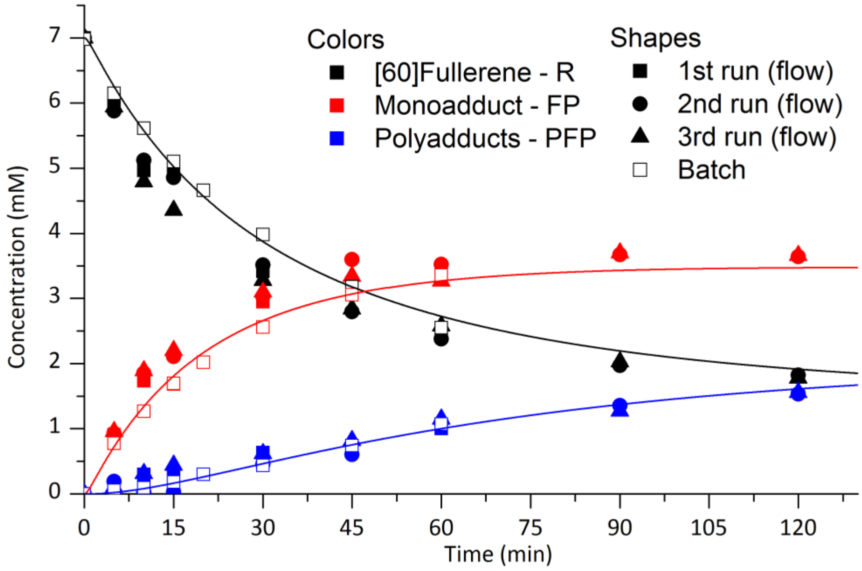

Figure 4.11. Kinetic profiles for flow experiments at 125 °C plotted together with the data collected in batch conditions. The solid line is the fitting function for batch experimental data.

Conclusions

This work reports a kinetic study of the 1,3-dipolar cycloaddition of an azomethyne ylide to [60]fullerene, using the ethyl ester of the amino acid sarcosine and heptanaldehyde as starting materials to generate the reactive azomethyne ylide *in situ*. ^{1}H-NMR experiment carried out on the starting materials helped to elucidate the mechanism by ruling out possible reaction and simplifying the mathematical model of the process.

The kinetic equations were used to determine the rate constants for each step of the reaction by fitting experimental concentration profiles collected in in batch conditions. Carrying out experiments at different temperatures allowed to study the activation energy of each reaction step thanks to the linearization of the Arrhenius' equation, and good linear coefficients were obtained for the results. An increase in both the reaction rate and the selectivity of the reaction have been observed and modeled with the increase of temperature.

Lastly, running the reaction in microfluidic conditions yields appreciable advantages neither in productiveness nor in ease of analysis, since i) mixing was not an issue for a slow reaction and ii) the broad RTD function brought about an artifact in the data collected in flow conditions for the long residence time. Further studies will be addressed at tackling this last issue, by careful modeling of the RTD function in order to provide an analytical description of its effects on the outcome of the process.

Experimental

[60]fullerene (99.5%) was purchased from Bucky-USA. Heptanaldehyde (95%), sarcosine ethyl ester hydrochloride (99%), anhydrous 1,2-dichlorobenzene (ODCB) (99%), anhydrous N,N-dimethylformamide (99.8%), 1,2-dichlorobenzene-d_4 (98% atom D) and N,N-dimethylformamide-d_7 (99.5 atom D) were bought from Sigma-Aldrich and used as received. HPLC-grade toluene was used to quench the crude reaction samples prior to analysis after cooling in water-ice bath. KD-Scientific syringe pumps, model KDS-212, equipped with Hamilton 5 mL gastight syringes, mounting Swagelok peek fittings and PTFE tubes ($ø_{int}$ = 500 µm), were used for fluid handling. HPLC analyses of reaction mixtures were performed on a Nacalai-Tesque Cosmosil Buckyprep column (250 × 5 mm) mounted on a Shimadzu LC-10AD pump system equipped with a Jasco 875-UV detector at 340 nm (eluent: toluene, flow = 1 ml/min).

Cycloadditions under batchwise conditions: In a dry, 25 ml, two-necked round bottomed flask equipped with magnetic stirrer, [60]fullerene (60.5 mg, 84 µmol), sarcosine ethyl ester hydrochloride (26.1 mg, 168 µmol, 2 eq) and heptanaldehyde (40.4 mg, 49.4 µl, 336 µmol, 4 eq) were dissolved in a mixture of 9 ml ODCB and 3 ml DMF under nitrogen atmosphere at room temperature. The reaction was started by heating the mixture under stirring in an oil bath at 110 °C, 125 °C and 150 °C, monitoring the temperature with a thermometer. Aliquots of the crude mixture (50 µl) were taken at regular intervals with a micropipette, diluted into a vial with 500 µl of ice-cold HPLC-grade toluene, and stored in an ice bath before being analyzed by HPLC.

Cycloadditions under flow conditions: The same reagents mixtures used for the batchwise experiment were loaded into glass syringes. The mean residence time was calculated as the ratio between the total volume of the reactor and the actual flow rate according to equation

1.11. During the experiments, at least two reactor volumes were discarded before starting samples collection in order to reach a steady-state for the system. Sampling was carried out by placing the end of the PTFE tube into a vial containing 1 ml of ice-cold HPLC-grade toluene. Roughly 50-100 µl aliquots of reaction crude were collected for every sampling and stored in an ice bath before being analyzed by HPLC. The residence time was progressively increased by reducing the flow rate of the syringe pump, rather than changing the length of the PTFE tube (3 m, for a total volume of 590 µl).

Acknowledgements

The author would like to thank Dr. Mauro Carraro and Prof. Marcella Bonchio for their help and guidance, especially in the planning of ^{1}H-NMR experiments.

5. Conclusions

Flow chemistry has yet to make it to every lab and course of study. At this moment it lacks *tradition*: it is simply not considered as a synthetic tool for lab-scale applications in the academia, because the generation of chemists on the field today has not been exposed to it. However, commercial flow apparatuses for chemical applications are reaching the market in growing numbers and it is widely accepted that the possibilities they offer are going to impact the way chemists think about their reactions. During this thesis, fast prototyping techniques for the fabrication of custom MFDs have been developed as a quick and low cost way to understand the true possibilities and drawbacks offered by this technology.

These protocols have been thoroughly described in chapter 2, to allow for the best possible reproducibility on behalf of the reader. They represent an important inheritance for the research group where my internship took place. Soft photolithography on thiol-ene resins was employed as the chief technique to transfer any pattern to a layer of photocurable resin and thus fabricate both the microstructured devices and their interfacing with the external world. Interesting alternatives were also exploited for the fabrication of the channel networks, especially by employing a cutting plotter to draw the desired patterns on low cost materials such as adhesive tapes and Parafilm M laboratory films. The quality of the prototypes produced by this low cost method was sometimes stunning. Different techniques were borrowed from other fields for the fabrication of electrodes, in order to broaden the MFDs' possible field of application.

Being “forced” to *think microfluidics* for three years, even in those situation where it was not necessarily the best option, I developed some sensitivity towards microfluidic applications, so that every device presented in chapter 3 highlights different ways in which MFDs can be used to solve chemical problems.

Safety issues of chemical processes generating dangerous intermediates were exemplified in the parallel synthesis of diazo dyes (paragraph 3.1). Not only could the diazonium salt intermediate (a potential explosive) be produced *in situ* at room temperature, rather than at 0 °C; it was also used in matter of seconds for the following coupling reaction and its holdup was way below 1 mmol, so that the danger posed by explosion was greatly mitigated. Besides an increased safety, the device demonstrated excellent multiplexing capabilities, in that it could run two syntheses of different dyes at the same time.

The microfluidic approach to photochemistry described in paragraph 3.2 allowed to increase the degree of control on the morphology of silver nanoparticles. Highly efficient LED illumination was used to direct the Ostwald ripening phenomena in citrate-capped silver colloids. In that case, the geometry of the microchannel played a fundamental role, since the reduced thickness of the suspension flowing in the conduit made for an extremely uniform illumination of the sample. Comparison between samples produced in the MFD with those from a traditional synthesis showed an increase in reaction rate as well as a decrease in the formation of anisotropic particles.

Thanks to the so-called *space-time equivalence*, a MFD interfaced with a spectrophotometer could be used to monitor in real time the dyeing process of thin layers of porous titanium dioxide – a process of fundamental importance for manufacturing dye sensitized solar cells – and fit the data with simple models, since the concentration of the dyes in the “dyeing bath” were constants. This allowed to collect large amount of data in a short time, that were used to better understand the dyeing process in paragraph 3.3.

On the whole, microfluidics has played the role of an *enabling technology*, or a set of tools that enables tasks to be carried out in *new* ways. In the last chapter, the kinetics of two important reactions involving the [60]fullerene carbon backbone were assayed. The first (cyclopropanation) is a “fast” reaction, that can be carried out in a few seconds, while the second (1,3-dipolar cycloaddition) is a hours-long process. In neither case the mere transposition of the batch synthesis into the flow regime has paid off in terms of yield. Moreover, microfluidic conditions complicated data treatment for the calculation of rate constants in the case of the slower process, because of the broad residence time distribution in the crude mixture at the outlet. On the contrary, a batch experiment for the determination of the concentration profiles of the cyclopropanation reaction would simply not have been feasible and it was microfluidics that allowed the fast process to be monitored. It should also be said that, for both reactions, a process could be envisioned where conversion could be traded for selectivity by carefully setting the reaction time. For fast reactions, such a deed is only feasible in flow conditions.

6. Bibliography

1. Terry, S.C., J.H. Jerman, and J.B. Angell, *A gas chromatographic air analyzer fabricated on a silicon wafer.* IEEE Trans. Electron Devices, 1979. **ED-26**(12): p. 1880-1886.
2. Manz, A., N. Graber, and H.M. Widmer, *Miniaturized total chemical analysis systems: A novel concept for chemical sensing.* Sensors and Actuators B: Chemical, 1990. **1**(1-6): p. 244-248.
3. deMello, A.J. and R.C.R. Wootton, *Miniaturization: Chemistry at the crossroads.* Nat Chem, 2009. **1**(1): p. 28-29.
4. Martinez, A.W., et al., *Simple Telemedicine for Developing Regions: Camera Phones and Paper-Based Microfluidic Devices for Real-Time, Off-Site Diagnosis.* Analytical Chemistry, 2008. **80**(10): p. 3699-3707.
5. Zheng, B., L.S. Roach, and R.F. Ismagilov, *Screening of Protein Crystallization Conditions on a Microfluidic Chip Using Nanoliter-Size Droplets.* Journal of the American Chemical Society, 2003. **125**(37): p. 11170-11171.
6. Baxendale, I.R., et al., *A flow process for the multi-step synthesis of the alkaloid natural product oxomaritidine: a new paradigm for molecular assembly.* Chemical Communications, 2006(24): p. 2566-2568.
7. *Contents.* Chemical Society Reviews, 2010. **39**(3): p. 891-898.
8. *Journal of Flow Chemistry - First Issue*. 2010; Available from: http://www.akademiai.com/content/122156/?v=editorial.
9. Valera, F.E., et al., *The Flow's the Thing...Or Is It? Assessing the Merits of Homogeneous Reactions in Flask and Flow.* Angewandte Chemie International Edition, 2010. **49**(14): p. 2478-2485.
10. *Vapourtec Flow Chemistry Equipment Website*. Available from: http://www.vapourtec.co.uk/.
11. *Corning Low Flow Reactor Brochure*. Available from: http://www.corning.com/WorkArea/showcontent.aspx?id=30831.
12. Rossi, E., P. Woehl, and M. Maggini, *Scalable in Situ Diazomethane Generation in Continuous-Flow Reactors.* Organic Process Research & Development, 2011.
13. Theberge, A.B., et al., *Microdroplets in Microfluidics: An Evolving Platform for Discoveries in Chemistry and Biology.* Angewandte Chemie International Edition, 2010. **49**(34): p. 5846-5868.
14. *Navier-Stokes Equation problem*; Available from: http://www.claymath.org/millennium/Navier-Stokes_Equations/.
15. Goldstein, S., *Fluid Mechanics in the First Half of this Century.* Annual Review of Fluid Mechanics, 1969. **1**(1): p. 1-29.
16. Neto, C., et al., *Boundary slip in Newtonian liquids: a review of experimental studies.* Reports on Progress in Physics, 2005. **68**(12): p. 2859.
17. Lauga, E., M.P. Brenner, and H.A. Stone, *The no-slip boundary condition.*, in *Handbook of Experimental Fluid Dynamics*, Springer, Editor. 2007.
18. Günther, M., et al., *Characterisation of residence time and residence time distribution in chip reactors with modular arrangements by integrated optical detection.* Chemical Engineering Journal, 2004. **101**(1–3): p. 373-378.
19. deMello, A.J., *Control and detection of chemical reactions in microfluidic systems.* Nature, 2006. **442**(7101): p. 394-402.
20. Atencia, J. and D.J. Beebe, *Controlled microfluidic interfaces.* Nature, 2005. **437**(7059): p. 648-655.
21. Johnson, T.J., D. Ross, and L.E. Locascio, *Rapid Microfluidic Mixing.* Analytical Chemistry, 2001. **74**(1): p. 45-51.

22. Schwalbe, T., et al., *Novel Innovation Systems for a Cellular Approach to Continuous Process Chemistry from Discovery to Market.* Organic Process Research & Development, 2004. **8**(3): p. 440-454.
23. Ducry, L. and D.M. Roberge, *Controlled Autocatalytic Nitration of Phenol in a Microreactor.* Angewandte Chemie, 2005. **117**(48): p. 8186-8189.
24. Brocklehurst, C.E., H. Lehmann, and L. La Vecchia, *Nitration Chemistry in Continuous Flow using Fuming Nitric Acid in a Commercially Available Flow Reactor.* Organic Process Research & Development, 2011. **15**(6): p. 1447-1453.
25. Löwe, H., V. Hessel, and A. Mueller, *Microreactors. Prospects already achieved and possible misuse.* Pure and Applied Chemistry, 2002. **74**(12): p. 2271-2276.
26. de Mas, N., et al., *Microfabricated Multiphase Reactors for the Selective Direct Fluorination of Aromatics.* Industrial & Engineering Chemistry Research, 2003. **42**(4): p. 698-710.
27. Xia, Y. and G.M. Whitesides, *Soft Lithography.* Angewandte Chemie International Edition, 1998. **37**(5): p. 550-575.
28. Wootton, R.C.R. and A.J. deMello, *Microfluidics: Exploiting elephants in the room.* Nature, 2010. **464**(7290): p. 839-840.
29. D.C. *SYLGARD® 184 SILICONE ELASTOMER KIT*; Available from: http://www.dowcorning.com/applications/search/default.aspx?R=131EN.
30. McDonald, J.C. and G.M. Whitesides, *Poly(dimethylsiloxane) as a Material for Fabricating Microfluidic Devices.* Accounts of Chemical Research, 2002. **35**(7): p. 491-499.
31. Gelorme, J.D., R.J. Cox, and S.A.R. Gurierrez, *Photoresist composition and printed circuit boards and packages made therewith*. 1989, International Business Machines Corporation (Armonk, NY) United States.
32. Bogdanov, A.L. *Advances in Resist Technology and Processing*. in *Advances in Resist Technology and Processing XVII*. 2000.
33. Microchem. *Permanent epoxy photoresist for pixel grids in electrowetting*; Available from: http://www.microchem.com/Appl-SpecDis-PermEpoxy.htm.
34. Hoyle, C.E. and C.N. Bowman, *Thiol–Ene Click Chemistry.* Angewandte Chemie International Edition, 2010. **49**(9): p. 1540-1573.
35. Cabral, J.T., et al., *Frontal Photopolymerization for Microfluidic Applications.* Langmuir, 2004. **20**(23): p. 10020-10029.
36. Bartolo, D., et al., *Microfluidic stickers.* Lab on a Chip, 2008. **8**(2): p. 274-279.
37. Cygan, Z.T., et al., *Microfluidic Platform for the Generation of Organic-Phase Microreactors.* Langmuir, 2005. **21**(8): p. 3629-3634.
38. Yuen, P.K. and V.N. Goral, *Low-cost rapid prototyping of flexible microfluidic devices using a desktop digital craft cutter.* Lab on a Chip, 2010. **10**(3): p. 384-387.
39. Carofiglio, T., et al., *Fullerene-Promoted Singlet-Oxygen Photochemical Oxygenations in Glass-Polymer Microstructured Reactors.* Advanced Synthesis & Catalysis, 2008. **350**(17): p. 2815-2822.
40. Donnola, P., *Sintesi organiche in reattori microfluidici*, in *Dipartimento di Scienze Chimiche*. 2010, Università degli Studi di Padova: Padova.
41. Wu, T., et al., *A New Synthetic Method for Controlled Polymerization Using a Microfluidic System.* Journal of the American Chemical Society, 2004. **126**(32): p. 9880-9881.
42. Xu, X., et al., *Integration of electrochemistry in micro-total analysis systems for biochemical assays: Recent developments.* Talanta, 2009. **80**(1): p. 8-18.
43. Marle, L. and G.M. Greenway, *Microfluidic devices for environmental monitoring.* TrAC Trends in Analytical Chemistry, 2005. **24**(9): p. 795-802.
44. Wang, H.-Y., et al., *Micro-sized microbial fuel cell: A mini-review.* Bioresource Technology, 2011. **102**(1): p. 235-243.

45. William B, Z., *Electrochemical microfluidics.* Chemical Engineering Science, 2011. **66**(7): p. 1412-1425.
46. Sullivan, S.P., et al., *Lattice Boltzmann simulations of electrolysis reactions: Microfluidic voltammetry.* Electrochemistry Communications, 2005. **7**(12): p. 1323-1328.
47. Li, P., et al., *Improvement of performance of dye-sensitized solar cells based on electrodeposited-platinum counter electrode.* Electrochimica Acta, 2008. **53**(12): p. 4161-4166.
48. Brinker, C.J. and G.W. Scherer, *The Physics and Chemistry of Sol-Gel Processing*. 1990, San Diego: Academic Press.
49. Hahn, J., J.H. Park, and M. Shin, *Modification method of microchannels of pdms microchip using sol-gel solution*. 2009.
50. Orhan, J.B., et al., *Internal Modification of Poly(dimethylsiloxane) Microchannels with a Borosilicate Glass Coating.* Langmuir, 2008. **24**(16): p. 9154-9161.
51. Kákoš, J., M. Mikula, and L. Harmatha, *Ultrathin insulating silica layers prepared from adsorbed TEOS, H2O and NH3 as a catalyst.* Microelectronics Journal, 2008. **39**(12): p. 1626-1628.
52. Brigo, L., et al., *An optical sensor for pH supported onto tentagel resin beads.* Sensors and Actuators B: Chemical, 2008. **130**(1): p. 477-482.
53. Natali, M., et al., *Rapid prototyping of multilayer thiolene microfluidic chips by photopolymerization and transfer lamination.* Lab on a Chip, 2008. **8**(3): p. 492-494.
54. Hung, L.-H., R. Lin, and A.P. Lee, *Rapid microfabrication of solvent-resistant biocompatible microfluidic devices.* Lab on a Chip, 2008. **8**(6): p. 983-987.
55. Teh, S.-Y., et al., *Droplet microfluidics.* Lab on a Chip, 2008. **8**(2): p. 198-220.
56. Concina, I., et al., *On-line monitoring and active control of dye uptake in dye-sensitised solar cells.* Chemical Communications, 2011. **47**(42): p. 11656-11658.
57. Gung, B.W. and R.T. Taylor, *Parallel Combinatorial Synthesis of Azo Dyes: A Combinatorial Experiment Suitable for Undergraduate Laboratories.* Journal of Chemical Education, 2004. **81**(11): p. 1630.
58. Bravo-Díaz, C., et al., *Dediazoniations in Water: An Integrated Physical Organic Chemistry Experiment.* Journal of Chemical Education, 2000. **77**(3): p. 384.
59. Molinaro, C., et al., *A Practical Synthesis of α-Aryl Methyl Ketones via a Transition-Metal-Free Meerwein Arylation.* The Journal of Organic Chemistry, 2007. **72**(5): p. 1856-1858.
60. Meerwein, H., E. Buchner, and K. van Emsterk, J. Prakt. Chem., 1939. **152**: p. 237.
61. Taylor, J.G., A.V. Moro, and C.R.D. Correia, *Evolution and Synthetic Applications of the Heck–Matsuda Reaction: The Return of Arenediazonium Salts to Prominence.* European Journal of Organic Chemistry, 2011. **2011**(8): p. 1403-1428.
62. O'Regan, B. and M. Gratzel, *A low-cost, high-efficiency solar cell based on dye-sensitized colloidal TiO2 films.* Nature, 1991. **353**(6346): p. 737-740.
63. Nazeeruddin, M.K., et al., *Combined Experimental and DFT-TDDFT Computational Study of Photoelectrochemical Cell Ruthenium Sensitizers.* Journal of the American Chemical Society, 2005. **127**(48): p. 16835-16847.
64. K. Nazeeruddin, M., P. Pechy, and M. Gratzel, *Efficient panchromatic sensitization of nanocrystalline TiO2 films by a black dye based on a trithiocyanato-ruthenium complex.* Chemical Communications, 1997(18): p. 1705-1706.
65. Sauvage, F.d.r., et al., *Effect of Sensitizer Adsorption Temperature on the Performance of Dye-Sensitized Solar Cells.* Journal of the American Chemical Society, 2011. **133**(24): p. 9304-9310.
66. Nazeeruddin, M.K., et al., *A swift dye uptake procedure for dye sensitized solar cells.* Chemical Communications, 2003(12): p. 1456-1457.

67. Holliman, P.J., et al., *Ultra-fast dye sensitisation and co-sensitisation for dye sensitized solar cells.* Chemical Communications, 2010. **46**(38): p. 7256-7258.
68. Peic, A., et al., *Real-Time Optical Waveguide Measurements of Dye Adsorption into Nanocrystalline TiO2 Films with Relevance to Dye-Sensitized Solar Cells.* The Journal of Physical Chemistry C, 2010. **115**(3): p. 613-619.
69. Fillinger, A. and B.A. Parkinson, *The Adsorption Behavior of a Ruthenium-Based Sensitizing Dye to Nanocrystalline TiO[sub 2] Coverage Effects on the External and Internal Sensitization Quantum Yields.* Journal of The Electrochemical Society, 1999. **146**(12): p. 4559-4564.
70. Lee, K., et al., *Selective positioning of organic dyes in a mesoporous inorganic oxide film.* Nat Mater, 2009. **8**(8): p. 665-671.
71. Cid, J.-J., et al., *Molecular Cosensitization for Efficient Panchromatic Dye-Sensitized Solar Cells.* Angewandte Chemie International Edition, 2007. **46**(44): p. 8358-8362.
72. Kuang, D., et al., *Co-sensitization of Organic Dyes for Efficient Ionic Liquid Electrolyte-Based Dye-Sensitized Solar Cells.* Langmuir, 2007. **23**(22): p. 10906-10909.
73. Ogura, R.Y., et al., *High-performance dye-sensitized solar cell with a multiple dye system.* Applied Physics Letters, 2009. **94**(7): p. 073308-3.
74. Wei, H., *Plasmonic Silver Nanoparticles for Energy and Optoelectronic Applications*, in *Advances in Nanomaterials and Nanostructures*. 2011, John Wiley & Sons, Inc. p. 171-184.
75. Mulvaney, P., *Surface Plasmon Spectroscopy of Nanosized Metal Particles.* Langmuir, 1996. **12**(3): p. 788-800.
76. Sherry, L.J., et al., *Localized Surface Plasmon Resonance Spectroscopy of Single Silver Triangular Nanoprisms.* Nano Letters, 2006. **6**(9): p. 2060-2065.
77. Jain, P., et al., *Review of Some Interesting Surface Plasmon Resonance-enhanced Properties of Noble Metal Nanoparticles and Their Applications to Biosystems.* Plasmonics, 2007. **2**(3): p. 107-118.
78. Volokitin, Y., et al., *Quantum-size effects in the thermodynamic properties of metallic nanoparticles.* Nature, 1996. **384**(6610): p. 621-623.
79. Cong, H., et al., *Silver Nanoparticle-Catalyzed Diels−Alder Cycloadditions of 2′-Hydroxychalcones.* Journal of the American Chemical Society, 2010. **132**(21): p. 7514-7518.
80. Jiang, Z.-J., C.-Y. Liu, and L.-W. Sun, *Catalytic Properties of Silver Nanoparticles Supported on Silica Spheres.* The Journal of Physical Chemistry B, 2005. **109**(5): p. 1730-1735.
81. Mailänder, V. and K. Landfester, *Interaction of Nanoparticles with Cells.* Biomacromolecules, 2009. **10**(9): p. 2379-2400.
82. Pan, Y., et al., *Size-Dependent Cytotoxicity of Gold Nanoparticles.* Small, 2007. **3**(11): p. 1941-1949.
83. Rycenga, M., et al., *Controlling the Synthesis and Assembly of Silver Nanostructures for Plasmonic Applications.* Chemical Reviews, 2011. **111**(6): p. 3669-3712.
84. Brust, M., et al., *Synthesis of thiol-derivatised gold nanoparticles in a two-phase Liquid-Liquid system.* Journal of the Chemical Society, Chemical Communications, 1994(7): p. 801-802.
85. Turkevich, J., P.C. Stevenson, and J. Hillier, *A study of the nucleation and growth processes in the synthesis of colloidal gold.* Discussions of the Faraday Society, 1951. **11**: p. 55-75.
86. Kimling, J., et al., *Turkevich Method for Gold Nanoparticle Synthesis Revisited.* The Journal of Physical Chemistry B, 2006. **110**(32): p. 15700-15707.
87. Stamplecoskie, K.G. and J.C. Scaiano, *Light Emitting Diode Irradiation Can Control the Morphology and Optical Properties of Silver Nanoparticles.* Journal of the American Chemical Society, 2010. **132**(6): p. 1825-1827.

88. Jin, R., et al., *Photoinduced Conversion of Silver Nanospheres to Nanoprisms.* Science, 2001. **294**(5548): p. 1901-1903.
89. Zheng, X., et al., *Photochemical Formation of Silver Nanodecahedra: Structural Selection by the Excitation Wavelength.* Langmuir, 2009. **25**(6): p. 3802-3807.
90. Maillard, M., P. Huang, and L. Brus, *Silver Nanodisk Growth by Surface Plasmon Enhanced Photoreduction of Adsorbed [Ag+].* Nano Letters, 2003. **3**(11): p. 1611-1615.
91. Sant'Ana, A.C., et al., *Size-dependent SERS enhancement of colloidal silver nanoplates: the case of 2-amino-5-nitropyridine.* Journal of Raman Spectroscopy, 2009. **40**(2): p. 183-190.
92. Macdonald, D.D., *Reflections on the history of electrochemical impedance spectroscopy.* Electrochimica Acta, 2006. **51**(8-9): p. 1376-1388.
93. Grahame, D.C., *The Electrical Double Layer and the Theory of Electrocapillarity.* Chemical Reviews, 1947. **41**(3): p. 441-501.
94. Macdonald, D.D., *Transient Techniques in Electrochemistry*. 1977, New York: Plenum Press.
95. Johnson, B.J. and S.-M. Park, *Electrochemistry of Conductive Polymers.* Journal of The Electrochemical Society, 1996. **143**(4): p. 1277-1282.
96. Han, L., et al., *Modeling of an equivalent circuit for dye-sensitized solar cells.* Applied Physics Letters, 2004. **84**: p. 2433-2435.
97. Wang, Q., J.-E. Moser, and M. Grätzel, *Electrochemical Impedance Spectroscopic Analysis of Dye-Sensitized Solar Cells.* The Journal of Physical Chemistry B, 2005. **109**(31): p. 14945-14953.
98. Chang, B.-Y. and S.-M. Park, *Electrochemical Impedance Spectroscopy.* Annual Review of Analytical Chemistry, 2010. **3**(1): p. 207-229.
99. Darowicki, K. and P. Ślepski, *Dynamic electrochemical impedance spectroscopy of the first order electrode reaction.* Journal of Electroanalytical Chemistry, 2003. **547**(1): p. 1-8.
100. Smith, K.C., et al., *The Spatially Distributed Dynamic Transmembrane Voltage of Cells and Organelles due to 10 ns Pulses: Meshed Transport Networks.* IEEE Transactions on Plasma Science, 2006. **34**(4): p. 1394-1404.
101. Randles, J.E.B., *Kinetics of rapid electrode reactions.* Discussions of the Faraday Society, 1947. **1**: p. 11-19.
102. Kroto, H.W., et al., *C60: Buckminsterfullerene.* Nature, 1985. **318**(6042): p. 162-163.
103. Hirsch, A. and M. Brettreich, *Fullerenes: Chemistry and Reactions*. 2005, Weinheim: Wiley-VCH Verlag GmbH & Co. KGaA.
104. Prato, M., *[60]Fullerene chemistry for materials science applications.* Journal of Materials Chemistry, 1997. **7**(7): p. 1097-1109.
105. Bonifazi, D., O. Enger, and F. Diederich, *Supramolecular [60]fullerene chemistry on surfaces.* Chemical Society Reviews, 2007. **36**(2): p. 390-414.
106. Ashcroft, J.M., et al., *Fullerene (C60) immunoconjugates: interaction of water-soluble C60 derivatives with the murine anti-gp240 melanoma antibody.* Chemical Communications, 2006(28): p. 3004-3006.
107. Salice, P., et al., *The continuous-flow cycloaddition of azomethine ylides to carbon nanotubes.* Chemical Communications, 2011. **47**(32): p. 9092-9094.
108. Nazario, M. and F. Giacalone, *Fullerene polymers*, ed. W.V. GmbH. 2009, Weinheim.
109. Seyler, H., et al., *Continuous Flow Synthesis of Fullerene Derivatives.* The Journal of Organic Chemistry, 2011. **76**(9): p. 3551-3556.
110. Bingel, C., *Cyclopropanierung Von Fullerenen.* Chemische Berichte, 1993. **126**: p. 1957.
111. Camps, X. and A. Hirsch, *Efficient cyclopropanation of C_{60} starting from malonates.* Journal of the Chemical Society, Perkin Transactions 1, 1997(11): p. 1595-1596.

112. Beuerle, F. and A. Hirsch, *Synthesis of Amphiphilic [60]Fullerene [3:3]Hexakisadducts with Four Spherically Defined Addend Zones.* Chemistry – A European Journal, 2009. **15**(30): p. 7447-7455.
113. Spänig, F., et al., *trans-2 Addition Pattern to Power Charge Transfer in Dendronized Metalloporphyrin C60 Conjugates.* Journal of the American Chemical Society, 2009. **131**(26): p. 9378-9388.
114. Hirsch, A., I. Lamparth, and H.R. Karfunkel, *Fullerene Chemistry in Three Dimensions: Isolation of Seven Regioisomeric Bisadducts and Chiral Trisadducts of C60 and Di(ethoxycarbonyl)methylene.* Angewandte Chemie International Edition in English, 1994. **33**(4): p. 437-438.
115. Hirsch, A., et al., *Regiochemistry of Multiple Additions to the Fullerene Core: Synthesis of a Th-Symmetric Hexakis adduct of C60 with Bis(ethoxycarbonyl)methylene.* Journal of the American Chemical Society, 1994. **116**(20): p. 9385-9386.
116. Kuwahara, S., et al., *Conclusive Determination of the Absolute Configuration of Chiral C60-Fullerene cis-3 Bisadducts by X-ray Crystallography and Circular Dichroism.* Angewandte Chemie International Edition, 2005. **44**(15): p. 2262-2265.
117. Silvestrini, S., et al., *Synthesis of methanofullerenes in microreactors: kinetic analysis and potential applications*. 2010, Oral Communication at uFlu 2010 - Second European Metting on Microfluidics: Tolouse.
118. Maggini, M., G. Scorrano, and M. Prato, *Addition of azomethine ylides to C60: synthesis, characterization, and functionalization of fullerene pyrrolidines.* Journal of the American Chemical Society, 1993. **115**(21): p. 9798-9799.
119. Prato, M. and M. Maggini, *Fulleropyrrolidines: A Family of Full-Fledged Fullerene Derivatives.* Accounts of Chemical Research, 1998. **31**(9): p. 519-526.
120. Campidelli, S.p., et al., *Diastereoisomerically Pure Fulleropyrrolidines as Chiral Platforms for the Design of Optically Active Liquid Crystals.* Journal of the American Chemical Society, 2010. **132**(10): p. 3574-3581.
121. Possamai, G., et al., *A fullerene-azothiophene dyad for photovoltaics.* Synthetic Metals, 2003. **139**(3): p. 585-588.

Ringraziamenti

Ci sono persone senza cui questa tesi di dottorato non sarebbe mai stata scritta. Mi riferisco al mio supervisore, prof. Maggini, ma anche agli altri strutturati del gruppo di ricerca e in particolare al prof. Carofiglio. Li ringrazio soprattutto per l'esempio scientifico, per le possibilità che mi hanno dato e per tutte le discussioni stimolanti dal punto di vista scientifico e non.

Un grazie a tutte le persone citate negli "acknowledgements" dei vari capitoli, senza cui questa tesi sarebbe stata molto più povera. A queste persone dovrei sicuramente aggiungere il dott. Rossetto e la prof. Ferrante, sempre estremamente disponibili.

Grazie a coloro che in ogni tempo furono nello studio 013: Iria, Marta, Enrica, Alessandro figo & Alessandro barbone (intercambiabili a seconda dei giorni), Gaetano e Prashant. La scienza è nulla se non è divertente. Un ringraziamento particolare a Renato, senza cui questo dottorato sarebbe stato forse un po' più produttivo ma sicuramente *molto* meno divertente. Alla fine vincono le armate rosse.

Grazie alla mia famiglia: Nini, Anna, Silvia e Stefano. Infine, c'è molto di Federica in questo lavoro, come mostrato in figura 7.1, nonostante di microfluidica ne capisca fin lì…

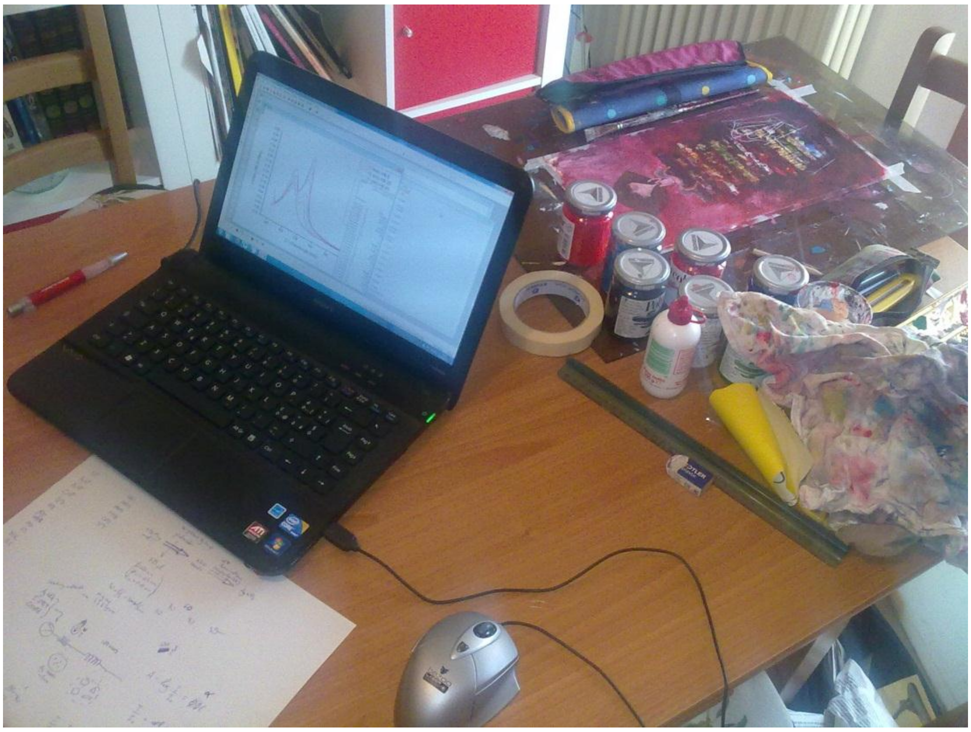

Figure 7.1. Ultimo giorno di stesura della tesi.